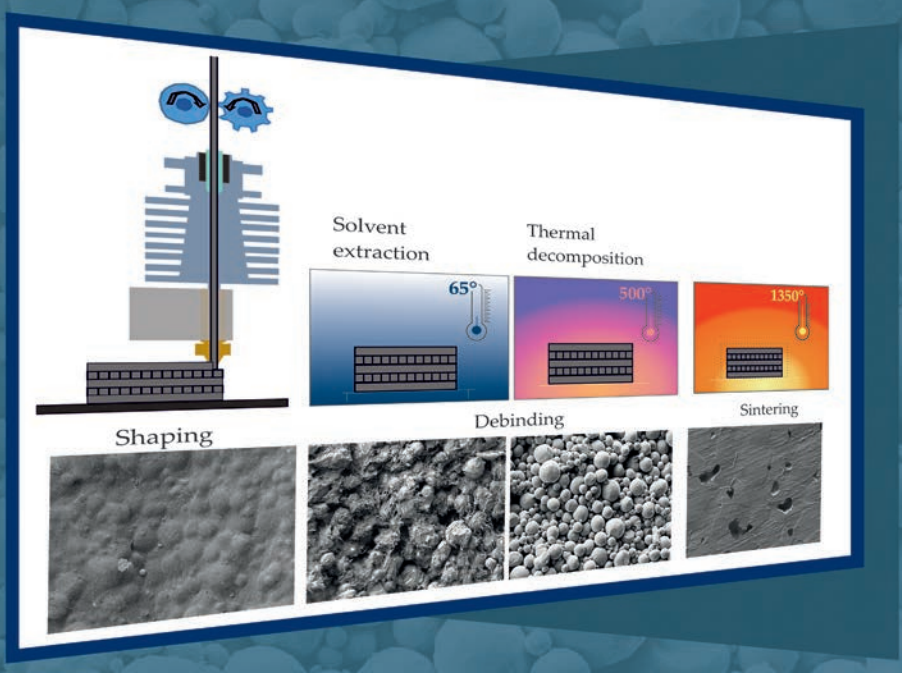

FAU Studien Materialwissenschaft und Werkstofftechnik 26

Yvonne Thompson

Additive Manufacturing by Metal Fused Filament Fabrication

FAU University Press

Yvonne Thompson

Additive Manufacturing by Metal Fused Filament Fabrication

FAU Studien

Materialwissenschaft und Werkstofftechnik

Band 26

Herausgeber der Reihe:

Prof. Dr. rer. nat. Mathias Göken

Yvonne Thompson

Additive Manufacturing by Metal Fused Filament Fabrication

Erlangen
FAU University Press
2023

Bibliografische Information der Deutschen Nationalbibliothek:
Die Deutsche Nationalbibliothek verzeichnet diese Publikation in der Deutschen Nationalbibliografie; detaillierte bibliografische Daten sind im Internet über http://dnb.d-nb.de abrufbar.

Bitte zitieren als
Thompson, Yvonne. 2023. *Additive Manufacturing by Metal Fused Filament Fabrication.* FAU Studien Materialwissenschaft und Werkstofftechnik Band 26. Erlangen: FAU University Press. DOI: 10.25593/978-3-96147-688-6.

Verlag und Auslieferung:
FAU University Press, Universitätsstraße 4, 91054 Erlangen

Druck: docupoint GmbH

ISBN: 978-3-96147-687-9 (Druckausgabe)
eISBN: 978-3-96147-688-6 (Online-Ausgabe)
ISSN: 2197-2575
DOI: 10.25593/978-3-96147-688-6

Additive Manufacturing by Metal Fused Filament Fabrication

Additive Fertigung von Metallen mittels Filamentextrusion

Der Technischen Fakultät
der Friedrich-Alexander-Universität
Erlangen-Nürnberg

zur
Erlangung des Doktorgrades Dr.-Ing.

vorgelegt von

Yvonne Thompson

aus Col. Lomas Verdes Naucalpan (Mexiko)

Als Dissertation genehmigt
von der Technischen Fakultät
der Friedrich-Alexander-Universität Erlangen-Nürnberg

Tag der mündlichen Prüfung:	19.06.2023
Gutachter:	Prof. Dr. Peter J. Felfer
	Prof. Dr. rer. nat. Eric Jägle

Summary

Additive manufacturing (AM) is the fabrication of 3-dimensional parts without the use of design-specific tooling. Among the variety of AM technologies, fused filament fabrication (FFF) has become one of the most widely used methods for polymeric materials. Recent development of innovative feedstock formulations has led to the availability of filaments with metallic or inorganic powder contents exceeding 55 vol%. Metal fused filament fabrication (MF^3) with metal-filled filaments is an indirect process that uses polymeric binders for additive shaping of green bodies. These are processed into solid metal parts after debinding and sintering. Due to the filament-based shaping, this process can be used for the additive manufacturing of all sinterable powder materials requiring low investment costs. The MF^3 process could thus provide a cost-effective and material-flexible alternative to powder bed fusion (PBF) manufacturing of small metallic components with complex shapes. To enable a successful process application, parameter optimization as well as the selection of the furnace atmosphere for each individual process step is crucial to achieve a high final density. In this context, the applied parameters have a significant influence on the microstructure and the functional and mechanical properties of the manufactured components.

It is the aim of this work to identify suitable parameter sets for the individual process steps and to evaluate the applicability of MF^3 for AM of various high-value metal alloys. This includes a general parameter optimization for each step of the entire process chain of shaping, debinding and sintering, independently of the processed metal powder. Based on the general process implementation, systematic parameter studies were performed for 316L,Ampersint 1557.02,cp-Ti, IN 718, CoWAlloy3mod, and 99 % pure Cu to derive the best processing strategies for each of these metals. In each case, a characterization of the microstructure and mechanical properties of the fabricated materials is presented. The accomplished process optimization provides suitable parameters for each material, enabling the use of MF^3 for AM of parts with mechanical properties similar to properties of conventionally fabricated parts.

The versatility of the implemented process is highlighted in the last part of this work by demonstrating the capabilities of multi-material MF^3. The use of the same polymeric binder system in all filaments allows the

combination of several materials in one green body. By finding suitable co-sintering parameters, metallic laminates and metal-ceramic composites were successfully produced and proof of the feasibility of multi-material AM is provided. In addition, the production of complex geometries using sacrificial ceramic support structures is demonstrated as an extension of multi-material MF³.

Zusammenfassung

Additive Fertigung (engl. *additive manufacturing (AM)*) ist die Herstellung dreidimensionaler Bauteile ohne den Einsatz formspezifischer Werkzeuge. Unter der Vielzahl der AM-Technologien ist die Filamentextrusion (engl. *fused filament fabrication (FFF)*) zu einer der am häufigsten verwendeten Methoden für polymere Werkstoffe geworden. Die jüngste Entwicklung innovativer Feedstockformulierungen hat zur Verfügbarkeit von Filamenten mit einem Gehalt an metallischen oder anorganischen Pulvern von mehr als 55 vol% geführt. Das Metallextrusionsverfahren (engl. *metal fused filament fabrication (MF³)*) unter Verwendung metallgefüllter Filamente ist ein indirektes Verfahren, das polymere Bindemittel für die additive Formgebung von Grünkörpern verwendet, aus denen nach dem Entbindern und Sintern kompakte Metallteile hergestellt werden. Aufgrund der filamentbasierten Formgebung kann dieses Verfahren für die additive Fertigung aller sinterfähigen Pulverwerkstoffe bei geringen Investitionskosten eingesetzt werden. Das MF³-Verfahren stellt somit eine kostengünstige und werkstoffflexible Alternative zu Pulverbettverfahren für kleine metallische Bauteile komplexer Geometrie dar. Für eine erfolgreiche Prozessanwendung sind eine Parameteroptimierung sowie die Wahl der Ofenatmosphäre für jeden einzelnen Prozessschritt entscheidend, um eine hohe Enddichte zu erreichen. In diesem Zusammenhang haben die angewandten Parameter einen wesentlichen Einfluss auf die Mikrostruktur und die funktionellen und mechanischen Eigenschaften der hergestellten Bauteile.

Ziel dieser Arbeit ist es, geeignete Parametersätze für die einzelnen Prozessschritte zu identifizieren und die Anwendbarkeit von MF³ für verschiedene hochwertige Metalllegierungen zu bewerten. Dies beinhaltet eine generelle Parameteroptimierung jedes Schrittes der gesamten Prozesskette von Formgebung, Entbindern und Sintern, unabhängig vom verarbeiteten Metallpulver. Auf der Grundlage der allgemeinen Prozessimplementierung werden systematische Parameterstudien für 316L, Ampersint 1557.02, cp-Ti, IN 718, CoWAlloy3mod und 99 % reines Cu durchgeführt, um die besten Verarbeitungsstrategien für jedes dieser Metalle abzuleiten. In jedem Fall wird eine Charakterisierung der Mikrostruktur und der mechanischen Eigenschaften der hergestellten Werkstoffe

vorgestellt. Die durchgeführte Prozessoptimierung liefert für jedes Material geeignete Parameter, die den Einsatz von MF³ für die additive Fertigung von Teilen mit ähnlichen mechanischen Eigenschaften wie bei konventionellen Verfahren ermöglichen.

Die Vielseitigkeit des implementierten Prozesses wird im letzten Teil dieser Arbeit durch die Option des Multimaterial-MF³ hervorgehoben. Die Verwendung desselben polymeren Bindemittelsystems in allen Filamenten ermöglicht die Kombination mehrerer Materialien in einem Grünkörper. Durch die Auswahl geeigneter Co-Sinter-Parameter konnten metallische Laminate und Metall-Keramik-Verbundwerkstoffe erfolgreich gefertig werden. Darüber hinaus wird die Herstellung komplexer Geometrien unter Verwendung von keramischen Stützstrukturen als Erweiterung des Multimaterial-MF³ demonstriert.

Contents

List of Abbreviations

Abbreviation	Description
316L	X2CrNiMo17-12-2 austenitic stainless steel
AM	Additive manufacturing
Ampersint 1557.02	X40CrMoV5-1 hot work tool steel
AMS	Aerospace material standard
APT	Atom probe tomography
BSE	Backscattered electrons
CAD	Computer aided design
CoWAlloy3	Co-base superalloy 3 with increased Mo content
CoWAlloy3mod	Modified Co-base superalloy 3
cp-Ti	Commercially-pure titanium (Gd. 1 as per ASTM F67 [1])
DED	Direct energy deposition
EBSD	Electron backscattered diffraction
EDX	Energy dispersive X-ray spectroscopy
EPBF	Electron powder bed fusion
FAU	Friedrich-Alexander-Universität Erlangen-Nürnberg
FDMet	Fused deposition of metals
FFF	Fused filament fabrication
FIB	Focused ion beam
GB	Grain boundary
HIP	Hot isostatic pressing
IACS	International annealed copper standard
IN 718	Inconel™alloy 718
IPF	Inverse pole figure
IR	Infrared

Abbreviation	Description
LDPE	Low density polyethylene
LPBF	Laser powder bed fusion
MA	Maleic acid anhydride
MBJT	Metal binder jetting
MF³	Metal fused filament fabrication
MIM	Metal powder injection molding
MUL	Montanuniversität Leoben
NDIR	Non-dispersive infrared technology
NMF	Neue Materialien Fürth
NNS	Near net shape
PBF	Powder bed fusion
PEG	Polyethylene glycol
pO_2	Oxygen partial pressure
PP	Polypropylene
PPB	Prior particle boundary
Q & T	Quenched and tempered
RT	Room temperature
RUB	Ruhr-Universität Bochum
SA	Stearic acid
SEM	Scanning electron microscope
ρ_T	Theoretical density
TEM	Transmission electron tomography
Tg	Glass transition temperature
TGA	Thermogravimetric analysis
TPE	Thermoplastic elastomer

Own publications

Parts of this thesis have already been published:

[1] **Thompson, Yvonne**; Gonzalez-Gutierrez, J.; Kukla, C.; Felfer, P.: Fused Filament Fabrication, Debinding and Sintering as a Low Cost Additive Manufacturing Method of 316L Stainless Steel. In: *Additive Manufacturing* 30 (2019), 100861.

[2] **Thompson, Yvonne**; Polzer, M.; Gonzalez-Gutierrez, J.; Kasian, O.; Heckl, J. P.; Dalbauer, V.; Kukla, C.; Felfer, P. J.: Fused Filament Fabrication-based Additive Manufacturing of Commercially Pure Titanium. In: *Advanced Engineering Materials* 23.12 (2021), 2100380.

[3] **Thompson, Yvonne**; Zissel, K.; Förner, A.; Gonzalez-Gutierrez, J.; Kukla, C.; Neumeier, S.; Felfer, P.: Metal Fused Filament Fabrication of the Nickel-Base Superalloy IN 718. In: *Journal of Materials Science* 57.21 (2022), 9541–9555.

[4] Gonzalez-Gutierrez, J.; **Thompson, Yvonne**; Cano, S.; Felfer, P.; Kukla, C.; Holzer, C.: *Steel Parts Produced by Material Extrusion Additive Manufacturing, Solvent Debiding and Sintering*. In: *Materials Science and Technology 2019 Conference Proceedings*. Portland, Oregon USA, 2019, 264–266.

[5] Gonzalez-Gutierrez, J.; **Thompson, Yvonne**; Handl, D.; Cano, S.; Schuschnigg, S.; Felfer, P.; Kukla, C.; Holzer, C.; Burkhardt, C.: Powder Content in Powder Extrusion Moulding of Tool Steel: Dimensional Stability, Shrinkage and Hardness. In: *Materials Letters* 283 (2021), 128909.

1 Introduction and motivation

Additive manufacturing (AM) techniques that no longer require design-specific tooling reshape the manufacturing landscape since the first AM patent comprising stereolithography was filed in 1984 [2]. Driven by digitalization, the implications of the modern manufacturing paradigm are mass customization and on-demand production. Emerging additive technologies introduced a shift in the production of metallic engineering components from manual manufacturing towards a completely digitalized value chain.

Among the many available manufacturing processes, AM methods are one processing group that realizes fabrication directly from digital computer aided design (CAD) models. Since the appearance of the concept of layer-by-layer manufacturing, a variety of different processes have been developed for AM of all material classes. These novel methods, which offer a high degree of design flexibility, allow to quickly adapt products to current demand. However, the available processes still have deficits in terms of production rate and unit costs, implying no ideal solution for metal production exists yet. For metal AM, the cost issue represents the bottleneck in overcoming the step from the rapid prototyping stage to an established production process [3, 4].

The metal fused filament fabrication (MF^3) offers a solution for affordable and customized production at small batch size. The potential of this process was recognized as early as 1996 [5–7], and intensive research efforts have contributed to the development of a range of highly filled filaments suitable for fused filament fabrication (FFF) [8–10]. However, at the time this project was started in 2018, literature on debinding and sintering of FFF printed green bodies was scarce and only few results on sintered samples had been reported [11–13]. Although research has been intensified in recent years, detailed studies on the sintering step are still lacking and fabricated metal parts possess process-related porosity that adversely effects mechanical and functional properties [14–19].

It is therefore the objective of this work to close the gap in the investigation of the MF^3 process chain, which includes FFF, debinding and sintering, and to unlock the full potential of this novel process. In this context, a particular goal is the acquisition of a detailed understanding of the process-specific influences on the debinding and sintering steps.

The decisive factors for good component quality are limitation of impurity uptake in the course of MF³ processing and the achievement of high sintered density. The acquired knowledge will contribute to the applicability of MF³ for affordable AM of small to medium-sized metallic components for functional application purposes.

2 Metal manufacturing processes

The range of processes for fabrication of metallic components is broad and subject to constant innovation. Through a variety of efforts, manufacturing efficiency has steadily improved and offers little potential for further productivity or quality enhancements. Thus, today's production technologies are characterized by fabricating products in high quantities in a resource-saving, cost-efficient and high-quality manner, but with low variance. As an additional requirement, the request for efficient use of raw materials has driven the development of near net shape (NNS) fabrication techniques to reduce the need of substractive machining in the scope of processing. By now, a large number of processes are available for the NNS manufacturing of metals and existing processes are constantly developed or supplemented by new systems [20–23]. This state is underlined by the chart of, according to publication numbers, most investigated NNS methods in Fig. 1 which shows medium to large production volumes for the majority of the processes.

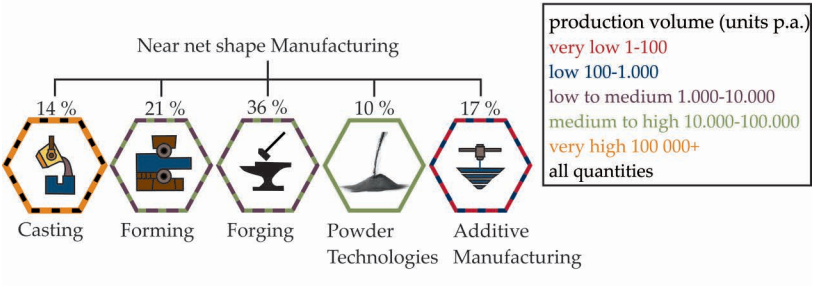

Figure 1: Chart of, according to publication numbers evaluated by Marini, Cunningham, and Corney most investigated NNS methods. The remaining 2 % correspond to machining processes [23]. The colors of the hexagons represent the feasible production volumes [24].

The trend towards customization dictated by the increasingly digitalized modern society requires further developments towards more flexible production with competitive supply chains. New processing approaches that enable manufacturing directly from digital models without the need for design-specific tools are provided by AM [25]. Intensive investigations during the last two decades lead to the development of a variety of technologies to offer AM options for all material classes [26, 27]. Among

these, the established processes for AM of metals are generally very cost-intensive. The MF³, which is considered a cost-effective alternative, takes advantage of the easy shapeability of polymeric materials before they are removed in subsequent process steps to produce a purely metallic or ceramic part.

In order to assess the potential of this process, the following section will first provide an overview of the currently established processes for the free-form fabrication of metals. The selected processes are presented in a material-independent way and specifics concerning the processing of certain metals are not discussed in detail. A complete overview of existing processes and additional information can be obtained from literature [27–32].

The MF³ process designed as part of this work is presented in section 2.2. Since the nature of this process is similar to the established metal powder injection molding (MIM), the processing steps and key influencing factors of both methods are summarized in the same section. The underlying scientific principles necessary to obtain a deeper understanding are discussed with a focus on the material level in chapter 3.

2.1 Additive manufacturing

Additive processing implies that materials are subsequently added layer-by-layer with the aim to build-up a new product. Within the additive processes, a distinction is made between form-free processes and those which require design-specific tooling for shaping the final contour [25]. Only freeform fabrication, i.e. processes of the first category, are referred to as AM methods [33]. These production technologies are characterized by a high degree of design flexibility and permit changes to the component design at short notice.

Since the different classes of materials place very different demands on the manufacturing process, a large number of AM processes were developed. The ASTM standard F2792-12a defined the term AM in 2012 and made an attempt to classify the most important processes [34]. It was replaced in 2015 by the joint ISO/ASTM 52900:2015 standard [33]. By today, this revised standard can no longer satisfactorily classify all existing methods, just a few years after its introduction. Kumar therefore pursues an approach for the classification of existing AM processes, which also takes into account developments that are expected in the future [25].

The classification is based on the type of material feed and differentiates between the categories of (1) *powder bed-based processes*, (2) *processes with material deposition* and (3) *processes where no material feeding in the sense of a periodically repeated material movement* takes place in the course of manufacturing. The three categories are subdivided into layer-based and non-layer-based processes. Since all material bed processes imply layer formation and all motionless material processes are of the non-layer type, a classification of additive manufacturing can be made, as demonstrated in Fig. 2. As this classification is highly asymmetric and the majority of processes is of the layer-based type, AM has become a synonym for layer-wise manufacturing. This is particularly the case since ASTM defines AM as layer upon layer methodologies [33]. In this work, the abbreviation AM is used in accordance with common practice in the sense of additive layer manufacturing.

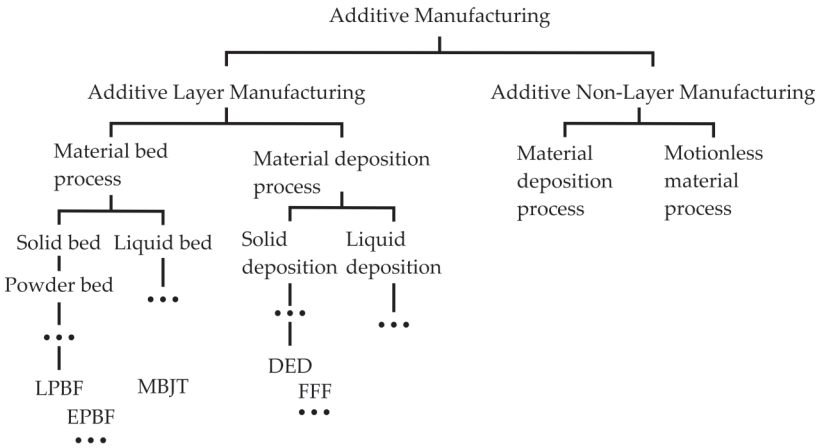

Figure 2: Classification of additive manufacturing according to Kumar [25].

In all additive processes, the shaping step is based on a CAD model. Little post-processing is required to improve the surface quality or enhance mechanical properties of printed parts. The specific operations such as polishing or heat treatments vary depending on the process, material and application [35]. The selection of a suitable process depends strongly on the material, as its thermal properties such as melting point, thermal conductivity and coefficient of thermal expansion as well as the optical properties limit the applicability [30]. Even within one material class, not

every material can be processed with the same available technology. The resulting microstructure and material properties vary as a function of the AM process used and the respective process parameters [32]. Process optimization can be very time-consuming and costly. In order to make an economical process selection, the intended application must always be taken into account to ensure that the required mechanical and functional requirements are met.

The additive manufacturing of small and medium-sized metal parts is mostly realized by means of beam-based powder bed fusion (PBF) processes. Depending on the energy source used, a distinction is made between laser powder bed fusion (LPBF) and electron powder bed fusion (EPBF). In both cases, the first step is the application of a layer of metal powder to the build platform before the material is selectively fused or melted. Surrounding powder serves to provide additional support for the manufactured structures until the process is completed. Afterwards, the component can be removed directly and the fabricated part is basically ready for its application. The only post-processing steps required are the removal of excess, loosely adhering powder and, if necessary, of printed support structures. If keyhole-porosity is prevented by optimized printing parameters, beam-based additive manufacturing delivers components of high density, with remaining porosity mostly attributed to entrapped process gas at levels of 0.1 % to 1.0 % [27, 29]. Optional post-processing steps such as hot isostatic pressing (HIP), heat treatment, machining and polishing can improve the mechanical properties of PBF processed parts. A characteristic of these processes is the anisotropic microstructure of components due to the layered manufacturing [36]. As a result, fabricated parts exhibit anisotropic properties associated with the build direction, which are detrimental to their application [37]. Current research investigates the influence of different scanning strategies on this process-related anisotropy [36, 38]. Depending on the susceptibility to oxidation of the processed metal, the choice of a suitable atmosphere in PBF can also have a major impact on the achievable component quality. LPBF processes have already been intensively researched, especially for the additive manufacturing of steel, titanium alloys and superalloys [39–47]. The electron beam as an energy source in EPBF additionally enables the processing of highly reflective materials and therefore expands the material portfolio, for example, for the processing of pure copper [48, 49] or high melting materials [50].

Due to the small layer height, the production of larger components using the powder bed processes is very time-consuming and generates high costs [32, 51]. As an alternative, direct energy deposition (DED) can be used for manufacturing of larger component volumes. In this process focused thermal energy is used to fuse materials by melting as they are deposited onto a substrate. The heat source can be either a laser, arc or electron beam with feed-material in form of metal wire or powder. At first a NNS part is produced layer by layer while the final shape is achieved by subsequent machining. The combination of rapid build-up of the rough contour and subsequent fine machining, allows an accelerated production of structural components with low material loss and high final densities [52–55]. However, the repeated heating while depositing further layers produces strong microstructural variations and inevitably residual stress. Subsequent heat treatment is neccessary for homogenization of the microstructure and increasing mechanical strength and ductility [56].

These established AM processes all provide NNS fabrication of metals to high density parts with effective utilization of material. However, the long production times due to layer-by-layer manufacturing and the expensive equipment result in high manufacturing costs per component. The use of AM of metals is therefore currently only justifiable for small quantities or particularly valuable materials.

2.2 The metal fused filament fabrication process

Free-form manufacturing of metals, that allows flexible modification of the component design, is currently only realized by means of the cost-intensive PBF or DED processes. These deliver good mechanical properties that are not necessary for every application. For applications where functional properties are the primary concern, a more cost-effective additive process can represent an alternative production method if reduced density and strength are acceptable. The MF³ thus closes the gap shown in Fig. 3 for an economical mold-free production of small metal parts [57].

The MF³ was developed by analogy to MIM from a method originally implemented for polymer processing. Both processes start with the mixing of sinterable metal powder with a polymeric binder and compounding of a homogeneous feedstock. To make it available for FFF, the feedstock is extruded into a filament that can be fed into any commercial desktop 3D

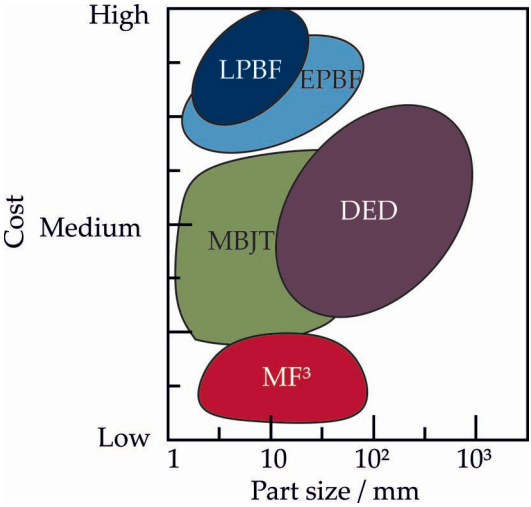

Figure 3: Comparison of major AM methods in terms of part size and cost. LPBF: Laser powder bed fusion, EPBF: Electron powder bed fusion, DED: Direct energy deposition, MBJT: Metal binder jetting, MF³: Metal fused filament fabrication. Reprinted and adapted with permission [57]. Values from [54, 58, 59].

printer. In case of MIM, the granulated feedstock is molded under pressure using design-specific tools. In both shaping techniques, the organic components within the feedstock allow cost-effective shaping of green bodies. Further process steps follow as shown in Fig. 4 for removal of the binder and densification of the remaining powder body by sintering.

The time-critical step is the removal of the organic binder components. At this point, a two-stage process with preceding solvent debinding can contribute to a reduction in the total duration [60, 61]. By chemical extraction of one of the binder components, interconnecting pore channels are created inside the part which, act as transportation routes for outgassing of decomposition products during the subsequent thermal debinding process [62]. During this step, the equilibrium between the decomposition of the polymer chains and the removal of the resulting carbon compounds must be precisely controlled, since a pressure increase inside the sample results in the formation of irreversible defects [63, 64]. After complete debinding, the highly porous part is densified during sintering. In order to reduce the remaining porosity, temperatures just below the solidus temperature of the processed alloy are usually used. Additional

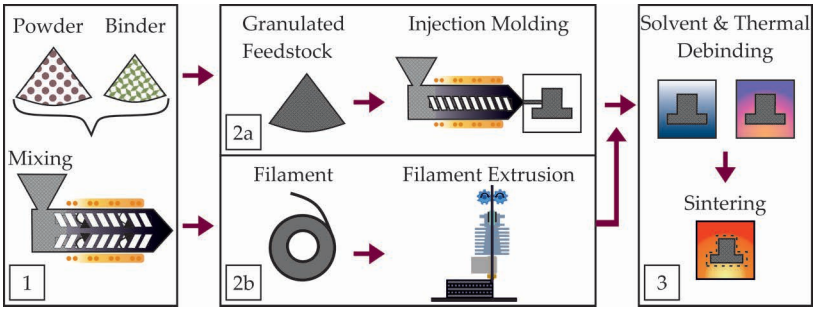

Figure 4: Comparison of MF³ and MIM process chains. Step 1: Mixing of powder and binder and kneading for homogenization. Step 2: Either injection molding of the granular feedstock (MIM) or FFF in case of MF³. Step 3: Debinding and sintering for both processing routes.

densification can be achieved with HIP by applying external pressure during the sintering process. A uniform powder packing inside the green body is demanded to avoid distortion during densification [65–67]. In any case, the reduction of component dimensions during sintering must be taken into account in advance during designing and dimensioning. The produced components reach densities of 95 % to 99 % with linear shrinkage of 15 % to 25 % in each dimension [68, 69]. The shrinkage of MF³ parts is generally higher than for MIM parts because the injection molded feedstock can tolerate a higher viscosity and thus a higher solids loading due to the high pressure applied during injection molding [70].

The MIM process has been widely used since the 1970s for the mass production of small components made of steels, superalloys and titanium [71–78]. Intensive research contributed to an optimization of processing parameters, so that manufactured parts exhibit high mechanical strength and good deformation behavior. Components produced by metal powder injection molding are used in a variety of applications. However, cost-effectiveness is only achieved at high quantities due to the cost associated with the needed design-specific tooling [79]. If the required production volume is given, MIM is the process of choice for the cost-effective production of small metal parts.

For the production of small quantities, the MF³ is a technology complementary to MIM. The availability of new materials is facilitated by findings from previous MIM research, which involved the optimization

of process parameters for specific materials [80]. Relevant processing differences result from the necessary extrudability to enable FFF. Initial investigations to integrate significant amounts of metallic particles into printable filaments began as early as 1970 under the name fused deposition of metals (FDMet) [5, 6]. Increasing the powder content in filaments for conventional FFF printers has been the subject of intense research efforts ever since [81]. Feedstocks for the production of green bodies must contain a high proportion of metallic powder in order to be suitable for subsequent debinding and sintering. However, increasing the powder content directly results in an exponential increase in viscosity [82–85]. In order to maintain extrudability, the viscosity increase must be compensated by selecting appropriate organic components. Details of possible binder compositions as well as rheological properties of MF³ filaments are considered in [86–88].

After successful filament development, printed green bodies can be further processed using the equipment established for MIM production. The microstructure evolution during the individual process steps of FFF, debinding and sintering is displayed in Fig. 5 for the case of commercially-pure ti-tanium (Gd. 1 as per ASTM F67 [1]) (cp-Ti). The morphology of parts in the course of processing is visualized in the lower line, assigned to the respective individual steps. The organic binder, that ensures viscous flow during filament extrusion, is removed step by step until a purely metallic component is produced. Densification of the remaining metal particles is created by sintering at elevated temperature during the final step.

The reduced proportion of metal powder in the green body (on average 55 vol% compared to up to 70 vol% in MIM) requires modifications to the debinding step. Sintering parameters must be adjusted to the specific metal, whereby values from MIM can be used. Achievable relative densities after pressureless sintering are in the range of 95 % to 98 % and thus below the values achieved in MIM [70]. The components produced in the MF³ are therefore not suitable for use in mechanically highly stressed components if no extra HIP is applied. From an economic point of view, MF³ production is nevertheless preferable to MIM for small quantities. Investment costs can be kept low by using existing MIM equipment and no additional design-specific tools are required.

The MF³ process represents a cost-effective alternative for the form-free production of metals if the residual porosity can be reduced to a minimum

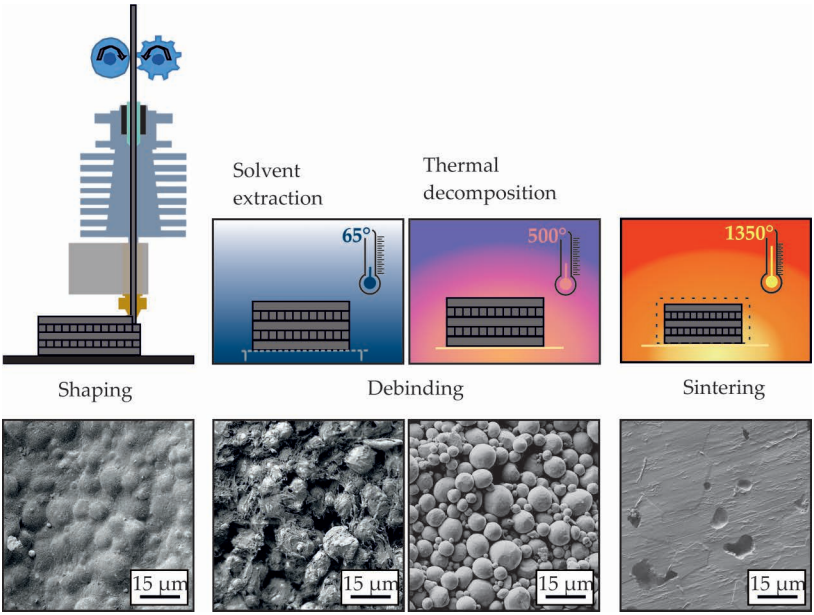

Figure 5: Schematic representation of the MF³ process and the respective microstructure of the titanium parts representative for the production of metal or ceramics: Shaping realized by FFF, binder removal through a two-step debinding process and sintering for final densification. Reprinted with permission [57].

by suitable sintering parameters and, if necessary, application of HIP. Compared to established AM processes, the densities achievable in MF³ are lower, while the homogeneity of the microstructure is advantageous over the anisotropy induced by PBF processes [89]. On the process engineering side, the significantly reduced equipment and operating costs, as well as the higher occupational safety, due to the fact that no loose powder has to be processed, are also beneficial.

With respect to conventional processing, the mechanical properties are reduced due to the relatively coarse grain structure resulting from the sintering process. However, the MF³ has great potential for high-quality materials when the focus is on a functional application. Compared to subtractive manufacturing, the material savings can allow the selection of a more expensive material with better properties, compensating for process-related strength losses.

3 Fundamentals of MF³

The MF³ process is based on the extrusion of highly filled thermoplastic filaments used for free-form fabrication of metals. It is an indirect process, which uses sacrificial polymeric binders for additive shaping of green bodies consisting of powder particles and an organic binder matrix. The polymeric binder is subsequently removed and the remaining powder is sintered. The resulting microstructure and mechanical properties of the final part are highly dependent on the choice of processing parameters.

This chapter provides the scientific background that is necessary to assess the influencing factors of the individual process steps and their mutual impact. Section 3.1 characterizes the highly filled thermoplastic filaments that serve as the base material. Additive shaping by FFF relies on the extrusion behavior of these filaments and is covered in section 3.2. Sections 3.3 and 3.4 deal with the evolution of component properties during the specific process steps of debinding and sintering. Both focus on the microstructural events responsible for maintaining and increasing the strength of the powder compact. These are important for the later discussions of the experimental results. The interacting parameters that are relevant during the different process steps are summarized in section 3.5, emphasizing the complex process-property relationship in MF³ processing.

All correlations are first treated from a general point of view, details on the specific processing of the various materials examined in this work are given in section 3.6. It shows the versatility of the process for the manufacturing of various metals and even ceramics. Finally, an outlook on multi-material MF³ is presented in section 3.7, indicating further potential for functional applications.

3.1 The highly filled thermoplastic filaments

The filaments used for printing of the green body are characterized by a high particulate content, which eventually allows the removal of the binder. Highly filled filaments with a powder content in the range of 45 vol% to 65 vol% are preferred, as the high powder fraction contributes to a high final density [81]. However, a high solids content significantly

affects the rheological behavior and complicates processing. The feedstock, which serves as the basic material for filament fabrication, is in most cases a complex multi-component system. It consists of a sinterable powder, a polymeric blend and additives. The structure of the feedstock with the individual components of the binder system is schematically illustrated in Figure 6.

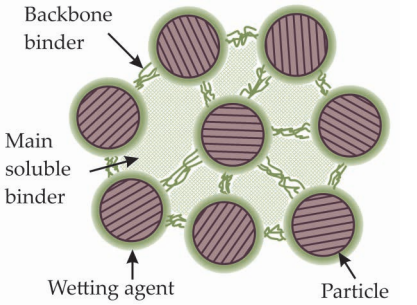

Figure 6: Schematic representation of feedstock microstructure.

The demonstrated dispersion of particles inside the binder structure is achieved during feedstock preparation prior to MF³ processing. It is conserved inside the filament and the printed green body. The feedstock production involves mixing of the powder with the molten binder constituents to create a homogeneous distribution of particles. High shear is required to break up agglomerates and increase homogeneity. To generate it, a variety of different kneaders (with Z-blades, counter-rotating rolls or twin screws) are available [81]. The structure of the powder-binder mixture is formed during compounding by the various binder components, which each occupy specific positions. In most cases three main binder types are involved:

i) The main binder component represents the largest amount (50 % to 90 %) of the total binder system and mainly determines the properties of the material during the extrusion process. It is removed first during debinding and is therefore selected to be chemically solved and extracted. Example materials are waxes [5, 90, 91], thermoplastic elastomer (TPE) [92–95] and polyethylene glycol (PEG) [96–98].

ii) The backbone polymer constitutes a stable framework that maintains the strength of the powder compact during solvent debinding. It occupies up to 50 % of the total binder and is frequently polypropylene (PP) [96, 99], low density polyethylene (LDPE) [100] or another polyolefin [13, 93–95].

iii) Additives can promote particle dispersion, lower the viscosity and prevent agglomeration and phase separation [101]. Depending on the powder chemistry up to 10 % of stabilizers, dispersing agents, coupling agents and compatibilizers can be added to the binder system. The most commonly used additive is stearic acid (SA) [81].

In combination, these binder components provide mechanical strength at room temperature and low viscosity at extrusion temperatures. Thus, the binder yields the filament properties required for MF³ processing. However, in filaments with a high powder content, strong particle interactions also influence the properties. With increasing solids content, the feedstock viscosity inevitably increases, ultimately approaching infinity at an asymptotic limit (Figure 7a) [74].

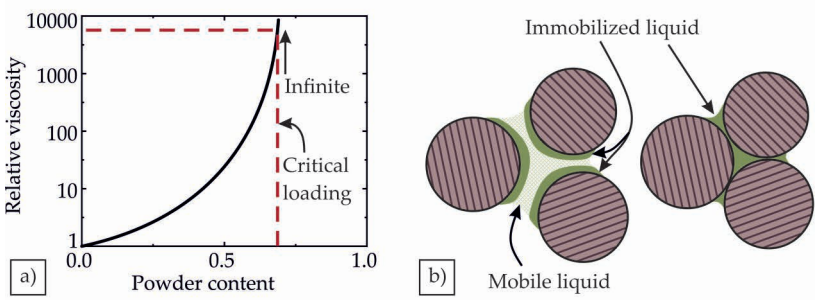

Figure 7: a) Plot of the mixture viscosity variation with powder content. Adapted from [74]. b) Schematic representation of immobile liquid between particles in contact.

The rapid viscosity change near the critical loading can be explained by the concept of immobilized liquid in Figure 7b, proposed by Vand. The immobilized liquid is the amount of binder required to fill the spaces between the particles when they are in closest packing. It corresponds to the bridging layer of absorbed organic molecules that is formed on the particle surface [101]. This binder fraction consists of coupling agents that form bonds with both the particle and the binder, and is not available for

flow processes. The immobilized liquid then contributes to an increase in the "effective" solids volume, that is proportional to the volume of particles [102]. Only excess of liquid binder beyond this immobilized fraction can contribute to reduce particle-particle friction and initiate viscous flow [103]. The effective volume fraction of the solids phase thereby becomes significantly higher than the actual volume of particles [104]. With increasing powder content, all of the remaining binder becomes immobilized and the viscosity increases sharply. At this critical powder content, the mean particle spacing approaches twice the film thickness. Close to the critical powder content, small variations in the mixture composition can be amplified into a large viscosity increase (Figure 7a). Beyond the critical content, if the binder fraction is too low, voids are formed as a result of irregularities in the mixing process. Since void nucleation requires energy, the mixture resists it by pulling the particles into close proximity, causing a sharp increase in viscosity [74]. Such filaments with too little binder content are not extrudable. To avoid problems during processing, the optimum powder content is a composition slightly below the critical value.

To increase the maximum powder loading, the thickness of the lubrication layer can be reduced. This is achieved by adding appropriate additives that promote wetting of the particle surface. Yet, the physical and chemical properties of the incorporated particles are further factors that affect the rheological behavior of the filaments. To achieve a high packing density, a small particle size and a bimodal or continuous particle size distribution are favorable [95]. On the other hand, smaller particles lead to processing difficulties as they have a higher agglomeration tendency. At the same time, a wider particle distribution can complicate the debinding process and cause an inhomogeneous microstructure. A spherical microstructure contributes to increased packing density and lowers the mixture viscosity while at the same time reducing the stability of the compound during thermal debinding [74]. Hence, powder properties can have both a positive and a negative influence on various feedstock properties. There is no optimum powder configuration and a trade-off must be found for balanced performance.

As a result of the mutual influence of powder and binder, highly filled filaments exhibit complex rheological behavior. Mueller, Llewellin, and Mader developed a model to microstructurally explain the changes in the rheology of suspensions in dependence of the particle volume fraction [105]. With increasing solids content, hydrodynamic interactions

between the particles arise and the viscosity increases. At low shear rates, the mixture behaves like a Bingham fluid, i.e. a yield stress must be exceeded to initiate viscous flow. This yield stress is a result of the formation of a network of interacting particles. Its magnitude is a function of particle size and the coefficient of friction between particles. Below yield stress, this network is capable of accommodating stress elastically until it breaks down and shear thinning behavior is exhibited during a region of pseudoplastic flow [105]. With increasing shear rates the behavior changes to Newtonian flow, that can further change to dilatant flow with shear thickening at highest shear rates (Figure 8).

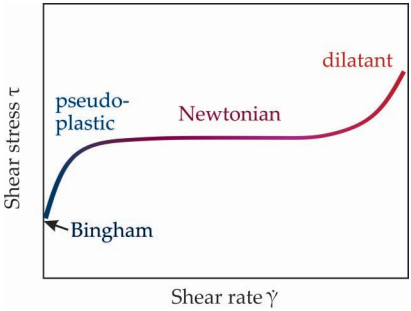

Figure 8: Variation in shear stress versus shear rate for powder-binder mixtures.

In practice, the viscosity of filaments is highly dependent on several parameters and very sensitive to changes. An engineered multi-component binder system enables shaping by filament extrusion within a range of processing conditions.

3.2 Shaping of green bodies by fused filament fabrication

Additive shaping of the MF3 green bodies is realized by FFF, i.e. by extrusion of highly filled thermoplastic filaments. The rheological behavior of filled polymers is very complex, and the development of mathematical models to allow a prediction of the flow behavior of suspensions of solid particles has been a research focus since the 1950s [102, 106–109]. During filament extrusion, the feedstock is heated inside the nozzle and viscous flow is initiated. As a result of different thermal expansion of the polymeric binder and the metallic powder particles, the effective solids

fraction is reduced during heating [74]. This contributes to a decrease of the viscosity, that enables filament extrusion as part of the printing process.

Nevertheless, particle agglomeration and, in the worst case, clogging can occur during extrusion through the narrow nozzle. Particle attraction or particle-surface interaction can promote the formation of agglomerates [110]. When entering the printer nozzle, the flow encounters a restriction due to the reduced nozzle cross-section. As the relative flow diameter decreases, the number of particle interactions increases leading to the formation of agglomerates. If a parabolic flow is assumed inside a tubular nozzle, a stable arch of agglomerated particles can form. This arch can ultimately cause clogging even if the particle diameter is small compared to the diameter of the nozzle [111]. Figure 9 sketches the formation of an arch of agglomerated particles, ultimately causing nozzle clogging. The hydrodynamic drag on particle 1 is greater than that on particle 2 because it is located in an area of higher flow and additionally shields particle 2 from the flow (Figure 9a). As a result, several accumulating particles form a blockage in the reduced nozzle cross-section, through which only part of the flow passes at a greatly reduced velocity (Figure 9b). Further particle accumulation ultimately causes clogging of the nozzle and interrupts the extrusion process.

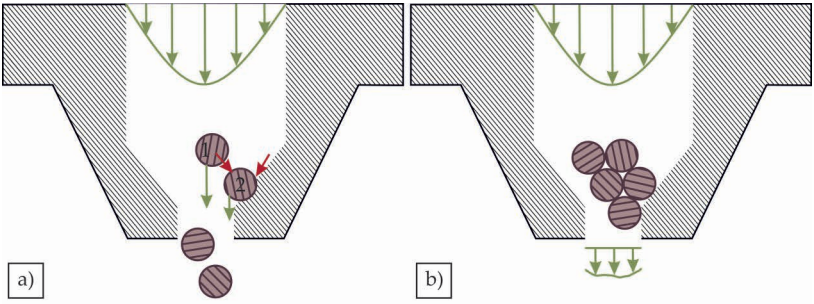

Figure 9: Development of nozzle clogging as a result of particle-particle and particle-surface interactions. a) First particle agglomeration and deposition caused by different flow forces, followed by b) blockage formation with strong reduction of flow rate.

To overcome clogging, the nozzle diameter must be large enough to allow continuous extrusion in the range of the printing temperatures

and the shear forces exerted by the downward fed filament. After successful extrusion, the viscosity of the deposited filament strands has a strong impact on the bond formation inside the printed green body. The formation of bonds between polymer layers corresponds to a sintering process [112]. Adjacent printed strands establish an interfacial contact by wetting, which is extended to form chemical bonds as a result of diffusion. The high viscosity of the deposited filament layers due to the high powder fraction reduces the molecular mobility and thus the layer-to-layer bond strength. A longer exposure to higher temperatures can enhance diffusion at the interface and the development of adhesive bonds [113]. In the scope of this work, it will be examined to what extent this beneficial effect can be generated by a reduction of the layer height during 3D printing.

Beyond interlayer bonding, a complete volume infill is a further requirement for MF³ green bodies. If the filling is inadequate, triangular flaws (marked by a red circle in Figure 10a) arise between two successive printed layers inside the components. These are formed due to the arrangement of the linear filling rotated by 90°. At the transition from the infill to the outer border, possible print defects have a rhombic shape (black circle in Figure 10a).

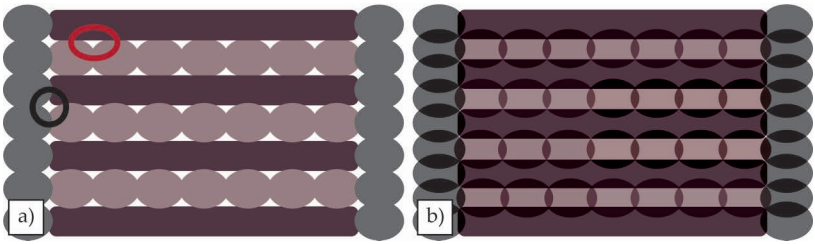

Figure 10: Schematic representation of the print pattern and pore shape a) in conventional FFF with a nominally degree of 100 % infill: Between the deposited strands pores with triangular shape are formed (red circle), while the flaws at the transition to the outline have rhombic shape (black circle). b) In case of deliberate over-extrusion, these systematic defects between successive layers are filled by excess extruded material.

To avoid these systematic defects, a deliberate over-extrusion contributes to increasing the green part density (Figure 10b). A possible increase in roughness due to over-extrusion can be reduced by post-processing operations such as laser polishing or mechanical methods on the green

part before sintering [11, 114]. To avoid these systematic defects, a deliberate over-extrusion contributes to increasing the green part density (Figure 10b). A possible increase in roughness due to over-extrusion can be reduced by post-processing operations such as laser polishing or mechanical methods on the green part before sintering [11, 114].

3.3 Debinding

Green bodies produced by filament extrusion are afterwards subjected to debinding with the aim of removing the organic binder components. Comprehensive process control is required to guarantee the stability of the powder body at all times. To avoid chemical changes in the material due to reactions with the decomposition products of the binder, complete removal of the organic content is required. In the practice of MIM, a number of procedures has been established that ensure a quick, defect-free and complete removal of the various binder components (Appendix A Table 26) [69]. In the case of the investigated MF³ green bodies, the use of a multi-component binder system allows successive debinding in a two-stage process: Solvent debinding and thermal debinding. During the first step, the main binder component is chemically dissolved and extracted. Interconnected pore channels are formed inside the parts. The second stage, the thermal debinding, involves the decomposition of the remaining organic components at elevated temperatures. The decomposition products evaporate through the previously formed pore channels, which are used as transport routes. The combination of both methods allows a reduction of the total process time. Details on microstructure evolution and influencing parameters in the course of the debinding step are described in the following sections.

3.3.1 Solvent debinding

Binder systems with only one of the components being chemically soluble in a given solvent are suitable for upstream solvent debinding. Depending on the primary binder, different solvents are available for chemical extraction. For wax-based binders that can be dissolved with, for example, heptanes or perchloroethylenes, debinding rates of 1.5 mm h^{-1} to 2 mm h^{-1} can be achieved. These are significantly higher than the rates achievable for water-soluble PEG [69]. An overview of frequently used binder-solvent combinations and the corresponding debinding rates are

listed in Table 26 in Appendix A. However, it has been shown that the rate-limiting step of solvent debinding is the diffusion of the dissolved binder to the surface. Thus, the thickness of the component and proportion of the binder polymer are additional variables that influence the duration of the solvent debinding step [62].

This first debinding step creates transport routes that facilitate the subsequent thermal debinding. The prerequisite for the effectiveness of this process is homogeneous mixing of the binders, which creates an interlocking, cohesive structure of the various components. Extraction of the soluble content then creates a continuous and interconnected open pore network. The mechanism of solvent debinding corresponds to a successive debinding that progresses from the component surface to the interior [97]. Figure 11 contains a schematic representation of the microstructure of different debinding stages.

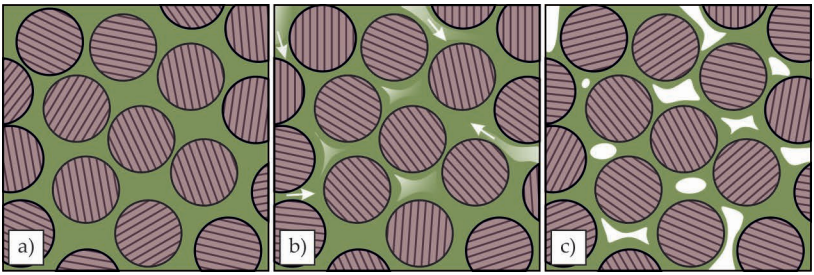

Figure 11: Schematic representation of binder distribution at different stages of solvent debinding: a) as-printed green body, b) initial stage of solvent debinding and c) final stage of solvent debinding. The hatching of the particles indicates their crystallographic orientation.

The attack of the solvent takes place on the surface and, as debinding progresses into the interior of the part, leads to the formation of pore channels. These pores become increasingly connected and form an interconnected open network that uniformly permeates the entire component. The embedded powder particles remain enveloped by the organic matrix of the backbone polymer at all times. This binder film on the particle surface constitutes a scaffold structure that guarantees the dimensional stability of the part even after the main binder component has been completely extracted [115].

The solvent debinding of the organic components is a time-dependent process and the total duration is strongly dependent on the component thickness. An elevated temperature of the solvent can have an accelerating effect [116]. From a mechanistic point of view, the solvent extraction process can be modeled as capillary liquid transport, where the driving force is the chemical concentration gradient of the binder in the solvent [117]. The degree of solvent debinding can be determined by recording the weight of the removed polymer. 99 wt% of the theoretically contained soluble fraction should be removed to create continuous pore channels and allow a quicker realization of the subsequent thermal debinding [94].

3.3.2 Thermal debinding

For final removal of all organic components, a thermal debinding step is carried out at elevated temperatures. During heating the binder is thermally decomposed into low molecular weight species, such as H_2O, CH_4, CO_2 or CO. The temperature range depends on the decomposition temperature of the polymers contained in the binder system. For the most commonly applied binder polymers, which belong to the group of polyolefins, it lies between 265 °C to 415 °C [64]. A summary of example binder polymers and their corresponding melting and decomposition temperatures is listed in Table 27 in Appendix A. The real decomposition behavior during heating can be determined by means of thermogravimetric analysis (TGA). It is influenced by the oxygen partial pressure (pO_2) in the atmosphere, since thermal oxidation accelerates the thermal degradation process, and the heating rate at which the critical temperature is approached [118, 119]. The latter must be greatly reduced in the range of the decomposition temperature of the backbone polymer to allow sufficient time for outgassing of the resulting carbon compounds and prevent deformation defects [120]. The transport takes place by permeation or diffusion through previously created pore channels. The mechanism changes to diffusion when the porosity or pore diameter increases or the temperature and thus the vapor pressure rises [121]. At all times, a balance between decomposition and removal must be maintained. Otherwise an increase in vapor pressure leads to the formation of defects and cracks [69]. The critical mass loss rate that allows polymer removal without defect formation is a function of the component

geometry and debinding atmosphere. Typical heating rates are low values around 0.5 °C min⁻¹ [122]. The resulting long debinding times can be reduced by implementing a stepwise temperature program in which the slow heating rate is applied only in the critical temperature range. These programs target a constant mass loss rate and the heating rate is adjusted accordingly [123]. The optimal heating rate can be calculated with equation 1 as a function of the temperature by using the degradation rates measured with TGA [123].

$$\frac{dT}{dt} \equiv \frac{\frac{dm}{dt}}{\frac{dm}{dT}} \tag{1}$$

In this formula, T denotes the temperature, t the time and m the mass. The term dm/dt corresponds to the relative mass loss rate for which a constant value is targeted (blue graph Figure 12b). The mass loss as a function of temperature (dm/dT) is determined experimentally by TGA measurements from the derivative of the recorded weight loss (red in Figure 12a) with respect to temperature. The term dT/dt corresponds to the targeted heating rate, which must be realized in the experiment. From this differential, the stepwise temperature profile can be determined in the form of a temperature-time curve (green in Figure 12b) by integration over time [123].

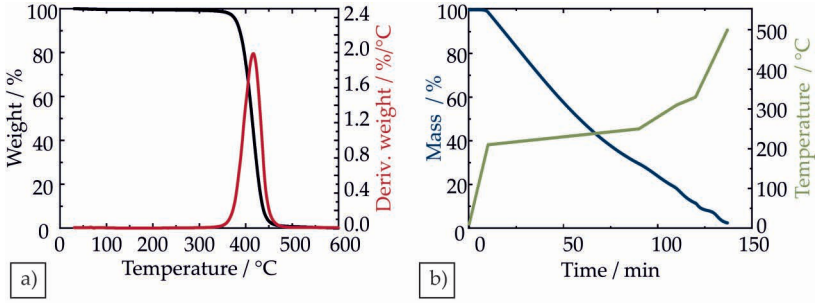

Figure 12: Derivation of a stepwise heating program: a) the measured derivative mass loss during heating is used to calculate b) the stepwise temperature profile for a selected mass loss.

The calculated heating program creates constant binder degradation that gives enough time for outgassing of degradation products and prevents the risk of pressure built-up inside the sample. Alternatively, a practical implementation of weight loss controlled thermal debinding was presented by Witt, Speyer, and Murali, where the signal from a microbalance is input through a control algorithm to control the heating rate [124].

Parallel to the slow removal of the polymer, particle rearrangements set in, which maintain the strength of the powder body. As a result, in the course of thermal debinding, the microstructure passes through different stages, as sketched in Figure 13.

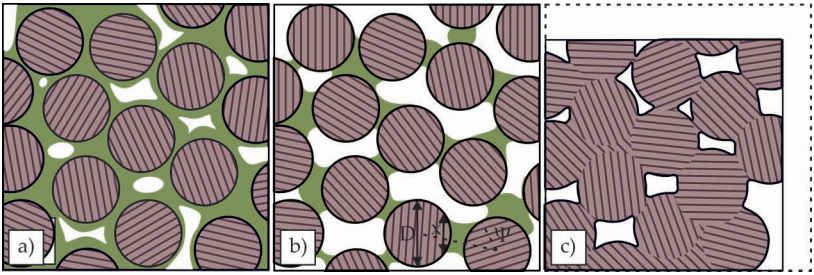

Figure 13: Schematic representation of microstructure evolution in the course of thermal debinding: a) partially debound part previous to thermal debinding (funicular state), b) intermediate state of thermal debinding (pendular state) and c) final stage of thermal debinding. In this last stage, first densification and shrinkage can be observed.

In the funicular state pictured in Figure 13a, that prevails after solvent extraction of the main binder component, the remaining organics form a coherent network traversed by pore channels. With decreasing binder content a transition to the pendular state takes place (Figure 13b). In this condition of progressed debinding, the remaining binder forms bridges at point contacts between two particles. With good wetting, these pendular bonds induce a capillary attraction between the particles. These adhesion forces depend on the pressure difference due to the curved surface ΔP, the surface energy of the liquid interface γ_{LV} and the size (X) and angle (ψ) of the liquid bond. With these variables, the adhesive force due to liquid bridges between neighboring powder particles can be calculated for the model assumption of ideally spherical particles according to equation 2 [125]. An influence of gravity can be neglected for spherical particles smaller than 1 mm [126].

$$F = \frac{\pi}{4} X^2 \Delta P + \pi \gamma_{LV} \cos \psi \tag{2}$$

Once the pendular stage is established, a small amount of the binder remains as a film on the particle surface. The only possibility to comprehensively remove all organic components is evaporation and removal in the gas phase. During the final stage of thermal debinding (Figure 13c) particle rearrangements lead to the formation of point contacts. Emerging Van der Waal forces as well as interparticle friction keep the powders in shape [69]. Particle cohesion is very weak during this stage and strengthening is achieved only later via the formation of material bridges in the form of sintering necks. These are generated by an increase in temperature directly after the removal of the organic components, which initiates the sintering activity [127]. In process engineering practice, thermal debinding is completed by a pre-sintering step, which restores the strength of the remaining powder body. Therefore, contrary to theory, the individual steps of thermal debinding and sintering cannot be clearly separated in practice. The first sintering activity at the end of the debinding phase already causes significant densification and shrinkage.

The thermal debinding process is critical in terms of producing high chemical purity of the MF3 materials. Due to the slow debinding rate and the resulting long process time at elevated temperature, the parts are exposed to atmospheric impurities for a long period of time. Additionally, the highly porous parts have a large surface area that makes them susceptible to the uptake of impurities during this step. As a result of the processing history, carbon emerging from binder degradation products and atmospheric oxygen are the main impurity elements in MF3 processing [128]. Oxide formation on particle surfaces reduces the sintering activity and must be prevented to achieve a high final density. In systems with low oxidation resistance, a low-oxygen or reducing atmosphere can be selected [129, 130].

For materials prone to carbide formation, limitation of carbon content is especially challenging and may have to be supported by the choice of a suitable atmosphere, for example, a hydrogen-containing atmosphere [131]. On the other hand, in the case of carbon-containing alloys, decarburization can occur, which in turn must be prevented by choosing the appropriate atmosphere [132].

A successful thermal debinding must use an adapted temperature program in combination with an adequate furnace atmosphere to achieve thorough binder removal. At the same time the sintering activity and chemical purity of the original powder must be conserved. Slow heating rates ensure the evaporation of binder degradation products without causing defect formation, while allowing time for particle rearrangements that restore the strength of the debound powder bodies.

3.4 Sintering

Sintering constitutes the last step in the basic MF³ process chain for fabrication of a solid component. It serves the densification of the manufactured parts. Subsequent process steps such as HIP for removal of remaining pores or heat treatment to improve properties are optional. To initiate sintering activity, a homologous temperature (defined as the ratio of the absolute temperature T to the absolute melting temperature T_M) in the range $0.5 < T/T_M < 0.95$ is chosen [133]. Starting from the debound and pre-sintered part with 35 % to 20 % porosity, the development of the microstructure passes through different stages, which are schematically shown in Figure 14.

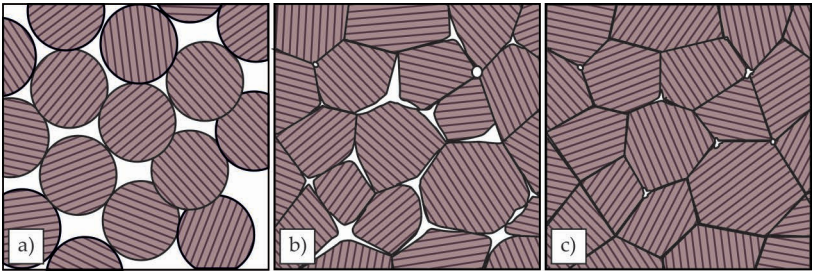

Figure 14: Microstructure evolution with ongoing sintering process: a) Initial state with neck-formation, followed by b) neck-growth and formation of grain boundaries at contact surfaces. c) Final state with remaining closed pores at triple points.

Particles that are in point contact after binder removal form first sintering necks during the initial phase of the sintering process (Figure 14a). This state is already established at the end of the thermal debinding process, and the transition to the initial sintering phase is not clearly defined in practice. The thin sintering necks grow by material diffusion

to point contacts and grain boundaries are formed at contact surfaces between particles (Figure 14b) [133]. Possible mass transport paths that provide neck growth are indicated in Figure 15a. The neck-size ratio (X/D) is a function of a kinetic term B, isothermal time t and the partical size D [134]:

$$\left(\frac{X}{D}\right)^n = \frac{Bt}{D^m} \tag{3}$$

The exponents n and m depend on the sintering mechanism and are given in Table 1. The kinetic term B is described by a Arrhenius function and depends on the temperature T associated with the mass transport, the activation energy Q and the gas constant R. B_0 is determined by material, crystal structure and geometric constants and also depends on the mass transport mechanism as listed in Table 1 [135].

Of the mass transport mechanisms sketched in Figure 15 only those that reduce the interparticle distance lead to shrinkage. When material is transported from the particle surface, i.e. by surface diffusion, neck growth occurs due to redistribution of material, but the distance between particles is not reduced. Mechanisms contributing to densification and shrinkage are volume diffusion and grain boundary diffusion, i.e. mechanisms that include material transport along the grain boundary.

Coble proposed two geometrically simple models for the shape changes of grains during intermediate and final stage sintering [136]. Initially spherical grains quickly develop regular surfaces and form the shape of a tetrakaidecahedron, as sketched in Figure 15b. With increasing densification, inbetween pore channels collapse and closed pores form at interfaces and grain boundary (GB) triple points (Figure 14c). Spheroidization of pores occurs because the surface energy of elongated cylindrical pores is at some point larger than a collection of spherical pores at GB triple points. According to the Raleigh instability criterion, pores of length L and diameter d_p become closed when $L \geq \pi d_p$. In a model material consisting of tetrakaidecahedron grains of all the same size, the calculated onset of pore closure is at 8.25 % porosity when the final sintering stage is reached [135]. Since in practice there is often a broad range in grain size and pore size, pore spheroidization occurs over a wide range of densities from 85 % to 95 %. If closed pores are attached to grain boundaries, shrinkage continues during the final sintering state. Isolated pores that

Table 1: Values of n, m and B_0 in dependence on the mechanism of mass transport during sintering neck growth [135].

Mechanism	n	m	B_0
Viscous flow	2	1	$\frac{3\gamma_{SV}}{2\eta}$
Plastic flow	2	1	$9\pi\frac{\gamma_{SV}D_v}{b^2}\frac{\Omega}{RT}$
Evaporation - condensation	3	2	$\frac{\pi}{2}^{\frac{1}{2}}\frac{3P\gamma_{SV}}{\rho_T^2}\frac{M}{RT}^{\frac{3}{2}}$
Volume diffusion	5	3	$\frac{80D_v\gamma_{SV}\Omega}{RT}$
GB diffusion	6	4	$\frac{20\delta D_b\gamma_{SV}\Omega}{RT}$
Surface diffusion	7	4	$\frac{56\delta D_s\gamma_{SV}\Omega}{RT}$

b = Burger's vector

D = Particle diameter

D_b = GB diffusivity

D_s = Surface diffusivity

D_v = Volume diffusivity

M = Molecular weight

P = Vapor pressure

Q = Activation energy

R = Universal gas constant

T = Absolute temperature

Ω = Molar volume

γ_{SV} = Solid-vapor surface energy

δ = Diffusion layer width

ρ_T = Theoretical density

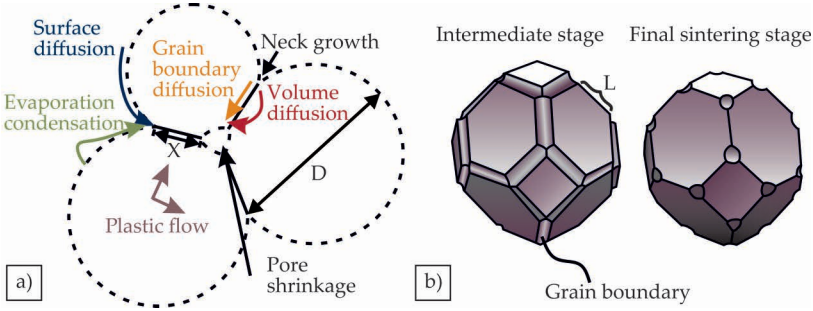

Figure 15: a) Schematic of the various mass transport paths that provide neck growth during sintering. The most common transport processes are surface diffusion, which gives no densification, and grain boundary diffusion, which creates densification. b) Coble's model of the pore and grain geometry for intermediate and final stage sintering. The tetrakaidecahedron consists of 14 sides (8 hexagons and 6 squares). In the intermediate stage of sintering the edges are assumed to be tubular pores, that in the final stage of sintering become spherical pores at the corners.

are separated from grain boundaries do not densify. These pores reach a minimum equilibrium size that depends on the prevailing internal gas pressure and the furnace atmosphere [137]. At that point the internal gas pressure P_g equals the solid-vapor surface energy γ_{SV} of the curved spherical pore of diameter d_p:

$$4\gamma_{SV} = P_g d_p \tag{4}$$

If the pore diameter at pore closure is d_1, the final pore size d_2 can be can be estimated according to equation 5 [135].

$$d_2 = \frac{1}{2}\sqrt{\frac{d_1^3 P_g}{\gamma_{SL}}} \tag{5}$$

Both possible pore-boundary configurations are illustrated in Figure 16a. Pores on the grain boundaries reduce the total grain boundary area and thus the system energy. If pores become separated, a new interfacial area is created and the system energy is increased proportionally.

As a consequence, pores at grain boundaries have a pinning effect and retard grain coarsening.

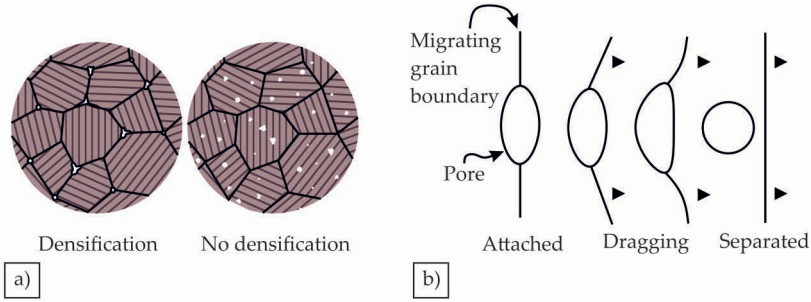

Figure 16: a) Possible pore-grain boundary configurations in the intermediate sintering stage. b) The sequence of pore isolation due to rapid grain growth during the final sintering stage. Adapted from [74].

The pinning stress σ_p exerted on the grain boundary is determined by the fractional volume of GB pores V_p and the corresponding pore size d_p and surface energy γ_{SV} according to equation 6 [138].

$$\sigma_p = \frac{3V_p\gamma_{SV}}{2d_p} \tag{6}$$

The mobility of the grain boundaries increases with elevated temperature. The less mobile pores can move under the stress exerted by the grain boundaries through volume or surface diffusion. If grain growth accelerates, however, grain boundaries can break away from the pores and leave them as isolated, spherical pores (Figure 16b) [74]. After pore isolation, further densification can only be realized slowly via volume diffusion. If gas is trapped inside the pores, the gas pressure limits the possibility of further pore elimination during sintering without application of external force. In practice a distribution width of the pore size exists due to particle size distributions and varying packing densities. Different curvature radii of differently sized pores cause a growth of larger pores at the expense of the smaller ones. Due to this Ostwald ripening the pore size of remaining pores in the final stage increases despite a slowly decreasing total porosity.

Simultaneously, grain coarsening accelerates as pores are eliminated. Grain growth is a result of diffusion between two grains of different size where larger grains grow at the expense of the smaller grains due to the lower surface energy per unit volume. Coalescence of grains is favored if the two grains have a low degree of crystallographic misorientation. Grain coarsening during sintering thus depends on microstructural features such as grain size, grain orientation, porosity and amount of secondary phases [139].

Detailed descriptions of the sintering processes can be found among others in publications of Geach, German, Weiser [137, 139–141]. These include the occurring material transport mechanisms and their respective influencing factors.

Specifically of MF³, as a result of the processing history, the parts exhibit pronounced shrinkage with shrinkage anisotropy and residual porosity after densification. The amount of shrinkage in the course of sintering is determined by the powder content inside the green body or filament. As outlined in Figure 17a, the initial powder packing density defines the amount of uniform shrinkage that is necessary to obtain the respective final density. For the powder content of 50 vol % to 60 vol % that is used in MF³ processing, a linear shrinkage of 15 % to 25 % can be expected if a relative sintered density of at least 95 % is achieved.

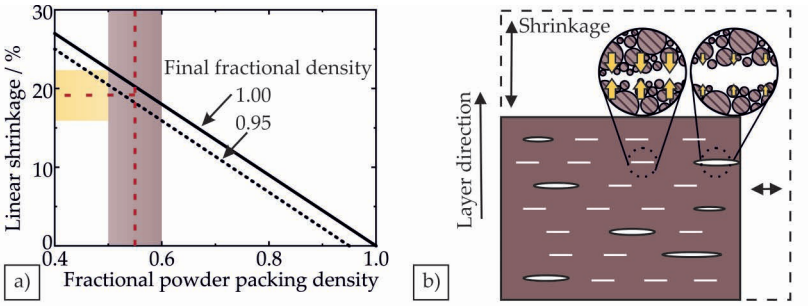

Figure 17: a) Plot of linear shrinkage versus initial powder packing density. The packing density range between 50 % to 60 % that is relevant for MF³ is highlighted in color. b)Influence of the layered structure on the shrinkage behavior of parts fabricated through MF³. The original dimension of the green body is indicated by the dashed line.

In practice, the linear shrinkage of brown bodies produced by FFF is not equally pronounced in all spatial directions. For the shrinkage in z-direction, i.e. up to 10 % higher values are measured in this built-up direction compared to the lateral shrinkage. One possible cause of this anisotropic shrinkage is the effect of gravitational force on the loose powder particles that causes particle rearrangements and denser powder packing in z-direction [142]. However, the effect of gravity is negligibly small for the case of the very small particles used in MF³ [126]. As the difference in shrinkage is very pronounced a more likely explanation lies in the anisotropy of the green body filling that emerges from the layered character of the FFF. While particles are densely packed within the extruded filament strands, distance between particles from adjacent deposited strands is larger. Densification towards a uniform relative density correspondingly produces increased rearrangements and shrinkage in that direction. If at certain points the distance between layers is too big, particle spacing can occasionally be too large, so that densification is no longer possible. In this case, systematic printing pores remain in the part even after the sintering process is completed [143]. This phenomenon is shown schematically in the sintered part of Figure 17 b. The original dimension of the green body is indicated by the dashed line. Accordingly, the amount of shrinkage and the degree of shrinkage anisotropy during sintering can be influenced by increasing the homogeneity of the FFF green bodies.

A prerequisite for sintering processes is the initiation of material transport between the particles in contact. Oxide layers on the surface, that are not removed under sintering conditions, act as a diffusion barrier and significantly lower the sintering activity [144]. Because of their small particle size and the resulting large surface, the powders used in MF³ are more susceptible to oxidation. If continuous oxide layers are formed, diffusion and thus the sintering process can be completely inhibited. A sintering atmosphere of low pO_2 such as vacuum is for this reason often applied to prevent oxide formation. Alternatively, previously formed oxides can be reduced by using H_2-containing atmospheres.

Sintering, as part of MF³ processing, must be performed at sintering temperatures and sintering times that are matched to the particular metal being processed in order to achieve optimum densification. The appropriate atmosphere avoids the formation of oxide layers at high temperatures, or enables a reduction of existing oxide layers on particle surfaces to prevent a sintering-inhibiting effect of oxides. Successful

initiation of material transport processes results in densification and pore elimination under shrinkage. Due to their high porosity, shrinkage of MF³ parts lies between 15 % to 25 % depending on the powder content in the filament. Due to the layered structure of the printed samples, shrinkage is mostly anisotropic and more pronounced in the z-direction. Typical for sintered material, MF³ metals have a relatively coarse microstructure with residual porosity after pressureless sintering.

3.5 Process-property relationship

The properties and performance of MF³ components depend on the composition, the sintering density and the resulting microstructure. The composition depends on the processing cycle and atmospheric influences during debinding and sintering, while the density is determined by the starting material and the debinding and sintering program. These dependencies are conceptually visualized in Figure 18.

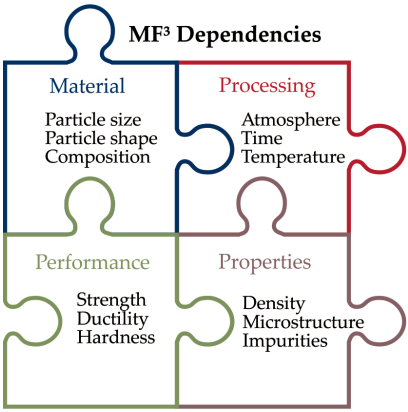

Figure 18: Schematic representation of the process-property relationship in MF³ processing.

For good performance, thorough densification must be generated during sintering, since the final density has a direct influence on the properties of the component. A higher degree of sintering improves properties such as hardness, strength, ductility, electrical conductivity and magnetic saturation [74]. The sensitivity of each of these properties to the degree of sintering is different and schematically sketched in Figure 19.

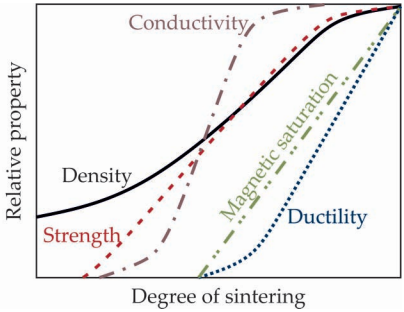

Figure 19: Schematic representation of the dependence of component properties on the degree of sintering. Adapted from [74].

Sintering can therefore be regarded as the critical step for the MF³ production of good quality components and must be given special consideration during process development. The obtained sintering densification is strongly influenced by atmospheric oxygen, as formed oxides retard material transport processes [130]. Depending on the oxygen affinity of the material, considerable oxidation can occur during filament production, at the increased temperatures during thermal debinding or during the sintering process. For high sintering activity during the final MF³ step, an atmosphere of low pO_2 is already required during thermal debinding [145]. In contrast, the absence of oxygen in the atmosphere retards the thermal decomposition of the binder polymers during thermal debinding. Thermogravimetric analyses in oxygenated and low-oxygen atmosphere show a delayed decomposition of the organic molecules without oxygen that results in an increased decomposition temperature [146]. This leads to competing relations between the interaction of atmospheric oxygen with the powder surface and the interaction with the binder polymer.

Independently of individual process steps, diffusion of atmospheric elements into near-surface regions of the components is not desired along the entire MF³ process chain in order to maintain a high chemical purity of the processed metals. At the same time an evaporation of alloying elements should be avoided to prevent process-related changes in the composition [69]. To balance these opposing conditions, the control of the atmosphere is particularly important, and its adaptation to the processed material is critical.

The key factor for fabrication of high quality MF³ parts is the control of the interaction of the powder with the atmosphere, always with the focus on conserving the sintering activity. Resulting obstructions on binder decomposition must be balanced by higher temperatures or longer process times to optimize the density and purity of the final product [145].

3.6 Metal fused filament fabrication of specific materials

In MF³, the properties of the powder and binder materials dictate which processing measures are to be selected for the specific material. Contradicting interactions during filament extrusion, debinding and sintering often require finding a trade-off between reduction of processing time and enhancement of final part properties. Different materials can only be successfully processed after adjusting of the sintering parameters and the furnace atmosphere. However, if the parameters are chosen precisely, the process is very versatile and, in addition to metals, can even be used for the additive manufacturing of ceramics [147].

Relevant characteristics of the ceramics and metals investigated in the scope of this work are summarized in the following section. During FFF and debinding, processing parameters apply for all materials since these steps depend only on the binder system used and the powder content of the filament. During thermal debinding and sintering, atmospheric influences must be reduced in line with the material to reduce impurity uptake.

3.6.1 Processing of ceramics

Ceramic powder often has an irregular particle shape due to the synthesis process [148]. Typical average particle sizes are 1 µm to 2 µm [149]. In many cases, ceramic particles consist of agglomerates, i.e. clusters of particles in the submicron or nano range [148]. As a result of an irregular particle shape, the viscosity of the filament is higher than with spherical particles at the same volume fraction [101]. To overcome the high viscosity, additional measures may be required during printing. When using a conventional filament extruder, for example, increasing the printing temperature or using a larger nozzle diameter are suitable options. However, studies have also shown that improved mixing can enable the

extrusion of highly filled ceramic suspensions through small nozzles < 100 µm [150]. During the following debinding step, the irregular particle shape leads to increased inter-particle friction, inducing a high shape stability of partially debound parts [151]. From a chemical point of view, the inertness of the ceramics and the resulting low oxidation tendency allow processing in oxygen-containing atmospheres. This contributes to accelerating the thermal debinding process and consequently reducing process times [146]. During sintering, high temperatures must be applied to account for the high melting point. The small particle size in the low micrometer range has a positive effect, as it results in increased sintering activity [152].

Al_2O_3 was chosen as an example for the processing of ceramics. Literature suggests a sintering temperature between 1400 °C to 1500 °C to reach high relative density and limit grain growth [153]. Since Al_2O_3 is not susceptible to impurity uptake due to its chemical inertness, the ceramic should be well suited for MF³ processing if an extrudable filament is available for green body shaping by FFF.

3.6.2 Processing of steels

The investigated gas-atomized steels have a spherical particle shape. This implicates a relatively low filament viscosity and good printability in desktop filament 3D printers. The high sphericity and smooth particle surface reduces inter-particle friction and requires low heating rates during thermal debinding to maintain dimensional stability [74]. Steel powders are susceptible to oxidation at elevated temperatures. Consequently, vacuum or process gases are required during thermal debinding and sintering [154]. Apart from oxidation, decarburization of the steel alloy must also be prevented by choosing the appropriate furnace atmosphere and temperature program [155]. Due to the broad variety of different steels, atmospheres and sintering programs must be chosen specifically for each alloy.

The X2CrNiMo17-12-2 austenitic stainless steel 316L is a low carbon type that forms discontinuous polyhedral oxide particles at elevated temperatures [156]. As these oxides reduce the sintering activity, the furnace atmosphere has a decisive influence on the achievable sintered density. Many studies have investigated the optimum sintering atmosphere to

avoid oxidation, but come to contradicting results [157–159]. Nevertheless, high relative densities above 95 % are obtained if temperature, time and atmosphere are appropriate. An increasing sintering temperature and time results in a decrease in porosity by pore elimination along with grain coarsening [160]. Additionally relevant to MF³ is the formation of GB chromium carbides of the $M_{23}C_6$ type at temperatures between 500 °C to 700 °C, which are in the range of thermal debinding. This results in the formation of Cr depleted regions along the grain boundaries, that make the steel susceptible to intergranular corrosion [161]. Thus, the limitations of oxidation, carbide formation and grain growth emerge as the critical factors in MF³ processing of 316L.

Tools steels, as the investigated X40CrMoV5-1 hot work tool steel Ampersint 1557.02 contain higher amounts of carbon. During sintering, the onset of densification is strongly dependent on reduction of surface oxide layers during heating. Depending on alloying elements, reduction of tool steels occurs in different temperature ranges and is more or less pronounced [154]. While carbon generally enhances deoxidation by carbothermal reduction, the contained chromium increases the thermodynamic stability of oxides and shifts reduction to temperatures above 1000 °C [162]. Additionally, elements with high oxygen affinity can act as oxygen getters and lead to a transfer of gaseous reduction products from iron oxides to oxygen sensitive alloying elements [163]. Thus, atmospheres and heating rates during sintering must be adjusted to avoid oxygen transport inside the material and obtain high densification with low amount of evenly distributed residual pores.

Sintered MF³ parts are subjected to a multi-step heat treatment including hardening and tempering. During this process, as well as during sintering, the initial carbon content must be conserved to achieve the microstructure and hardness required for application [164]. If decarburization can be prevented, the final microstructure is either composed of tempered martensite and bainite or shows a pearlite-bainite structure [165, 166]. Targeted hardness values lie between 480 HV to 520 HV in the quenched and tempered (Q & T) state.

Maintaining the carbon content during sintering and heat treatment by selecting suitable atmospheres and process parameters is thus crucial for the MF³ production of tool steel with high strength and good ductility.

3.6.3 Processing of titanium

In MF³ processing of commercially-pure ti-tanium (Gd. 1 as per ASTM F67 [1]) the high tendency to oxide formation requires the application of protective gas or vacuum during filament extrusion to avoid preliminary oxidation of particle surfaces. Likewise, processing at elevated temperatures must be realized in atmospheres of low pO_2. In vacuum, the reduction of oxide layers and onset of sintering takes place at 700 °C [167]. Accelerated densification is achieved by making use of the α-β transformation. Cyclic sintering by repeated heating above and below the $\alpha \rightarrow \beta$ transformation temperature 882 °C provides strain, defects and interfaces for enhanced diffusion in the 800 °C to 1100 °C temperature range [168]. Microstructure after sintering is multi-phased with an α-Ti matrix and oxygen induced retained α-phase dispersed inside the bulk material. A hard surface layer of oxygen stabilized α-phase (*α-case*) is formed, that is less ductile and can result in the formation of surface cracks under tensile loading [169]. If iron enriches at grain boundaries, the *β*-phase is stabilized at room temperature [170]. Consequently, lamellar grain boundary β-Ti is often observed in sintered titanium.

The challenge in MF³ manufacturing of titanium is thus the conservation of chemical purity to avoid secondary phase formation induced by oxygen impurities, that reduce mechanical strength.

3.6.4 Processing of nickel-base and cobalt-base superalloys

Nickel- and cobalt-based superalloys exhibit increased high-temperature strength as a result of precipitation strengthening. Nickel-based alloys are currently the most commonly applied materials in the high-temperature range [171]. Their increased high-temperature strength results in particular from a high volume fraction of coherent γ' precipitations. In addition, high proportions of Cr and Al provide high oxidation resistance up to elevated temperature ranges [172]. Cobalt-base superalloys were first identified by Sato et al. that discovered the possibility of precipitation strengthening in the Co-Al-W ternary system [173]. Since then, research efforts have investigated the influence of Al and W addition on the high-temperature stability of the strengthening *γ'* (Co_3(Al, W))precipitates [174, 175]. Ti and Ta as additional alloying elements can increase the γ' solvus

temperature and improve the mechanical properties at high temperatures [175–178]. Within the scope of this work, two different alloys were investigated, on the one hand the widely-applied nickel-base alloy Inconel™alloy 718 (IN 718) and, in addition, a novel cobalt-base superalloy developed during research at the Friedrich-Alexander-Universität Erlangen-Nürnberg (FAU).

Inconel™alloy 718 is the most used nickel-base superalloy and thoroughly investigated for manufacturing by MIM processing [179–185]. Highest densities were obtained by processing in vacuum at a temperature range of 1260 °C to 1290 °C that allows for liquid phase sintering [186]. After heat treatments, sintered IN 718 is strengthened by finely dispersed γ" (Ni_3Nb) and γ' ($Ni_3(Al, Ti)$) intermetallic precipitates. An increased amount of impurities as a result of the processing history can lead to formation of carbides and oxides, often in the form of prior particle boundarys (PPBs) [76]. If located at grain boundaries, oxides and carbides impede grain growth and can contribute to a fine-grained microstructure. Thus, an acceptable concentration of grain boundary carbides and borides can improve mechanical strength, but too large amounts of high-temperature stable carbides can act as crack initiation sites, reducing mechanical strength [187].

Regulation of carbide formation and grain growth as a result of processing are the crucial factors to enable successful MF³ fabrication of IN 718. The sintered material requires an additional heat-treatment to generate the precipitation of γ" and γ' phases and enhance high-temperature mechanical properties.

Co-base superalloys of the Co-Al-W ternary system exhibit an ordered precipitation phase similar to the ni-base superalloys [173]. The hardening γ' phase is a $Co_3(Al, W)$ precipitate which is metastable [188] and therefore reverts to the equilibrium phases χ-Co_3W, μ-Co_7W_6 and β-CoAl at longer ageing times. To make co-base alloys suitable for high-temperature applications, a series of different compositions were produced at FAU as part of Lisa Freund's doctoral thesis, and the influence of various alloying elements was investigated [189]. For improved strength, the Co-base superalloy 3 with increased Mo content (CoWAlloy3) alloy was developed with an increased content of molybdenum to promote the formation of the grain boundary pinning μ-phase ($(Co, Ni, Cr)_7(W, Mo)_6$). Besides the increased Mo content, the CoWAlloy3 is strongly based on the Co-9Al-9W ternary system, i.e. it uses mainly Al and W as γ'-formers [189].

The resulting alloy has good forgeability, which also makes it attractive for additive processing in PBF processes.

The conventional method of producing cobalt-based superalloys involves wrought processing of polycrystals [190–192]. Alternatively, single crystals are often produced by Bridgman growth [193]. To make cobalt-based alloys available for additive manufacturing, investigations in recent years have focused on alloy development that enable LPBF and EPBF [194, 195]. In parallel, powder metallurgical production routes that include a sintering step are also investigated [196–198]. Efforts in alloy development at FAU focused on the introduction of a GB pinning phase to inhibit grain growth in polycrystalline co-based superalloys [191].

When establishing a MF³ processing route for AM of cobalt-base superalloys, the focus lies on maintaining a small grain size while achieving a high volume fraction of γ' phase for high mechanical strength. In addition to appropriate sintering parameters, a heat treatment must be applied.

3.6.5 Processing of copper

MF³ of pure copper is particularly attractive since powder-bed methods for additive manufacturing of this material are challenging. Due to its high thermal conductivity of 400 $W\,m^{-1}\,K^{-1}$ at room temperature and the high reflectivity in the near infrared (IR) laser sintering is difficult [26, 199]. Many studies have made AM of pure copper available by implementation of new laser parameters or making use of green lasers for enhanced energy introduction into the copper powder material [200–204]. As an alternative to laser melting techniques, EPBF was proven to be successful for the fabrication of 99.9 % pure copper of high density [48, 49, 205]. However, all of these powder bed processes require high investments and energy consumptions.

As an alternative, Binder Jetting that fabricates parts via selective binder deposition into a powder bed was investigated as a cost-effective production method of complex copper parts. The printed green bodies are then sintered for densification. Final relative densities of 85 % to 92 % can be obtained after pressureless sintering by optimization of powder morphology and process parameters [206, 207]. Application of HIP as a post-process step allows further densification to 99.7 %, yet leads to an anisotropic linear shrinkage due to graded density in the green part [207].

Since copper powders are prone to oxidation, a control of the sintering atmospheres is crucial for optimized densification. While thin films of copper oxide of 40 nm to 60 nm show activated sintering, thicker layers that reduce the oxide-to-oxide contacts have an inhibiting effect [208]. The continuous oxide layers require an incubation period to initiate sintering activities and result in weak densification unless reducing atmospheres are used to remove the oxide layer and restore diffusion [209].

For this reason, thermal debinding and sintering in MF³ of copper must be conducted in suitable atmospheres that prevent oxide formation and maintain high sintering activity to achieve a high final density.

3.7 Multi-material additive manufacturing

The ability of fabricating composites from multiple materials can enhance additive manufacturing processes by either optimizing the mechanical properties or increasing the functionality of finished parts. However, multi-material AM is challenging and a fundamental advantage of certain AM technologies [210].

MF³ offers the possibility of multi-material AM if the same binder system is used in all combined filaments. In this case, the shaping by FFF poses no difficulty since similar polymers form a cohesive bond [211]. This means that during the combined extrusion of two different filaments, a solid interface is created between the two phases. The shaping of composite green bodies can therefore be easily realized if multiple nozzles are available for extrusion and the printing parameters of the individual materials are known [212]. In solvent debinding, the solvent extracts the main binder polymer equally in both phases. The different densification behavior of the materials has to be taken into account only during thermal debinding and the atmospheres and temperature program have to be adjusted to maintain the geometric stability of the two phases while the backbone polymer is removed [213]. The challenge in multi-material MF³ lies in the sintering step, i.e., achieving a high sintering density in both materials while simultaneously forming a stable interface [214]. Influencing factors on this decisive co-sintering are covered in detail in section 3.7.1.

If no stable interface is formed during sintering, separation of the different phases is possible at the end of the process chain. In this case, the material of higher sintering temperature can be used as a support

structure to enable the fabrication of complex geometries. More details on the application of separable supports, first introduced and meanwhile patented by Desktop Metal™, is given in section 3.7.2 [215, 216].

3.7.1 Additive manufacturing of composites

Multi-material MF³ for fabrication of composites must create high densification of the individual phases while simultaneously achieving a strong interfacial bonding. A prerequisite for this is successful co-sintering, which requires a general matching of material properties [214]. Simchi, Petzoldt, and Hartwig proposed a model to estimate the co-sintering capability of a material combination considering thermal expansion, shrinkage and sintering temperature [217]. The formation of a strong interfacial adhesion is only possible if a chemical bonding can be achieved, either directly between the different phases or through the formation of a connecting interlayer by diffusion [92, 218]. During processing, the coefficients of thermal expansion should be in a similar range to avoid internal stresses and resulting defect formation [214]. This applies to heating during thermal debinding and sintering as well as to the cooling step. In the latter case, cracks could otherwise occur along the newly formed interface due to shrinkage differences during cooling. To achieve similar shrinkage in both phases, the powder contents of the two filaments should be matched to each other during the preceding filament fabrication [74, 219]. Otherwise, if the net shrinkage of the individual phases is strongly differing, stresses emerge at the interface, leading to cracking and delamination. Investigations on co-sintering of ceramic compounds revealed that shrinkage differences are critical especially during the early sintering stage, where the strength of the compound is still low [220, 221]. This mismatch in the initial stage is attributed to different sintering start temperatures. Besides, two further mismatch types can be distinguished for a two material combination as sketched in Figure 20 [222].

During intermediate sintering, mismatch occurs if the temperatures of the maximum shrinkage rate differ (Figure 20b). Mismatch in the final stage is attributed to different net shrinkage resulting from different powder contents in the green state. This latter case can be influenced by matching the infill levels of the filaments and is only negligibly influenced by the behavior of the different materials [74].

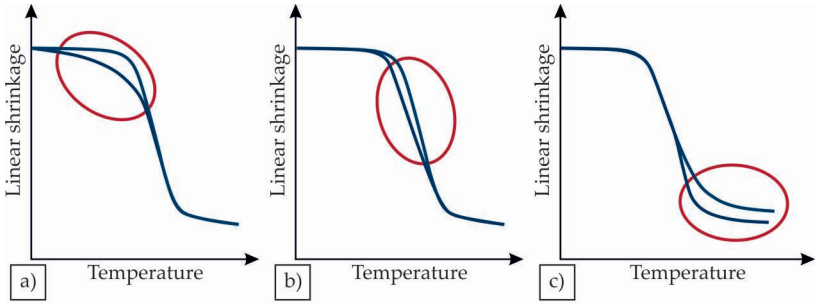

Figure 20: Shrinkage mismatch types for a two-material-combination according to the sintering stages: a) Different starting temperatures, b) different temperatures of maximum shrinkage rate and c) different final shrinkage. Adapted from [222].

Brooks et al. studied the co-sintering potential of several material combinations to evaluate their potential for multi-material 3D printing. They identified a number of material combinations, based on similar sintering temperatures and shrinkage behavior of the individual materials [214]. The sinter start temperature depends on the material and correlates with the melting point. If materials with different sintering behavior are to be combined, a possibility is to change the powder particle size, since smaller particles have a higher sintering activity due to their larger specific surface area. Using this approach, metal-ceramic composites have been successfully shaped and sintered by MF³ [92, 213].

The challenge in MF³ of composites lies in matching the sintering parameters and shrinkage behavior of the materials which are joined to form a green body by multi-material FFF. If successful co-sintering can be achieved and a strong interfacial bonding is created, composites can be produced from all compatible powder materials.

3.7.2 Additive manufacturing of complex geometries

AM is widely applied to generate complex, customized parts that are not processable by other means. However, intricate geometries often contain overhanging regions that must be supported during the printing process. Subsequent removal of support structures requires manual and cost-intensive post-processing. Jiang, Xu, and Stringer collected numerous publications regarding support structure optimization according to the 3D printing method used [223].

In case the shaping is realized via FFF, material can only be deposited on existing underlying surfaces. Further debinding and sintering as part of MF³ processing requires supports to preserve the geometric shape during binder removal and densification. The printing of support material extends the overall processing duration, and the removed structures usually result in waste material. In addition, the removal of support structures introduces a higher surface roughness [223]. Some studies therefore focus on reducing the required amount of support material by intelligent part orientation and bio-inspired tree-like design of supports [224, 225].

Multi-material MF³ opens up new possibilities for the design of support structures. If two materials with non-compatible sintering windows are combined, sintering can result in only one of the two materials being properly densified. The use of support material with a sintering start temperature significantly higher than that of the base material makes it possible to obtain a loose state of the support structure at the end of the process. It can then be separated from the densified component with little force. This method has in recent years been established and patented by the company Desktop Metal under the Separable Supports™ technology [215, 216]. It makes use of a Ceramic Release Layer™ applied at the interface between component and support structure, which desintegrates during sintering enabling easy removal of support material [226]. A side effect of the use of ceramic powders is a reduction in material loss, which could be increased by building the entire support structure from ceramics. Since the metallic base materials are more valuable than the ceramics, significant cost savings can be achieved in this case. A drawback in using hardly sintering material as a support structure is the strong shrinkage differences that can arise between the component and the support structure during processing. Due to these differences, stresses can be exerted on the component that can lead to the formation of defects [214]. It is therefore necessary to evaluate the amount of ceramic material that can be used in the support structure without the risk of stress formation.

The task of support structures for MF³ of complex geometries is to provide sufficient support for overhanging areas without inducing internal stresses due to the different shrinkage behavior. If ceramics can be used suitably, they have the potential to build easily removable support structures, reducing manual post-processing and contributing to material and cost savings.

4 Aims and scopes of this thesis

NNS manufacturing via MIM has grown to become an established and well investigated fabrication method that finds wide application for a broad variety of materials. Today, it is the process of choice for large quantity production of small to medium part size [69]. The upcoming trend towards personalized items requires flexible production and opens a demand for form-free manufacturing methods. Additive manufacturing is of growing interest at this point, enabling customized fabrication at short lead time [25]. The drawback of most metal AM methods is the high cost caused by expensive equipment. The MF³ with its process chain similar to MIM seems to be predestined to close the gap for economical and at the same time flexible manufacturing.

For a reliable application of the MF³, a careful control of processing parameters is necessary in the course of the entire process chain. Profound knowledge of microstructural evolution, process-related influencing factors and material properties is required. It is thus the aim of this work to develop a stable process control, capable of fabricating additively shaped parts with low process-induced defects or impurities. Each step along the process chain is therefore studied separately to understand the isolated influence of varied process parameters during shaping (chapter 6.1), debinding (chapter 6.2) and sintering (chapter 6.3). In these chapters considerations are made independent of the powder material processed. After implementation of a stable process route, the applicability for the fabrication of different metals is the focus of chapter 6.4. Special importance is placed on the selection of suitable sintering parameters for each individual powder, since these have a decisive influence on the achievable final density and component properties.

316L stainless steel was used as the basis for process optimization, due to its low carbon content, single-phase microstructure and good oxidation resistance. Other metals were selected to cover a wide range of functional properties.

- X40CrMoV5-1 hot work tool steel was investigated as a structural material for tool production to benefit from high design flexibility at low production costs. It requires precise control of the carbide content to ensure that the high strength and hardness required for the application can be achieved during subsequent heat treatment

- High-temperature superalloys enable higher efficiency of gas turbines thanks to their high operating temperatures. When manufactured by MF³, they can also find novel applications since the cost-intensive machining of conventional production is no longer required. In addition, the reduced consumption of raw materials improves the economic production of superalloys. By economical additive manufacturing, superalloys can replace heat-resistant steels in small and complex components in chemical plants
- Titanium is of interest for various technical applications due to its high specific strength, low density and excellent corrosion resistance. For electrochemical applications, high-purity titanium is used in the form of thin, porous plates in electrolyte fuel cells
- Pure copper exhibits outstanding physical properties, especially highest electrical and thermal conductivity. Therefore, it is widely used as a functional material in electronic systems and for applications where rapid heat transfer is required. Due to its high thermal conductivity, it is very difficult to process in PBF systems, making sinter-based MF³ a promising alternative

For all materials, manufactured parts are analyzed with regard to their chemical purity after completion of the MF³ process chain. A mechanical characterization of the metallic specimens is carried out and in each case a comparison is made with conventionally manufactured material.

As an outlook, a proof-of-concept of multi-material manufacturing for functionalization is given in chapter 6.5 pointing at further use cases of MF³. The material combinations investigated were selected as examples either on the basis of the compatibility of their co-sintering behavior or with regard to their functional properties.

- Composites of 316L & IN 718 represent a material combination with matching sintering temperatures, which should benefit co-sintering
- Composites of copper & Al_2O_3 combine materials with strongly differing electrical conductivity. This material combination represents the feasibility limit of the multi-material MF³ spectrum due to the strongly different sintering behavior
- Ceramics are tested as a separable support structure for fabrication of complex steel geometries

5 Materials and methods

Within this section, the components and composition of the processed filaments are characterized and the procedure and parameters of the individual process steps are described. Afterwards, the methods used to characterize the chemical composition and microstructure of the manufactured components are presented. In the last section, the measurements used to evaluate the mechanical properties are described. Unless otherwise stated, the work was carried out at the Chair of General Material Properties at FAU.

5.1 Chemical composition of the highly filled filaments

The three-component binder system chosen for all filaments under investigation in the scope of this work was developed at the institute of Polymer Processing at Montanuniversität Leoben (MUL) [94]. In combination, the two main constituents provide the mechanical flexibility and stiffness, that are necessary to spool and feed the filament into the extruder. The major fraction of the binder is a thermoplastic elastomer (TPE, Kraiburg TPE GmbH & Co. KG, Germany) that is soluble in cyclohexane and thus makes the binder available for solvent debinding. The second component, the backbone polymer is an insoluble grafted polyolefin (PP, BYK Chemie GmbH, Germany), providing stability of the partially debound part after solvent extraction. The PP was functionalized with maleic acid anhydride (MA, Scona TPPP 9212, Byk Chemie GmbH, Germany) to enhance wetting of powder surfaces and homogenization of the powder-binder mixture. The exact composition is kept confidential as the formula of an adequate binder system is essential to allow the extrusion of filaments with a high amount of powder and is thus crucial for the success of the MF^3 process.

Most filaments were prepared with a powder content of 55 vol%. Only in case of the tool steels a study of the influence of powder loading on processing and final results was conducted and the amount of incorporated powder was therefore varied from 50 vol% to 60 vol%. Generally, a particle size below 45 µm was chosen for all metal powders to enable high particle packing and limit the filament viscosity. To reduce agglomerations, the smallest accepted particle size was 5 µm. Particle size distributions and

powder specifications of the specific materials processed in the scope of this work were measured by optical particle size analysis (Camsizer XT, Retsch Technology, Germany) at Volkswagen AG. Results are given in the respective sections starting from chapter 6.4. Spherical, gas atomized powders were chosen for all metallic materials. As a result of powder synthesis, the Al_2O_3 powder had irregular particle shape.

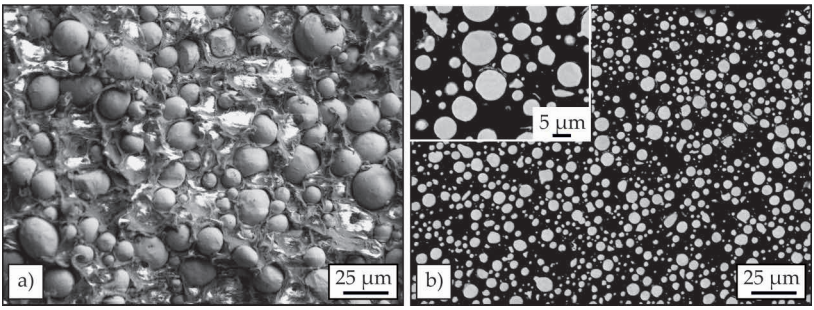

Figure 21: Representative filament cross-sections: a) Fractured surface of titanium filament. Powder particles are embedded into the polymeric binder matrix. b) Polished cross-section of Ampersint 1557.02 filament at different magnifications. The overview image shows the homogeneous distribution of powder particles inside the filament. The close-up in the upper left corner proves good powder quality with no internal porosity.

Representative cross sections of metal filaments are shown in Figure 21 for the examples of titanium and Ampersint 1557.02 tool steel. For all used filaments, homogeneous particle distribution was created and agglomeration of particles could be successfully prevented. The targeted powder content of 55 vol% was achieved for all metal-filled filaments except for IN 718, that contained only 52 vol%.

5.2 Extrusion-based additive manufacturing

The process chain of MF³ includes the production of the green body by filament extrusion, the removal of organic binder components and finally, densification by sintering at high temperatures. Details on the equipment used for processing and all relevant processing parameters are the content of the following section.

5.2.1 Shaping of green bodies

The used highly filled filaments are suitable for extrusion with conventional FFF 3D printers. The majority of the samples in this work were fabricated using the Prusa i3 MK2 model (Prusa Research, Prague, Czech Republic). In order to maintain the print quality and to account for the increased wear of the printer components due to the abrasive effect of the embedded particles, some parts were replaced with higher strength components. The nozzle was changed to either an E3D hard metal nozzle (model V6, E3D-Online Ltd., Chalgrove, UK) or a olsson ruby nozzle (3DVerkstan AB, Solna Sweden), which are available in diameters of 0.6 mm and 0.8 mm respectively. Both nozzle materials have good abrasion resistance and the ruby material additionally possesses high thermal conductivity. The original brass filament drive gear for feeding the filament into the extruder was replaced by a stainless steel gear of higher strength. The selected printer model has a heatable print bed, which facilitates the bonding of the first print layer. The maximum temperature of the heating bed is 100 °C, and the nozzle can be heated up to 300 °C.

A spindle-driven Panowin F1 printer (Panowin Technologies Co Ltd. Shanghai, China) was modified for dual printing of two different filaments. The original nozzle was replaced by the E3D Chimera 2-nozzle extrusion unit (E3D-Online Ltd., Chalgrove, UK). A second stepper motor (NEMA 17, 42 mm x 42 mm, 0.5 N m with 1.8° full step angle) was added to feed the filaments. The static components for mounting the extruder unit and the motors were designed with Autodesk Fusion 360 (Autodesk Inc., CA, USA) and manufactured from ABS on a five-axis CNC milling machine (Pocket NC V2-10, Bozeman, MT, USA). The printer control board was replaced by an Arduino Ramps 1.4 (Arduino SRL, Torino, Italy) and the Marlin 3D printer firmware (under the GNU General Public License [227]) was installed and individually adapted for operation in dual-nozzle mode. Finally, a heated bed was installed.

Printed models were constructed with Autodesk Fusion 360 and the slicer Software Simplify3D (version 3.1.1, Simplify3D, Cincinnati, OH, USA) was used for generation of the machine-readable G-Code. Simple cylindrical specimens with a height of 4 mm or 6 mm and a diameter of 20 mm or 23.5 mm were selected for the investigation of process parameters and material properties. All samples were printed at nominally full infill, using alternating linear and concentric patterns with an infill overlap of 20 %. The outer wall consisted of two concentrically printed

circumspheres in each layer. Other printing parameters were systematically varied and optimized for highest density of fabricated samples. Results of theses studies are presented and discussed in section 6.1.1 and individual parameters for printing of the various filaments were defined (Appendix B).

Even with nominal overfilling of layers, a certain porosity is left in printed samples as a result of the layered characteristic of FFF printing. To overcome this systematic porosity, the concept of post-compression in the green state was investigated. For a preliminary feasibility study, compression was generated using a cylinder hot mounting press (LaboPress 1, Struers, Copenhagen, Denmark). The pressure is applied uniaxially and vertically to the specimen. In order to generate the targeted quasi-isostatic compression, the dimensions of the cylinder samples were adjusted to exactly fit the diameter of the press. A systematic study of the compression effect was performed by varying the applied load between 20 kN to 45 kN, resp. 41 MPa to 92 MPa for the duration of either 5 min or 10 min. To improve flowing of the binder polymer and enhance densification, the sample was heated to a temperature of 180 °C during the compression process.

In the green state, further machining can be easily realized. A separate 5-axis CNC milling machine (Pocket NC V2-10, Bozeman, MT, USA) was used to cut the hourglass micro tensile specimens out of printed cylinder samples. The milling machine was equipped with a three-flute shank milling cutter of 2 mm diameter. The tool path was generated using CAD software (Autodesk Fusion 360, Autodesk Inc., CA, USA). Cylindrical specimens for compression and creep tests of the investigated superalloys were milled from printed green bodies in the same manner.

5.2.2 Debinding

The binder system enables two-stage debinding, which is divided into solvent debinding and thermal debinding. Equipment and materials used to realize both processes are briefly described below.

Solvent Debinding
The chemical extraction of the main binder component, i.e. TPE, can be realized by means of cyclohexane (≥ 99.5 %, Carl Roth GmbH+Co KG, Karlsruhe, Germany). To accelerate the solvent debinding process, elevated temperatures of 70 °C are used, which are below the boiling

point (80 °C) of the solvent [228]. The total time required to dissolve and extract the polymer is dependent on the sample thickness. Since the solvent attacks the surface of the component, debinding is a successive process that penetrates into the interior of the component with increasing immersion time. The actual degree of debinding can be checked by monitoring the weight fraction of the removed polymer. In this work, solvent debinding was considered complete as soon as 98.5 wt% of the total TPE content was removed.

Thermal Debinding
Thermal debinding is used to decompose and remove the remaining backbone polymer at elevated temperatures. The decomposition behavior of the specific polymer was analyzed by TGA in the range of 25 °C to 500 °C. Measurements were performed both in ambient atmosphere and low-oxygen atmosphere under nitrogen gas, to account for the influence of the atmosphere on the decomposition behavior. A variation of the heating rates from 1 °C min^{-1}, 3 °C min^{-1}, 5 °C min^{-1} to 10 °C min^{-1} allows a prediction of the debinding behavior. TGA measurements of the binder system were carried out at the Chair of Polymer Materials at FAU on a TGA Q5000 (TA Instruments, Eschborn, Germany). Data on partially debound IN 718 brown bodies and titanium brown bodies was provided from MUL.

Thermal debinding was carried out in different tube furnaces depending on the chosen atmosphere. The pO_2 was reduced either by an argon gas flow of 50 mL min^{-1} or by applying a vacuum in a Hereaus tube furnace (Heraeus Holding GmbH, Hanau, Germany), that was equipped with a Pfeiffer turbo-pump (Pfeiffer Vacuum Technology AG, Aßlar, Deutschland). In the latter case, levels varied between 1×10^{-3} mbar to 1×10^{-5} mbar, depending on the amount of the volatilized binder. Experiments under reducing atmosphere (95 % Ar with 5 % H_2) were performed with a constant gas flow rate of 250 mL min^{-1} (GSL-1500X-50HG, MTI Corporation, Richmond, CA, USA).

5.2.3 Sintering

Sintering was carried out at elevated temperatures up to 1400 °C in the furnaces used for thermal debinding. Again, vacuum, argon and forming gas were available as atmospheres. The sintering temperatures and times

were varied in this work to maximize the relative sintered density. In all cases, cooling was performed inside the furnace at a rate of 3 °C min^{-1}.

The achieved sintered density was evaluated according to Archimedes principle by weighing the sample mass in air and water (A200 S, Sartorius AG, Göttingen, Germany) and calculating the density according to equation 7:

$$\rho = \frac{m_{air} \cdot \rho_{water}}{m_{air} - m_{water}} \tag{7}$$

In addition, the residual porosity of cross-sections was determined by digital image processing using Image J software (version 1.45s, U.S. National Institutes of Health, MD, USA). Based on the results of the density measurement, an optimal sintering program was determined, which was used to produce samples for the characterization of microstructure and mechanical properties. Sintering temperatures and times were chosen individually for each processed material to create highest density while preventing excessive grain growth.

Pressureless sintering reaches maximum relative densities of 98 %. Further densification is only possible by application of external pressure as done in HIP. To evaluate the applicability of HIP for sintering and post-sintering treatments in the course of MF³ processing, some tests on modified Co-base superalloy 3 (CoWAlloy3mod) were conducted at Ruhr-Universität Bochum (RUB) using HIP QIH9 (Quintus Technologies AB, Sweden). A pressure of 100 MPa was applied at a temperature of 1250 °C for 30 min or in a two step process at 1100 °C for 120 min followed by 10 min or 60 min at 1250 °C. All HIP tests were completed by air quenching.

5.3 Chemical and microstructural characterization

Microscopy

The macroscopic structure of the samples, as well as the examination of porosity and defects, was carried out on a light microscope (Axio Imager M1, Carl Zeiss Microscopy GmbH, Jena, Germany). For this purpose, cross-sections perpendicular to the build-up direction during FFF were cut and prepared by wet grinding with SiC papers and polishing with

diamond suspensions and SiO_2 suspension. The *MosaicX Aquisition* mode was used for recording overview images which serve to evaluate systematic, process-related porosity.

Microstructural characterization was performed on a scanning electron microscope (SEM) (Zeiss Crossbeam 1540, Carl Zeiss Microscopy GmbH, Jena, Germany), mostly using backscattered electrons (BSE) at an acceleration voltage of 20 kV. Energy dispersive X-ray spectroscopy (EDX) on the same equipment was used for elemental phase analysis. For more detailed investigation of the microstructure of the processed superalloys, foils of 200 µm thickness were cut and electrolytically thinned (A3, Struers GmbH, Germany) to make them available for transmission electron tomography (TEM) characterization. A Philips CM200 transmission electron tomography was used at a high voltage of 200 kV. Electron backscattered diffraction (EBSD) images enable an evaluation of grain size and grain orientation. Measurements were done on a FEI Helios NanoLab 600i DualBeam (FEI Company, USA) with the EBSD-detector Symmetry (Oxford Instruments, UK) and analyzed using Tango software (Oxford Instruments, UK). Image acquisition was performed at an accelerating voltage of 20 kV and current of 2.7 nA with an exposure time of 3 ms and a step size of 1.5 µm. Inverse pole figure (IPF) coloring is used to visualize the grain orientation [229].

Chemical analysis
Various chemical analysis techniques and microscopic methods were used to characterize the microstructures, defects, phases and compositions after finalization of the MF³ sintering process. The content of oxygen and carbon in the bulk samples was determined by means of non-dispersive infrared technology (NDIR) (EMIA 320V2 and EMGA 620 WC, Horiba Jobin Yvon, Germany, respectively). For this purpose, samples of 0.035 g and 0.5 g were prepared by cutting and grinding. All NDIR analyses were performed at Neue Materialien Fürth (NMF).

Chemical analysis of the bulk samples by spark spectrometry was done with SpectroMaxx 06 (SPECTRO Analytical Instruments GmbH, Kleve, Germany) on polished cross-sections under argon flow.

Atom probe tomography (APT) (CAMECA LEAP 4000X HR, CAMECA Inc. Madison, WI, USA) was used for analysis of phase specific compositions. Sharp tips were prepared by either electropolishing or focused ion beam (FIB) (Zeiss Crossbeam 540, Carl Zeiss Microscopy GmbH, Jena, Germany) lift-outs of the regions of interest. Depending on the material,

voltage or laser mode was used for data acquirement: Titanium tips were measured in voltage pulse mode at a base temperature of 55 K and pulse fraction of 20 % at a pulse repetition rate of 200 kHz. Laser mode was applied for IN 718, using a pulse energy of 50 pJ and a pulse rate of 200 kHz to trigger field evaporation at 1 % of the pulses. The base temperature was set to 50 K. Data processing was done in IVAS (Cameca Inc. Madison, WI, USA) with the provided algorithm and MatLab (MathWorks Inc., Natick, MA, USA) using a custom algorithm developed in-house [230].

5.4 Mechanical characterization

Hardness tests
Vickers hardness of all processed materials was measured according to DIN EN 6507 with a load of 0.2 kp (1.96 N) (KWB 10-V, KB Prüftechnik GmbH, Hochdorf-Assenheim, Germany). The low indentation force allowed the insertion of several indents within a small specimen cross-section. For comparison of hardness, 10 indents were averaged in each case.

Bending tests
In case of the investigated ceramics, 3-point bending tests were carried out according to DIN EN 843-1, 2008 [231]. Specimens were printed with dimensions of 32×5×4 mm^3. To reduce the surface roughness caused by over-extrusion, the specimens were ground with 46 µm grit sandpaper in the green state. After sintering, no further surface finishing was applied. The final dimensions of the sintered bending specimens were 25×3.5×2 mm^3. The force was applied parallel to the build-up direction.

Tensile tests
Preliminary studies on the 316L steel demonstrated relevant ductility of the specimens despite the presence of residual porosity [232]. This allows an evaluation of the mechanical strength by tensile testing. Due to size limitations of the sintering furnace and resulting low specimen volume a micro tensile test set-up (Kammrath & Weiss GmbH, Dortmund, Germany) was used. The micro-tensile testing method and the clamping system developed therefor were first presented in [57]. The clamping system was constructed to ensure gimbal specimen fixation as illustrated in Figure 22a.

To prevent the small specimen from sliding in the clamping, a combination of tight and frictional fit was chosen. The frictional fit was achieved

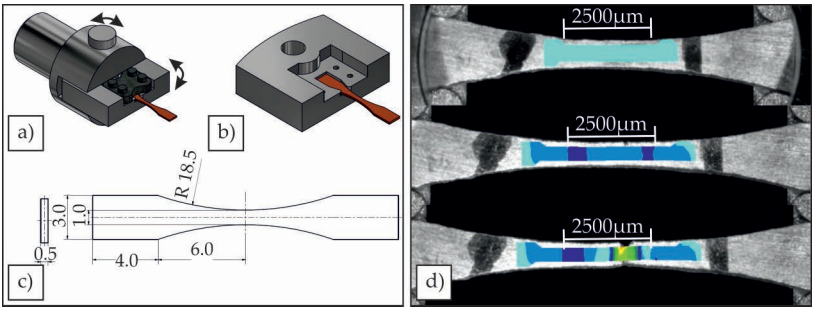

Figure 22: Micro-tensile test set-up with a) gimbal mounting of the micro tensile specimen with a rotatable bearing of the slide. b) Positive locking of specimens into the slide is created by sink erosion of a specimen shaped cavity. c) Dimensions of the hourglass specimen after sintering. d) Digital image correlation was used to measure the effective length according to regions of highest strain. Figures a-c) reprinted with permission [57].

by screw tightening using a roughened bracket (Figure 22a), whereas a positive locking was realized by sink erosion of a specimen shaped cavity into the sample holder (Figure 22b). The introduced cavities align the transversal symmetry axis of the specimen and the testing unit. Completed by rotatable bearing of the specimen holder using a connecting rod (Figure 22a), two-dimensional gimbal fixation of the samples is realized. Specimens have the hourglass geometry shown in Figure 22c [57]. The length of the specimens is 23.5 mm, with a gauge width of 1 mm at a thickness of 500 µm. These geometries were determined to create a stress increase in the gauge length of 200 % with respect to the specimen areas fixated in the clamping system. This approach limits the occurrence of yielding solely to regions that remain unaffected by fixation. The tensile module is equipped with a 5 kN load cell and an inductive displacement transducer. Tests were conducted displacement controlled at a constant rate of 5 µm s^{-1}. The tensile load was applied perpendicular to the build-direction. All tests were monitored in-situ by digital video microscopy (Keyence VHX-600, Keyance Corporation, Neu-Isenburg, Germany). This enabled verification of elongations by digital image correlation (Veddac 6.0.1.2, Chemnitzer Werkstoffmechanik GmbH, Chemnitz, Germany) according to regions of highest strain (Figure 22d).

Compression tests
Compression tests on the CoWAlloy3mod were performed on the universal testing machine Instron 4505 (Instron GmbH, 64293 Darmstadt) according to DIN 50106 [233]. Specimens of the forged reference material were eroded into cylinders with a diameter of 2.5 mm and ground to a parallel height of 4 mm. The MF³ samples were milled into cylinders in green state. An oversize of 40 % was selected, as after sintering oxide layers were removed from all surfaces by grinding and the final dimensions (diameter 2.5 mm, height 4 mm) were produced. All specimens were tested at room temperature (RT), 650 °C and 750 °C at a strain rate of $1 \times 10^{-4}\ s^{-1}$. The compressive load was applied parallel to the build-direction.

Creep tests
Mechanical performance of IN 718 at high temperatures was investigated by creep tests on a custom-build pneumatic device. Creep specimens were milled out of printed cylinders in green state and had a cylindrical shape with a diameter of 4 mm and a length of 6 mm after sintering. Tests were performed on annealed samples at 650 °C under compression from 650 MPa to 800 MPa. In all measurements the load was applied parallel to the build-direction.

6 Process development of MF³

The results of the experimental studies carried out in the scope of this work are presented in the following chapter. At the beginning, the general process is treated independently of the investigated material, including a parameter optimization for the individual process steps. These imply the adjustment of the printing parameters for the production of densely filled green bodies (section 6.1). In section 6.2, the debinding process for the selected binder system is covered, taking into account the individual steps for removing the polymer and initiating sintering processes. The process optimization is concluded by a general consideration of the sintering process for the densification of the manufactured samples in section 6.3. In the second part of the chapter, the processability of different inorganic and metallic materials by MF³ is investigated and the particularities resulting from the individual material properties are specified (section 6.4). Finally, section 6.5 provides an outlook on the potential of the presented process for the manufacturing of multi-material compounds and complex components.

6.1 Shaping of green bodies for metal fused filament fabrication

The shaping of green bodies was realized by a filament extrusion process. Afterwards, further manufacturing operations were applied for compensation of printing induced irregularities. For this purpose a compression process was added to remove minor printing defects and increase the density of the printed components. Additionally, milling was performed on some samples in the green state to cut out the geometry of specimens for tensile or creep testing.

6.1.1 Material extrusion

The highly filled filaments developed at MUL can be processed with conventional desktop FFF printers. Modifications to the equipment used in this work, which take into account the abrasive effect of the powders integrated in the filaments, have already been described in chapter 5.2.1. The majority of the processed filaments were printed with a 0.6 mm diameter nozzle. This was determined after a series of preliminary tests

and corresponds to the smallest possible diameter that allows stable extrusion without clogging of the nozzle. For the processed Al_2O_3 it was necessary to increase the diameter of the nozzle to 0.8 mm due to the irregular particle shape of the powders, that leads to a higher filament viscosity. The nozzle temperature during printing of the highly loaded MF³ filaments must be high enough to sufficiently reduce the viscosity and prevent clogging of the nozzle. At the same time, there is an upper limit for the maximum nozzle temperature if the viscosity is too low during extrusion. In this case, the deposited filament strands are too weak, so that no sharply defined geometry can be built up.

A detailed evaluation of the influence of nozzle temperature on print quality of the Ampersint 1557.02 tool steel shows the susceptibility to print defects if the temperature is too low [234]. For a temperature of 270 °C, significant printing defects are visible in Figure 23a, which cannot be completely compensated even by a higher extrusion multiplier (Figure 23b).

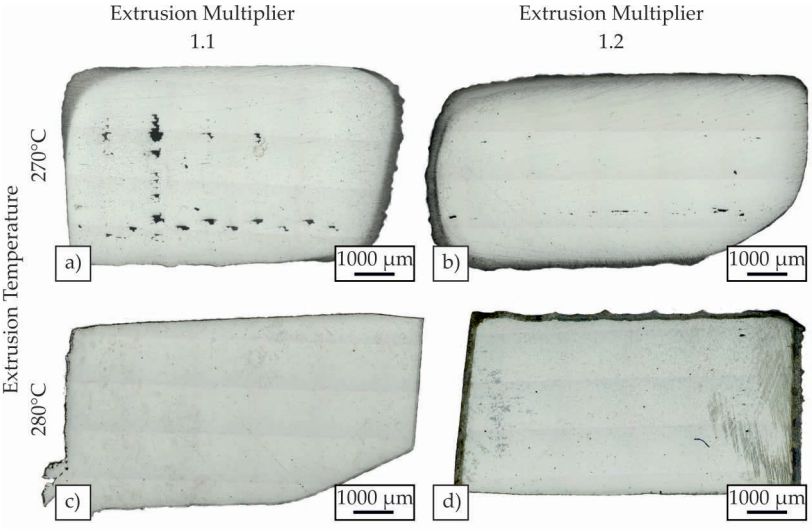

Figure 23: Influence of the printing temperature and extrusion multiplier on printing defects visible as sytematic pores after sintering.

In comparison, Figures 23c & d demonstrate how a temperature increase of 10 °C contributes to a significant increase in print quality and reduction

of printing induced irregularities. The higher temperature improves the diffusion between deposited filament strands and creates a stronger fusion of the layers and reduction of intermediate defects [112].

For all filaments used in this work, the optimum printing temperature lies between 250 °C to 290 °C. This value is higher than the printing temperatures of pure polymer filaments because the high particle content significantly increases viscosity. On the other hand, incorporation of particles with high thermal conductivity increases the thermal conductivity of the filament [235], which promotes melting of the filament and ultimately lowers the viscosity [236]. This effect is particularly evident when printing the copper filament, which can be extruded at the lowest printing temperature of the metal-loaded filaments studied, at 250 °C.

Unlike reported for pure thermoplastic FFF filaments [237], the temperature of the print bed did not prove to be decisive for good bonding of the first print layer. Since the glass transition temperature (Tg) of the main binder component, i.e. the TPE, is below room temperature, the polymer exhibits rubber-elastic behavior after extrusion even when in contact with the unheated print bed. Nevertheless, Spoerk et al. proved a jump in viscosity of PP-based filaments between 70 °C to 120 °C and therefore better adhesion when heating the bed to this temperature range [238]. Although PP is the backbone polymer of the filaments used in this work, print bed temperatures of 20 °C, 70 °C and 100 °C were successfully used. Besides improving the first layer adhesion, heating of the print bed can also contribute to avoid abrupt cooling and potential formation of thermal stresses inside the printed structure and thus prevents cracking and warpage of the printed samples. At this point, the increased thermal conductivity of the MF³ filaments due to the high particle content further contributes to a more uniform heat distribution inside the deposited part, reducing distortion during printing [235]. On the other hand, a temperature of 100 °C constitutes the maximum output of most FFF printers and thus results in high wear. For an extension of the printer lifetime, the high print bed temperature can therefore be dispensed with, since it has no influence on the quality of the final MF³ components.

The printing speed was experimentally defined to reduce total printing durations while ensuring best layer bonding. For good adhesion of circular or curved circumspheres, the printing speed was reduced to $25\,\mathrm{mm\,s^{-1}}$. Execution of the rectilinear infill was accelerated, using a

speed of 30 mm s^{-1}. Adapted to the printing speed and nozzle temperature, the speed of the fan, used for accelerated cooling of deposited layers, also decisively influences the print quality. Since heat capacities of the integrated metal powders are significantly higher than those of pure polymeric filaments, the printing time of a single layer is not long enough to generate sufficient cooling. Printing trials, as shown in Figure 24 using an open box shape with 5 mm wall thickness allowed investigations on an intentionally difficult model in terms of cooling airflow.

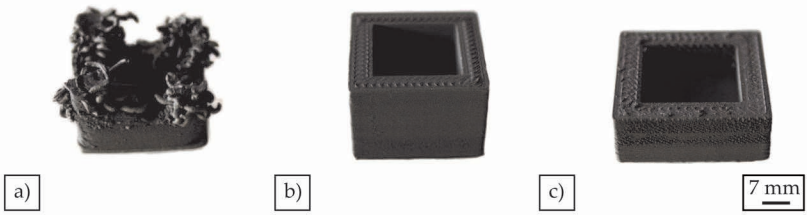

Figure 24: Influence of the fan settings on the success of the printing process: a) Insufficient layer cooling without fan: Imperfect layer bonding and shape loss. b) Optimized layer cooling with stepweise increased fan speed by 2 % every second layer up to a maximum of 25 %. c) Excessive cooling with fan at full power: bonding deficits and interruption of printing process. Reprinted with permission [232].

Without additional fan cooling, insufficient cooling of the printed layers resulted in unbound, curly structures, that finally impeded printing of further layers (Figure 24a). Contrastingly, too high of a fan speed led to rough surfaces and even caused clogging of the nozzle with abortion of the printing process, as shown in Figure 24c. For the examined model, best results were obtained by gradually increasing the fan speed by 2 % every second layer until reaching a fan speed of 25 % of the maximum speed of 6500 rpm of a 225 L min^{-1} to 400 L min^{-1} radial fan. Combining the nozzle temperature of 290 °C with the stepwise fan control enabled successful printing of the chosen box with a smooth print quality that is depicted in Figure 24b. In general, the adaptation of the fan power to the material, component shape and printing speed is essential for a successful printing process.

In terms of the infill strategy, the layer-by-layer filament fabrication includes printing two circumferential lines that build up the outer wall of the component. This is supplemented by a systematic infill, which is

independent of the shape of the cross-sectional area. While with conventional FFF of polymers the components are often filled using grid structures with a relative proportion of 25 % to 50 %, a complete filling is targeted in this work for additive manufacturing of solid metallic components. This was realized by a 100 % linear filling with a relative overlap of adjacent printed lines of 20 %. In case of inadequate printing parameters, defects occurred with this filling pattern both in the specimen interior and at the transition from the infill to the circular border. Micrographs of sintered samples still show these defects even after completion of the entire process chain of the MF³ (Figure 23). The pores generated during the printing process are too large and cannot be eliminated by densification during the sintering process. To avoid these systematic defects, the filling pattern of the cylinder samples was adapted and a combination of alternating linear and concentric patterns was used as can be seen in Figure 26. On top, a deliberate over-extrusion during the printing process also contributes to higher green part density. An increase of the extrusion multiplier from 1.0 to 1.1 results in a significant reduction in visible printing defects and, after sintering, an increase in relative density from 80 % to 88 %. Further increments generate further increases in density, albeit to a smaller extent. A nominal extrusion rate of 120 % was selected as the best option by setting the value of the extruder flow rate to 1.2. The dimensional accuracy of the green body is not affected by this measure, while the systematic porosity is reduced.

Reducing the layer height additionally proved beneficial in increasing the density of MF³ components. By repeatedly applying thinner layers of material in combination with the slight over-extrusion within the individual print layers, higher packing can be achieved when using smaller layer height. Additionally, the more frequent deposition of hot filament increases the diffusion between adjacent strands and contributes to enhanced layer adhesion inside the green body [112]. In systematic investigations on cube-shaped 316L samples, the reduction in the layer thickness from 0.3 mm to 0.1 mm contributed to an increase in the relative sintered density from 90 % to 95 %.

Drawn from these presented results, the optimum printing parameters for each material are listed in separate tables in appendix B. In general, a layer height of 0.1, an extrusion multiplier of 1.2 and an alternating linear and concentric infill pattern are best suited to produce green bodies with high volume filling and a low proportion of systematic printing defects.

6.1.2 Compression of printed green bodies

Green bodies printed with optimized parameters can still contain minor bonding deficits and a locally lower packing density. To compensate for these inaccuracies, a compression step in green body state is conceivable, generating further densification of printed samples. Processes described in literature, such as gas isostatic forging or cold isostatic pressing [239, 240], require complex equipment that was not available in the scope of this work. As a feasibility study, a hot press was used to generate quasi-isostatic compression of the cylindrical shaped samples. The increase in relative density produced by the compressive force exerted at a temperature of 180 °C was examined, varying the amount of force and the duration of its application. Results of compression tests on 6 mm high green bodies are provided in Table 2. The evaluation of best compression parameters was conducted on titanium samples and results of this study are published in [57].

Table 2: Experimental study of the increase in relative density generated by compression in green state. The increase in relative density in dependence of the applied pressure and duration of compression is calculated relative to the maximum obtained green density of 3.06 g cm^{-3}.

Duration	Pressure		
	41 MPa	62 MPa	82 MPa
5 min	+ 0.1 %	+ 3.7 %	+ 1.6 %
10 min	+ 3.0 %	+ 6.0 %	+ 7.0 %

Experimental investigations show a general trend of a higher increase in density when increasing the applied force. A duration of 10 min is favorable to give enough time for material flow and thus enhance compression. Complementary to this systematic series of tests, the application of a higher pressure of 92 MPa for a duration of 10 min was tested on green bodies of 4 mm and 6 mm height. Again, the compression successfully increased the density in these tests independent of sample height. Variations in the green density which reduce process stability were significantly reduced by the compression step. The measurable increase in the green density also affects the final density, creating an increase in density of 1 % to 2 % after sintering (Figure 25a).

The reduction in porosity of titanium samples in the final sintered state is clearly visible in light microscopy images in Figure 25b.

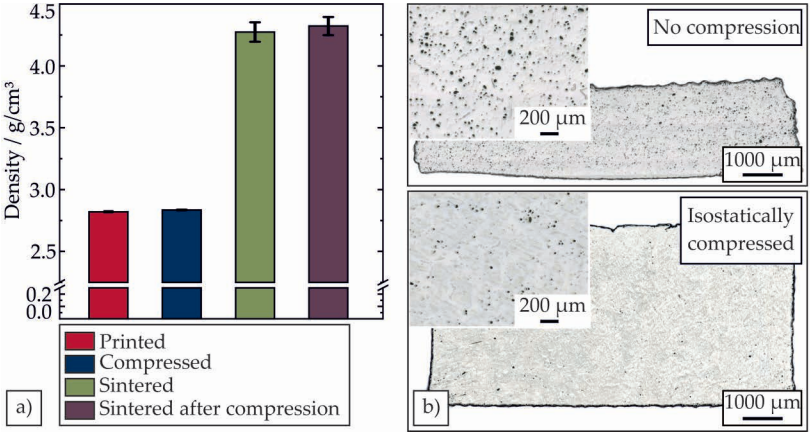

Figure 25: Impact of green body compression demonstrated a) on the density of green body and sintered titanium part and b) on resulting porosity in microscopical cross-sections of sintered samples. Adapted with permission [57].

The performed compression is an evidence of the possible enhancement of particle packing within the green body. Therefore, the pressing in green state was used for most samples investigated in this work in order to obtain best reproducibility, homogeneity, and with simple means to increase the final density. Similar compression could be realized by other methods using a liquid or gas. The concept of compression of green bodies can in these cases be used for form-free production, if the force is applied isostatically. For example, as shown by Paramore et al., gas isotatic forging allows reduction of existing defects without limiting the dimensional freedom gained by the printing process [241].

6.1.3 Milling in green body state

Due to the large volumetric proportion of binder, MF³ green bodies can be machined with simple means and inexpensive tools. In the scope of this work, a milling process was chosen to cut the specimens required for mechanical testing out of printed cylindrical green bodies. Using a standard 5-axis CNC milling machine, no additional modifications are necessary to machine the green bodies with high accuracy.

All hourglass micro tensile and cylindrical creep specimens shown in later chapters were shaped by milling out of printed cylinders.

The entire process chain of the green body production as applied in this work is shown in Figure 26. It includes manufacturing of cylinder samples by filament extrusion that is in some cases followed by compression of the green body for reduction of minor printing defects. Milling as the last shaping step is optional, if specific geometries are required for mechanical tests.

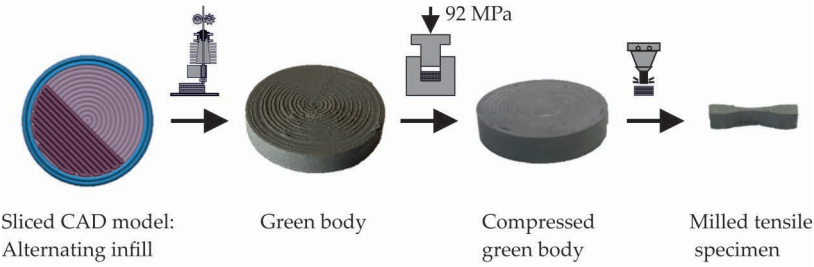

Figure 26: The process chain for green body fabrication as applied in this work comprises fused filament fabrication and optionally compression and milling.

This process chain for fabrication of 3-dimensional green bodys could alternatively also be implemented using the milling function of a multi-axis machine used previously for printing, as suggested by Parenti et al. [114].

The green parts produced according to this process chain are densely filled and have no systematic defects caused by the shaping process. After printing, parts exhibit characteristic wall structures that emerge from building up in layers during the FFF. The staircase surface appearance is reduced by the compression step. If further surface smoothing is requested, milling can also be applied without altering the general part geometry [114]. Alternatively, laser polishing is another method that was demonstrated to contribute to the reduction of green body roughness [11].

6.2 Removal of organic binder constituents

The aim of the debinding step is the complete decomposition and removal of organic components without altering the chemical composition of the

remaining powder. The multi-component binder system developed at MUL is suitable for a two-stage debinding process, consisting of solvent debinding and thermal debinding [94]. Hereby, the preliminary solvent extraction of a main binder amount enables the reduction of the overall process duration.

In the scope of this work a debinding workflow was established, that reliably enables removal of the organic binder constituents. The two steps of solvent and thermal debinding were studied individually, and in each case the successful removal of the targeted binder component was verified. The resulting microstructure evolution was monitored throughout the process. After completion of the entire debinding step, the chemical purity of the remaining metal part is analyzed. Some of the following results have previously been published in [232] and [57].

6.2.1 Solvent debinding

The main binder component (TPE) is solube in cyclohexane. The mass fraction that needs to be chemically extracted is known for each material from calculations of the filament composition. The degree of solvent debinding and thus also its completeness can be determined from the mass loss of the samples. It is known from previous investigations that more than 95 % of the contained TPE must be removed to enable a defect-free thermal debinding afterwards [94]. Measurements on 316L green bodies conducted in preliminary studies show the expected dependency of the total duration of solvent removal on the wall thickness (in the specific case the thickness of the cylinder sample) [232].

The recording of the extracted polymer fraction that is pictured in Figure 27 was carried out using 250 mL of fresh cyclohexan per 100 g sample mass. No recirculation was used, which resulted in saturation of the solvent during extraction. The measurements indicate a completion of the solvent debinding step after 28 h for a wall thickness of 2 mm. In comparison, 56 h of immersion time are required in case of a wall thickness of 6 mm. In the context of this work, a closed solvent debinding set-up without solvent recovery was used. This led to a saturation of the solvent with ongoing debinding, resulting in a reduction of the extraction rates during the debinding process. As a consequence longer process times were required for thorough removal of the soluble binder

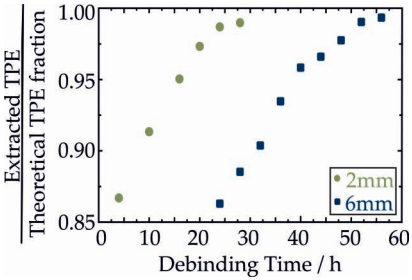

Figure 27: Dependence of the duration of the solvent debinding on the wall thickness of the green body. Measurements were recorded each with 250 mL fresh cyclohexan per 100 g sample mass. Reprinted with permission [232].

polymer. For the practical implementation of this work, the immersion time was adapted to create the necessary mass loss. Incompletely debound samples were reintroduced into the solvent until at least 98 wt% of the theoretically contained TPE were removed. Slight deviations in the amount of the extracted mass fraction resulted if small proportions of the soluble polymer were completely enclosed by the insoluble backbone polymer. Additionally, even small variations in the concentration within the filament can result in deviations of the mass loss achieved during solvent debinding. According to the recorded mass losses, every material investigated within this work was successfully solvent debound.

The removal of TPE during the solvent debinding step is also visible on microstructural level and can be verified using SEM imaging. A comparison of the microstructure before (Figure 28a) and after (Figure 28b) solvent debinding shows the generated porosity. The extracted binder component leaves pore channels that traverse the entire sample evenly and, once the solvent debinding is completed, can be observed at any fracture surface. These interconnected pores serve as pathways for the removal of the decomposition products during the subsequent thermal debinding [97]. Figure 28b shows how the embedded powder particles remain completely encapsulated in the organic network of the backbone polymer at the end of the solvent debinding step. This guarantees the dimensional stability of the partially debound green body [115]. Based on this microscopical analysis, solvent debinding can be considered successfully completed in terms of removal of the contained TPE and preparation for subsequent thermal debinding.

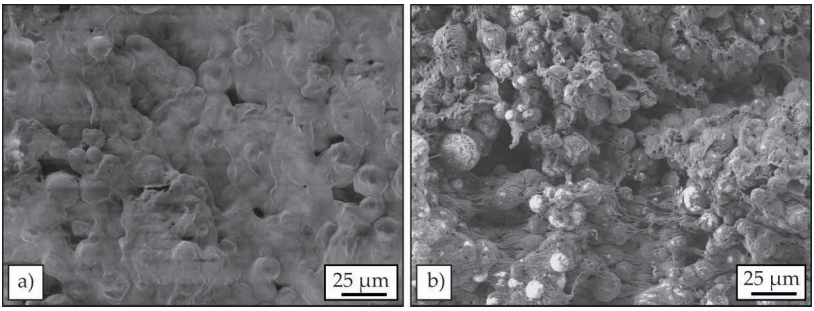

Figure 28: Development of the microstructure with ongoing solvent debinding: a) As-printed state prior to debinding: Surface microstructure of printed green bodies. b) Condition after completion of solvent debinding: Microstructure of a fractured surface with interconnected pore network after completion of solvent debinding. Reprinted with permission [232].

The successful solvent extraction of the main polymer fraction while maintaining the strength of the partially debound part proves that the filament preparation was successful in terms of building a homogeneous feedstock network structure during compounding. The results are evidence that a suitable feedstock formulation has been found for separating polymer removal into solvent extraction and thermal debinding steps.

6.2.2 Thermal debinding

Thermal debinding comprises decomposition of the remaining binder polymer at elevated temperatures and removal of decomposition products through the previously formed pore channels. To avoid the formation of defects, a balance between these two processes must be established, with the removal of decomposition products through the interconnecting pore channels being the rate-determining step of thermal debinding [69]. In practice, this means that the decomposition of the polymer must be controlled by adjusting the heating rate. This process is highly dependent on the specific binder polymers and their corresponding degradation behavior. Since the same binder system is used for all filaments in this work, the thermal debinding parameters are identical for all investigated materials. The degradation behavior of the backbone polymer used in this work was studied by TGA that records the rate of decomposition of the backbone polymer as a function of temperature. By identifying

the temperature range of polymer decomposition, this measurement provides a guideline for creating an adapted temperature program.

The data plotted in Figure 29 for the decomposition of the backbone polymer show a dependency of the decomposition temperature range on the heating rate. Slower heating rates give more time for the onset of decomposition processes and decrease the critical temperature range. The surrounding atmosphere has a stronger influence on the decomposition behaviour than the heating rate. The TGA measured in nitrogen shows an increase in the decomposition temperature of around 150 °C for the backbone polymer used in this work. These results demonstrate that oxygen accelerates the decomposition of polymer chains and consequently debinding in an atmosphere of low pO_2 leads to a strong delay of the reaction. In any atmosphere, the binder used in this work is completely decomposed up to a temperature of 450 °C.

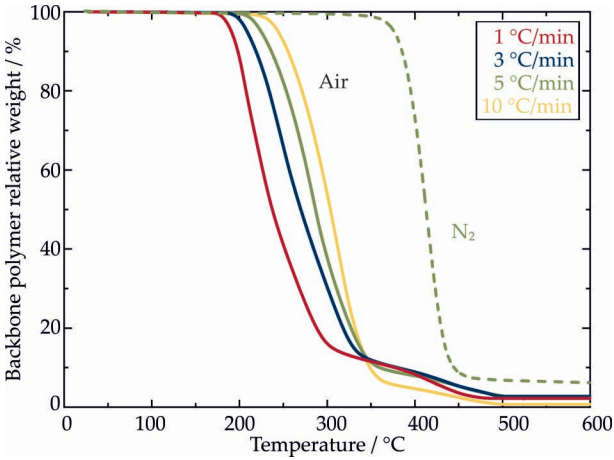

Figure 29: TGA of the pure backbone polymer measured in air and low pO_2 (N_2) atmosphere. A strong dependence of the range of highest decomposition rate on the heating rate and the pO_2 inside the atmosphere can be observed.

The maximum heating rates applicable for defect free debinding of the printed cylinders fabricated in the scope of this work were experimentally evaluated by test series on 316L stainless steel samples. Results of these investigations have already been published in [232]. To preserve high sintering activity, only low pO_2 atmospheres were considered, i.e., vacuum,

Ar and Ar+5 % H_2. The effect of different heating rates on the dimensional stability and defect formation of 6 mm thick cylinder samples during thermal debinding in vacuum is shown in Figure 30. Particularly the sample that was debound at the highest heating rate of 3.0 °C min^{-1} shows serious distortion and shape loss in the bottom part. At a heating rate of 1.0 °C min^{-1} the dimensional stability was conserved. Yet, there was an increase in pressure inside the sample, which led to the formation of bubbles on the surface.

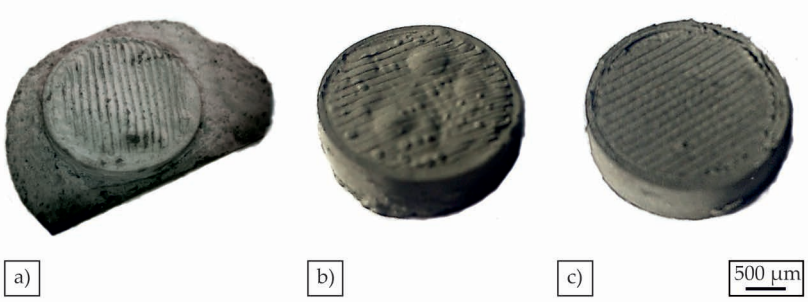

Figure 30: Influence of heating rates during thermal debinding of 316L parts of 6 mm height in vacuum: a) 3.0 °C min^{-1}: shape loss due to too fast binder degradation, b) 1.0 °C min^{-1}: bubble formation on the surface as a result of internal pressure increase, c) 0.2 °C min^{-1}: defect-free debinding by balanced binder degradation and evaporation. Reprinted with permission [232].

For reproducible, defect-free debinding in vacuum, the heating rate of the examined samples was reduced to 0.2 °C min^{-1}. Since this slow heating rate would result in very long measurement times, no TGA was recorded at this heating rate. However, in Figure 31 the decomposition curve at 0.2 °C min^{-1} in N_2 atmosphere was calculated on the basis of the measured values shown in Figure 29. The value of 0.2 °C min^{-1} applies to the examined wall thickness of 6 mm that lies at the top end of the realizable dimensions. Similar results were obtained for 5 mm wall thickness with a rate of 0.5 °C min^{-1} by Supriadi et al. [122] and for 4 mm thickness with 1.0 °C min^{-1} by Li et al. [242]. More detailed investigations, which also take into account the influence of the filament infill percentage on the realizable heating rate, were carried out on the Ampersint 1557.02. For cylinders of 6 mm height with powder fractions of 55 vol% and above, a rate of 0.4 °C min^{-1} can be applied in vacuum without causing defect formation. If the infill level is only 50 vol%, a maximum heating rate of

0.2 °C min⁻¹ must be used to avoid distortion. In general, a reduction in heating rate contributes to an increase in sintered density, but once defect formation is prevented, further density gain is negligible. Lowering the rate further to 0.1 °C min⁻¹ can be beneficial at 60 vol% powder content, but there is no clear trend [234].

To verify the binder removal under practical conditions at 0.2 °C min⁻¹ in vacuum, the expected behavior for the reduced heating rate was calculated based on the measurement at 5 °C min⁻¹ in N_2. The actual degradation behavior of the backbone polymer in the used vaccum furnace was evaluated by interrupted thermal debinding tests. Samples were heated to the indicated temperature with 0.2 °C min⁻¹ and directly afterwards cooled at 5 °C min⁻¹. The remaining weight percentage of backbone polymer after heating to the respective temperature is indicated by the blue squares in Figure 31. The recorded polymer removal according to the measured values of remaining sample weight correlates very well with the calculated data obtained from TGA measurements.

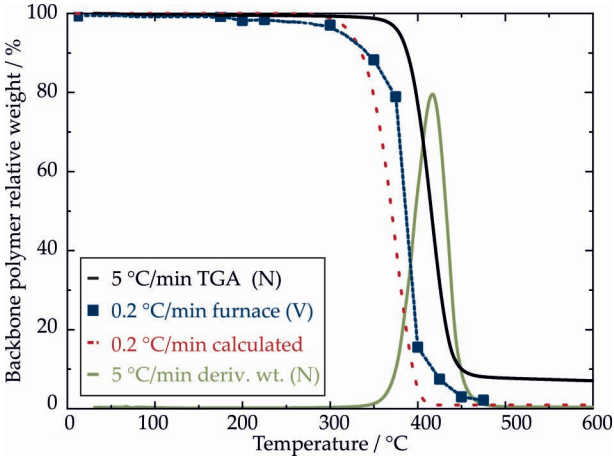

Figure 31: Degradation of the backbone polymer measured in controlled N_2 atmosphere at 5 °C min⁻¹, calculated for a heating rate of 0.2 °C min⁻¹ (red dotted line) and measured by interrupted thermal debinding at 0.2 °C min⁻¹ in a vacuum furnace (blue squares). The green line gives the weight derivative curve measured at 5 °C min⁻¹ in N_2. Reprinted with permission [57].

As the TGA indicates the completion of the decomposition process at 450 °C to 500 °C, low heating rates result in long process times of up to

48 h. To speed up the debinding, a step-wise temperature program can be used where the heating rate is massively reduced only in the critical temperature range of the highest decomposition rate [243]. In the scope of this work, a step-wise temperature program was established based on the experimental analysis of several critical heating rates in different atmospheres in combination with the measured TGA data. This program enables defect-free thermal debinding in the shortest possible process duration. It includes the use of the minimum heating rate between 170 °C to 450 °C in each of the furnace atmospheres. The temperature curve for thermal debinding in vacuum is plotted in Figure 32. It consists of three ranges with an initial rapid heating at 10 °C min^{-1} to 170 °C, as the binder polymer is not affected and does not undergo degradation in this temperature range. During the critical second phase, slow heating at 0.2 °C min^{-1} is applied between 170 °C to 450 °C. The polymer removal is concluded by a soaking time of 60 min at 450 °C to give enough time for complete binder degradation and evaporation. Finally, heating to the targeted sintering temperature can be conducted at 5 °C min^{-1}. This step-wise temperature program reduces the total duration of thermal debinding to 25 h, which is half the time required for constant heating at 0.2 °C min^{-1}.

Depending on the used binder system with different polymers, similar temperature programs were derived by Derfuss et al. [123]and Pinwill, Edirisinghe, and Bevis [244], albeit with more steps and consequently smaller increments of temperature ranges. Another strategy for implementation of a rate-controlled binder removal is the use of a microbalance to record the weight loss over time and control the furnace power. This in-situ thermogravimetric analyzer produces very small variations in heating rate over the entire temperature range, resulting in a multi-step temperature program [63, 124].

Microstructure images serve to check the removal of the organic components by the stepwise temperature program. Exemplary, titanium was investigated by interrupted debinding tests with a critical heating rate of 0.2 °C min^{-1} in vacuum. Samples were slowly heated to the indicated temperature and immediately afterwards a cooling process with a cooling rate of 5.0 °C min^{-1} was initiated. Results of these investigations have previously been published in [57]. The SEM images of titanium samples after interrupted thermal debinding (Figure 32) allow an observation of the binder removal as a function of the debinding temperature. At the beginning of thermal debinding, the green body is permeated

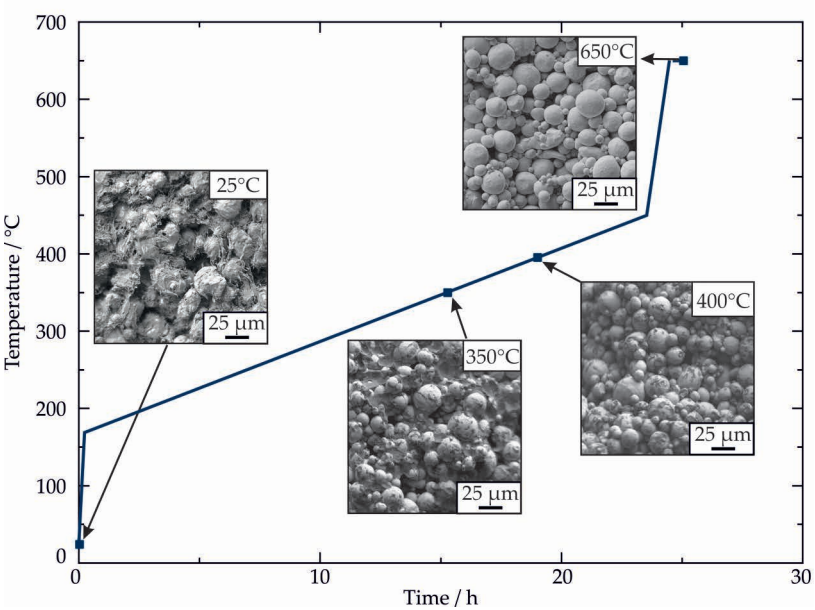

Figure 32: Stepwise temperature profile for thermal debinding in vacuum. Microstructural images show the evolution of titanium microstructure during thermal debinding.

by interconnecting pore channels formed during the preliminary solvent debinding process. The remaining backbone polymer constitutes a fibrous network that still completely encapsulates the titanium particles. The first microstructural changes become visible at a temperature of 350 °C, at which the organic content is significantly reduced. The strength of the samples is greatly reduced in this state, as the fraction of polymer retaining the particles in shape decreases substantially and the porosity increases. This development progresses up to 400 °C where almost the entire polymer is removed, until at elevated temperatures of 650 °C microstructural images confirm the complete decomposition of the organic binder components.

Detailed analysis of heating rates in different temperature ranges provides a stepwise temperature program, which is used in this work for defect-free thermal debinding of investigated samples. The heating rate that is applicable in the critical temperature range between 170 °C to 450 °C

depends on the used atmosphere. Comparative debinding experiments with constant heating rates in Ar and Ar/H_2 (95 %/5 %) atmosphere show strong differences in the maximum applicable mass loss rate. In vacuum, as already described, a maximum heating rate of 0.2 °C min^{-1}, corresponding to a mass loss rate of 0.023 mg min^{-1}, can be used. In contrast, heating rates up to 0.5 °C min^{-1}, i.e. 0.057 mg min^{-1} are achievable with gas flow. The pressure of the surrounding gas atmosphere contributes to better tolerance of a higher internal pressure in the sample. In addition, the gas flow accelerates the removal of decomposition products [245], which prevents the formation of high pressure levels inside the component. The process times for thermal debinding can therefore be significantly reduced by using a gas atmosphere of low pO_2 compared to debinding in vacuum.

In order to maintain the chemical purity of the MF³ components, the carbon content after thermal debinding should be at the same level as in the starting powder. Binder residues due to incomplete evaporation, however, lead to an increase in the carbon content. NDIR measurements on sintered titanium samples, each thermally debound according to the optimum temperature program in argon (critical heating rate 0.5 °C min^{-1}) and vacuum (critical heating rate 0.2 °C min^{-1}), show a significant increase in C-level as a result of the MF³ process. In a direct comparison of the two atmospheres, more effective removal of the outgassing carbon compounds was achieved with argon flow. The measured C-content within the bulk material is 0.12±0.02 wt% when debinding in argon compared to 0.89±0.03 wt% after vacuum debinding. These measured values are consistent with investigations on MIM titanium alloys [128]. The same trend is also evident for tool steels with significantly lower C-levels after debinding in argon atmosphere compared to vacuum debinding. However, while processing of titanium targets at lowest C-contents, carbon is an important alloying element in steels and is necessary for achieving the desired microstructure and hardness [164]. When fabricating steels, it must therefore be ensured that C-levels do not become too low due to the processing history.

Apart from carbon control, the oxygen uptake during MF³ processing must be limited in order to prevent harmful oxide formation. However, titanium samples processed in argon exhibit a significantly increased oxygen content (1.52±0.18 wt%), which is particularly noticeable through the formation of oxide layers on the component surface. Vacuum processing is beneficial in this case as it limits oxygen uptake resulting in lower

contents of 0.56±0.01 wt%. The same correlation between debinding atmosphere and resulting oxygen content was observed by Shibo et al. on MIM titanium alloys [128].

Analyses of the titanium samples show that with respect to chemical purity the choice of debinding atmosphere must be made specifically for each material and must take into account properties such as oxygen affinity and targeted carbon content. Further details on atmospheric influences on properties of sintered MF³ metals are also given in section 6.4.

The mechanical strength and the underlying development of the microstructure after completion of thermal debinding was investigated by a series of pre-sintering tests at different temperatures. To create first pre-sintering activities, samples were subjected to a hold-time at 650 °C, 700 °C, 750 °C, 800 °C and 850 °C for 90 min each directly after the heating program of the thermal debinding. When pre-sintering titanium and 316L at 700 °C or below, the samples did not exhibit sufficient mechanical strength and stable handling of the samples was only possible at 750 °C and above. Figure 33 shows the two complementary processes that contribute to the enhancement of stability of the powder bodies: the strength in the pre-sintered state arises either from increased interparticle friction or via material bridges as a result of initial sintering neck formation.

Before this condition is reached, the strength of the powder packaging in the course of the debinding process is generated by attractive forces of the remaining binder. Fig. 13 illustrates the interactions between binder components and powder particles as the debinding process progresses. The microstructure changes from the funicular stage after solvent debinding to the pendular state shortly before debinding is completed. Liquid binder components at point contacts between neighboring powder particles exert attractive forces between the particles. These forces initiate particle rearrangements and consequently lead to a denser packing of the particles. The result of these rearrangement processes becomes particularly clear when comparing the microstructures of 316L parts pre-sintered at 700 °C (Figure 33a) and 750 °C (Figure 33b). After complete removal of the organic components, the cohesion of the powder packing is maintained by Van der Waals forces between neighboring particles. These weak interactions are reinforced by friction of the particle surfaces, so that good stability is obtained when the packing is dense. Additionally,

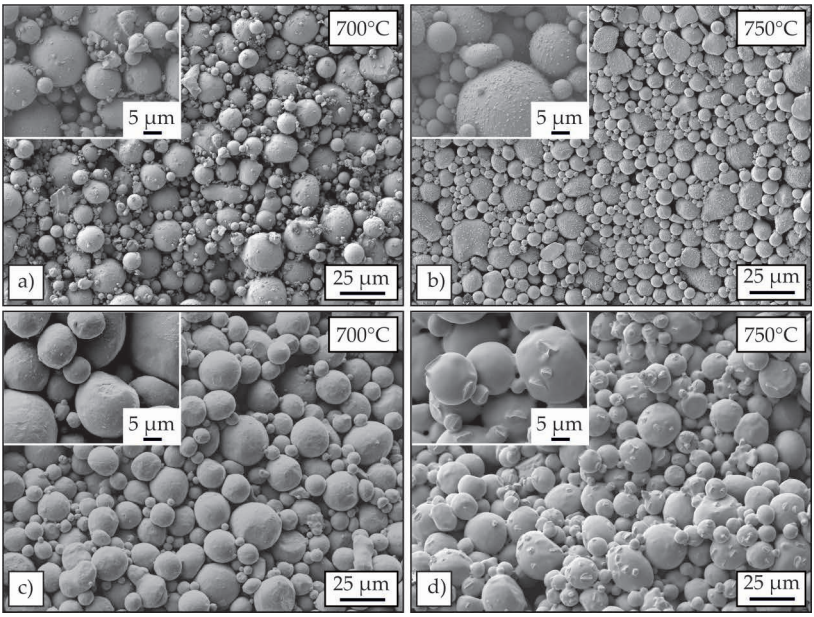

Figure 33: Developement of the microstructure of 316L (a and b) and titanium (c and d) as a function of the pre-sintering temperature after thermal debinding. a) and c): loosely packed particles after a dwell time of 90 min at 700 °C b): densely packed particles after 90 min at 750 °C indicate strong rearrangements of 316L particles, d): first formation of sintering necks between titanium particles after 90 min at 750 °C.

friction is increased by oxide formation on the particle surface, which in case of the 316L takes place from 750 °C onwards despite the vacuum atmosphere used. Oxides increase the roughness of the surface and thus the friction. Nevertheless, efforts should be made to avoid oxide formation, since the oxides formed on particle surfaces inhibit sintering later in the process.

The second mechanism that increases the stability of the samples is the formation of sintering necks, which can be detected in titanium at 750 °C (Figure 33d). With the onset of oxide reduction, which starts at 700 °C for titanium powder [167], the sintering activity is strongly increased and first bonds are formed between neighboring powder particles. As

sintering progresses, these bonds become stronger and the stability of the parts increases.

The steels, cp-Ti and IN 718 investigated in this work exhibit sufficient mechanical strength to allow for part handling when pre-sintered at 750 °C. Only the copper requires pre-sintering at higher temperatures of 900 °C to develop similar strength.

6.3 Sintering

The completely debound brown body in the pre-sintered state is highly porous. The removal of the original 45 vol% organic content in the green body creates a continuous pore network. After particle rearrangements and initial densification processes at the elevated temperatures during the thermal debinding process, the density of the brown bodies lies between 70 % to 85 %. To remove the correspondingly large amount of remaining pores, a high degree of shrinkage must be generated during the final sintering process, which produces pronounced shrinkage in each spatial direction. Dilatometry on pre-sintered samples shows a linear length shrinkage of 12.3±1.6 % that, in combination with the preliminary shrinkage during thermal debinding (7.1±1.2 %), results in a total shrinkage of approximately 20 %. This is within the expected range of linear shrinkage for an original packing density of 55 vol% in the green body (Figure 17a) [74].

A pronounced anisotropy of the shrinkage is to be expected due to the layered character of the printed samples [143]. Kurose et al. reports significantly higher linear shrinkage in the z-direction than in the xy-directions [143]. As described in section 3.4, they assign the higher shrinkage in printed z-direction to the layered character of FFF green bodies. They state that the packing density of particles between adjacent layers is slightly lower than within a single layer, resulting in a higher degree of shrinkage upon densification (Figure 17b). In this work, the linear shrinkage was determined for samples printed with optimized parameters and the influence of layer height and green body compression was evaluated. To exclude influences of differing wall thicknesses, 316L cubes of 10×10 mm were milled out of printed cylinders for systematic investigations. Cubes that did not undergo compression in the green body state show a dependence of the anisotropy on the layer height. Results in agreement with those reported by Kurose et al. with higher

shrinkage in the z-direction are observed only for the largest layer height of 0.3 mm. However, the difference to the lateral xy-shrinkage is not pronounced. In actual figures, this equates to a shrinkage of 17.3±0.6 % in lateral xy-direction that compares to a shrinkage of 18.9±0.3 % in z-direction. Shrinkage and density values of all cubes fabricated without green body compression are summarized in Table 3. For all samples, the alignment is assigned during the printing process, changing the orientation in the furnace has no effect on the shrinkage difference.

Table 3: Influence of layer height on linear shrinkage and density of FFF printed 316L cubes.

Layer height	z-Shrinkage	xy-Shrinkage	Relative density
mm	%	%	%
0.1	17.2 ± 0.5	21.4 ± 0.9	97.3 ± 1.4
0.2	18.7 ± 0.1	18.5 ± 1.2	92.7 ± 0.7
0.3	18.9 ± 0.3	17.3 ± 0.6	89.6 ± 0.9

Specimens subjected to quasi-isostatic compression in green state show reasonable differences in the shrinkage behaviour. Linear shrinkage in z-direction is reduced to a value of 10.3±1.7 %, while the shrinkage in xy-direction increases to 23.5±2.2 %. Detailed values of this test series are listed in Table 4.

Table 4: Influence of layer height on linear shrinkage and density of FFF printed 316L cubes subjected to quasi-isostatic compression in green state.

Layer height	z-Shrinkage	xy-Shrinkage	Relative density
mm	%	%	%
0.1	10.3	23.1 ± 0.6	97.2
0.2	8.3	26.4 ± 1.6	91.5
0.3	12.4	21.1 ± 0.5	92.9

The observations of these comparative sintering trials lead to two conclusions: First, the theory of reduced particle packing between adjacent printed layers in the case of conventional FFF (section 3.4, [143]) is supported, giving an explanation of the higher z-shrinkage of solely printed green bodies with large layer height. The anisotropy of the green body powder packing directly results in the anisotropic shrinkage during the sintering process. Second, the compression in a hot press is not appropriate to create isostatic densification despite the restricted radius of the cylindrical samples that prevents lateral squeezing. However, the generation of higher particle packing in the z-direction by pressurization in the green state has proven successful, as it leads to significantly reduced z-shrinkage. Figure 34 sketches the densification processes leading to shrinkage of the compressed green body as opposed to the uncompressed state in Figure 17b. Compression contributes to close vertical particle packing, while lateral squeezing results in greater particle spacing in the xy-plane due to non-isostatic compression. As a result, the densification during sintering results in reduced linear shrinkage in z-direction, while the linear lateral shrinkage is of the same order of magnitude as for the uncompressed specimen. With this information, linear shrinkage during MF³ can be reduced to uniformly 10 % in each spatial direction by applying green body compression. If isostatic compression can be exerted as reported in [239, 240], uniform shrinkage can be created. This allows for better predictions of final part shape and broadens design possibilities.

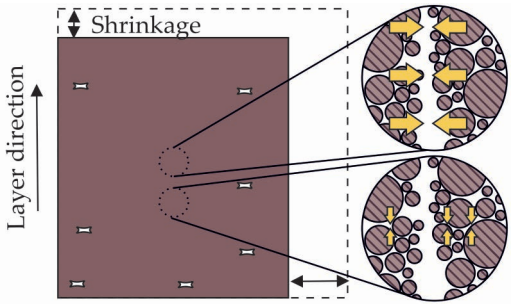

Figure 34: Process-induced shrinkage anisotropy of MF³ components with deliberate overextrusion by optimized printing strategy and quasi-isostatic uniaxial compression in green state. The particle packing between adjacent layers is enhanced and a reduction of z-shrinkage is achieved.

The results on non-compressed cubes prove that another strategy to increase the packing density of particles in the z-direction is a reduction of the layer height during FFF printing. This measure not only reduces shrinkage, but is directly related to an increase in density of more than 7 % (Table 3). Based on these findings, the layer height of 0.1 mm was identified as most suitable for printing of MF³ green bodies and used for all samples investigated in the scope of this work.

In the same context, a higher powder content of the filament directly leads to higher powder packing in the green body, resulting in lower shrinkage and higher sintering density. This correlation was demonstrated on Ampersint 1557.02 filaments with 50 vol%, 55 vol% and 60 vol% powder content and values are given in Table 5 [234].

Table 5: Influence of filament powder ratio on linear shrinkage and sintered density of Ampersint 1557.02 tool steel.

Filament infill vol%	z-Shrinkage %	xy-Shrinkage %	Relative density %
50	16.5 ± 1.0	20.1 ± 2.6	95.1 ± 0.3
55	12.9 ± 1.2	9.6 ± 1.2	94.1 ± 0.9
60	12.6 ± 1.2	16.0 ± 1.7	96.0 ± 0.6

In the comparison between 50 vol% and 60 vol% the improvement caused by an increase of the filling ratio is evident. The corresponding SEM images (Figure 35) show a decrease in residual porosity with increasing filament filling level, which is apparent from a decreasing number of pores. The behavior of the 55 vol% samples is not consistent and differs from the expected trend. This deviation is due to printing defects, which are significant when measuring the entire sample and differs from the bulk behavior, which follows the general trend.

The highest density was obtained for the highest powder content of 60 vol%. However, due to the high solids loading, this filament was very brittle and printing was only possible by feeding the filament manually. Therefore, to ensure stable process control, a powder content of 55 vol% was selected for all further filaments used in this work.

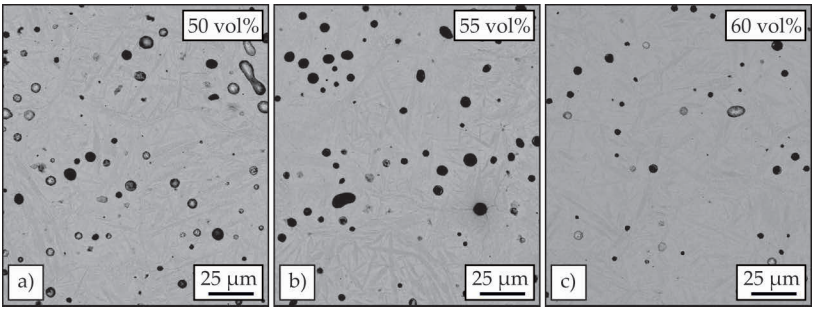

Figure 35: Microstructure of sintered Ampersint 1557.02 parts of different filament fillgrades.

In order to achieve thorough densification, high sintering temperatures close to the solidus temperature are applied. Long sintering times can also contribute to an increase in final density. Systematic sintering trials on 316L confirm an increase in density with increasing sintering temperature and sintering time (Figure 36a).

The combination of high sintering temperature and long sintering time can cause excessive grain growth. A coarse grain structure after sintering reduces the strength of the sintered materials. Grain boundary pinning pores or carbides at grain boundaries can counteract grain growth and contribute to conserving the fine grain structure [139]. However, since the mobility of pores is lower than the velocity of the grain boundary in the case of strong grain growth, pore isolation and deformation often occur in the final stage of sintering. Isolated pores cannot be completely eliminated in pressureless sintering. The final densities achieved in MF³ after optimization of all process parameters are in line with values for pressureless sintered components from the literature [137], where residual porosity of 2 % to 8 % in the form of isolated, spherical pores is reported.

Larger defects introduced during previous process steps cannot be compensated by pressureless sintering and remain as pores with a characteristic shape that can be recognized in Figure 36b. Pores emerging from printing show the typical rhombic or triangular shape resulting from the layered structure and are marked in yellow. Defects from thermal debinding can be recognized as cracks along printed layers (red arrows) or hemispherical gas pores. The formation of these two types of defect-related porosity can be avoided. Then, only the spherical gas pores

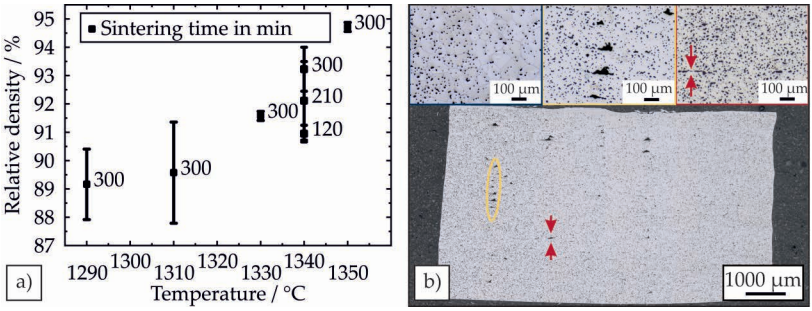

Figure 36: a) Relative sintered density of 316L as a function of sintering temperature and sintering duration. b) The remaining porosity corresponds to three different types, according to the coloration: blue: spherical gas pores, yellow: systematic printing defects and red: cracks along printed layers.

marked in blue in Figure 36b remain after pressureless sintering. Through optimal process control, final relative densities of 90.5 % to 98.7 % of the respective materials are achieved in MF³. Application of external force by HIP can further enhance densification, but is opposed to the mold-free production and the cost-effective approach of the MF³ process. In the context of this work, additional HIP as a post-processing step following pressureless sintering was exemplarily investigated for the CoWAlloy3 as a prove of concept. The results show that for pre-sintered samples with a relative density of at least 88.5 %, a density increase of 8.4±0.5 % can be realized. Thus, relative densities of more than 99 % were achieved. Further application of HIP on other materials was dispensed with in favor of cost efficiency.

The final density obtained strongly influences the mechanical and functional properties of the manufactured parts. For 316L, a correlation between the Vickers hardness and density was found, that is visualized in Figure 37a. A high pore content reduces hardness, which is associated with a reduction in mechanical strength. The slightly lower hardness for the highest density of 96 % indicates grain growth and decarburization due to extended sintering in vacuum that counteracts the increasing effect of the higher density.

Not only the mechanical properties but also the the functional properties show a strong dependence on the relative density. In the case of copper, the electrical conductivity is strongly decreased by remaining pores

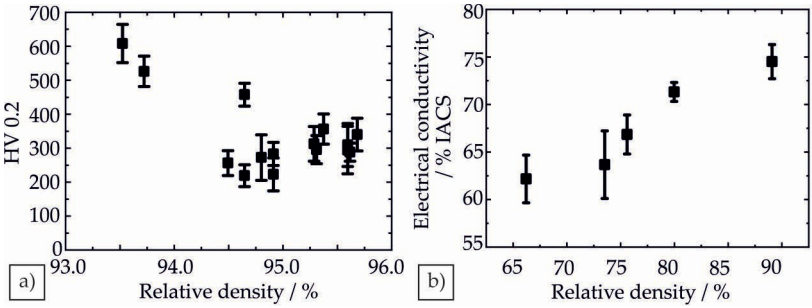

Figure 37: Influence of sintered density of properties of MF³ specimen: a) Hardness of 316L as a function of relative density. b) Correlation between relative density and electrical conductivity of copper specimens.

(Figure 37b). For the achieved relative density of 89.1 %, the electrical conductivity reaches 74.5 % of the international annealed copper standard (IACS). The dependence of material properties such as strength, ductility, conductivity and magnetic saturation on the density of sintered samples has also been demonstrated by German and is sketched in (Figure 19) [74]. Based on these measurements, it can be concluded that achieving a high relative density after sintering is crucial for successful MF³ processing.

In addition to the necessary material-specific thermal activation, further process parameters must ensure high sintering activity. These include avoiding oxide formation by selecting a furnace atmosphere of low pO_2. It is therefore necessary to choose the appropriate sintering atmosphere in combination with the best suitable sintering temperatures for each individual material. Only then can MF³ processing create parts of high sintered density for high mechanical strength and good functional performance.

6.4 MF³ of selected materials

The applicability of the MF³ process to the fabrication of different materials depends on their corresponding sinterability in conventional furnace processes. Crucial for successful processing is an onset of the first sintering activity at temperatures above the decomposition temperature of the binder polymer [81]. Sintering parameters need to be adapted to the

specific material while targeting a high sintering density and avoiding excessive grain growth. The nature of MF³ with debinding and sintering as part of the process chain results in increased O and C content in the fabricated part. The oxygen originates from the remaining O_2 content inside the furnace atmosphere and formed oxides inhibit densification during sintering [144]. The formation of carbides that results from carbon adsorption of binder degradation products causes embrittlement of the component in the final sintered state [246]. Both elements, can reduce the mechanical properties. Maintaining high chemical purity of the processed material by limiting the oxygen and carbon content through the selection of the appropriate furnace atmosphere is therefore critical to the performance of the manufactured components.

As part of this work, the applicability of the MF³ for the additive manufacturing of various materials was investigated. As a starting point, Al_2O_3 was studied, which is insensitive to atmospheric influences. However, the main focus of this work lies on the processing of metallic materials. For this purpose, 316L and IN 718 were selected, which have already been intensively researched and are widely used. Additionally, high-quality metals and alloys for functional applications that are difficult to process by conventional manufacturing were examined.

6.4.1 Al_2O_3

Manufacturing of ceramic components traditionally involves the use of binders and final densification by sintering [148]. Ceramics should therefore also be suitable for processing in the MF³. In this work, Al_2O_3 as a common ceramic was selected and its processability was investigated experimentally. Details on processing parameters and the resulting microstructures and properties of MF³ Al_2O_3 will be given in the following section. Parts of the presented results were obtained in the scope of the master thesis of Jorrit Voigt [247].

Processing of Al_2O_3

Al_2O_3 was manufactured using filaments with a powder content of 53 vol% and the binder system described in section 5.1. The ceramic powder was supplied by Krahn Chemie GmbH, Hamburg, Germany) with an average particle size of 0.1 µm to 0.3 µm (measured by laser diffraction as provided by the supplier) and chemical composition as listed in Table 6.

Table 6: Composition of Al_2O_3 powder (Taimicron TM-DAR) as provided by the supplier.

Al_2O_3 %	Si ppm	Fe ppm	Na ppm	K ppm	Ca ppm	Mg ppm
> 99.99	< 25	< 15	< 10	< 5	< 5	< 5

The Al_2O_3 filament exhibits pores with a size of 5 µm to 20 µm observable in Figure 38a in light microscopy images of cross-sections. These pores were introduced during compounding and extrusion of the feedstock and are randomly distributed. Despite the presence of these small pores, compounding of the powder-binder mixture can be considered successful, as the irregular ceramic particles are homogeneously dispersed inside the binder system (Figure 38a).

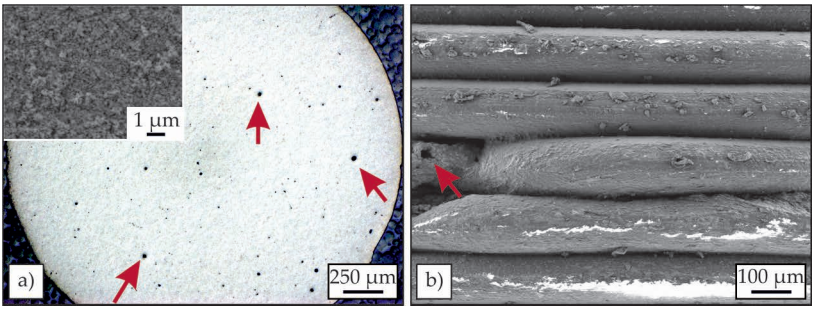

Figure 38: a) Cross-sectional image of alumina filament with randomly dispersed pores. A homogeneous distribution of powder particles inside the filament was achieved. b) Layered lateral surface of a FFF alumina green body printed with optimized parameters. Pores in the filament remain within the deposited strands even after FFF, as shown by red arrows.

Printing parameters for FFF of Al_2O_3 filaments were evaluated in experimental test series. At temperatures below 260 °C the extrusion process through the 0.8 mm nozzle was frequently interrupted due to nozzle clogging. To ensure process stability, the nozzle temperature was set to 280 °C. This high temperature is required to compensate the viscosity increase emerging from very small particle sizes and the irregular particle shape of the brittle ceramic powder [74]. Use of high nozzle temperatures

contributes to higher tolerance to local viscosity fluctuations or variations in temperature control during printing. It enables FFF of Al_2O_3 green bodies with layered surface structure as show by electron microscopy in Figure 38b. The SEM image of the surface reveals pores inside the deposited strands, which originate from the filament and persist after the printing process. The print bed temperature was set to 90 °C to overcome first layer adhesion problems appearing at lower temperatures. Infill during printing was increased to create deliberate over-extrusion and prevent formation of systematic print-related pores (as explained in detail in section 6.1.1). Overlap between adjacent layers and the extrusion multiplier were set to maximum possible values that still allowed to meet the requirements of dimensional accuracy (EM 1.1 at 90 % overlap). The complete parameter set used for FFF of alumina filaments is displayed in appendix B, Table 28. No additional compression or milling was applied to the Al_2O_3 green bodies.

The contained TPE was successfully removed in cyclohexan, creating a mass loss of 5.97 wt%. Defect-free thermal debinding was possible at a heating rate of 1 °C min^{-1}. The irregular particle shape has advantages in binder removal, as the irregular particle surface causes a high level of friction between neighboring particles. This creates high stability of the samples at all times along the process chain and allows relatively fast heating. Due to the high melting temperature (2050 °C) of the ceramic [248], sufficient strength for handling of the debond brown bodies could only be generated after holding at 900 °C for 180 min.

An argon atmosphere was chosen for sintering at a temperature of 1414 °C. This temperature corresponds to the upper limit of the used furnace, implying that higher temperatures could not be tested in the scope of this work. When sintering for 5 h at this temperature, a relative density of 98.5 % was achieved. Longer sintering times of up to 600 min did not result in a significant increase in density in the conducted test series. Results of the sintering trials are summarized in Table 7.

Despite the limitations of the furnace, which restrict the sintering temperature to a maximum of 1414 °C, high relative densities were achieved for sintering durations of 300 min. The results indicate that the small particle size of the ceramic powder contributed to high sintering activity, especially since the filament introduced additional pores into the green body. As the melting temperature of Al_2O_3 is much higher that tested sintering temperature, it is expected that further densification and

Table 7: Density of Al_2O_3 after sintering at 1414 °C in dependence on the sintering time [247].

Time min	Density g cm^{-3}	Relative density %
60	3.81 ± 0.0	96.4 ± 0.5
300	3.89 ± 0.0	98.7 ± 0.1
600	3.90 ± 0.0	98.9 ± 0.1

shortening of the sintering time is possible if the sintering temperature is increased. However, this hypothesis was not proven experimentally.

The microstructure of sintered Al_2O_3 displayed in Figure 39a is fine-grained and exhibits residual porosity. Most of the pores are still connected in small networks, indicating that the final stage of the sintering process has not yet been reached.

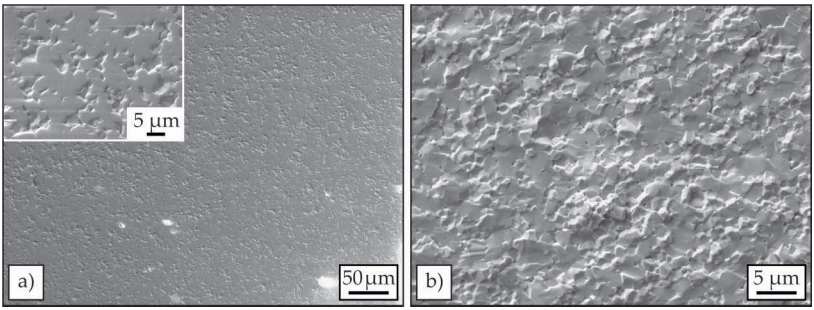

Figure 39: a) Cross-sectional image of sintered Al_2O_3. b) Fractured surface of sintered Al_2O_3.

The grain structure is discernible on the fracture surface in Figure 39b. Grains of approx. 1 µm size can be recognized with spherical micropores at grain boundary triple points. Cleavage-like fracture surfaces can be identified on some of the grains, which reveal the brittle fracture behavior of the ceramic.

Properties of Al_2O_3
For mechanical characterization of the sintered Al_2O_3 specimens, the flexural strength was determined by means of 3-point bending tests following DIN EN 843-1, 2008 [231]. Bending strength of sintered specimens reached 335.2±64.7 MPa [247]. Literature reports a bending strength of 400 MPa for 99.5 wt% pure Al_2O_3 [248]. The reduced bending strength of sintered samples is due to the remaining porosity after pressureless sintering at 1414 °C. Likewise, the low Weibull modulus of 5.4, that was measured in [247], is a result of the processing history and indicates the need for optimization in future investigations.

The results obtained in the scope of this work show the high potential of the presented process chain for additive manufacturing of oxide ceramics. Competing AM technologies require either high-temperature preheating as for LPBF or implementation of dopants to improve final part properties in EPBF [249]. In all of these single-step methods, the feasible geometries are limited and costs are high. Alternative multi-step AM processes have been promoted for a variety of ceramics, but still require further investigations to overcome remaining deficiencies in mechanical properties and performance [250]. The MF³ can therefore be considered a promising approach for additive manufacturing of ceramics and should be further improved by using increased sintering temperatures to reduce the amount of remaining porosity observed in this work and likewise reported in existing literature [251].

6.4.2 Steels

Steels comprise the most variant group of metallic materials. The processability of steels in the MF³ was investigated in this work using the example of a corrosion-resistant austenitic chromium steel (316L) and a hot work tool steel (Ampersint 1557.02). The basic task, as for all metals, is to maintain the sintering activity by preventing oxide formation. Furthermore, specifically for steels, the control of the C-content is essential to achieve the targeted microstructure and high mechanical strength. A detailed evaluation of suitable processing parameters and resulting material properties is presented in the following section.

Processing of 316L
The austenitic stainlees steel 316L (Micro-Melt™316L, Carpenter Technology Corp., USA) was selected for its wide range of applications. Some

results of the following section were obtained as part of the author's master thesis [252] and have already been published in [232]. The exact composition as provided by the supplier is listed in Table 8.

Table 8: Composition of 316L powder as provided by the supplier.

Fe wt%	C wt%	Si wt%	Mn wt%	P wt%	S wt%	Cr wt%	Ni wt%	Mo wt%	Cu wt%
bal.	0.017	0.55	1.28	0.019	0.006	16.3	10.2	2.05	0.1

The particle size distribution of the gas atomized 316L powder was measured by optical analysis (Camsizer XT, Retsch Technology, Germany). In Figure 40b, the results of the analysis are plotted in terms of the relative particle fraction within the specified size class of 2 µm and as the cumulative fraction of the particle size. According to this measurement, the mean particle size is 17.7 µm, with D_{50}=16.3 µm and D_{90}=25.4 µm.

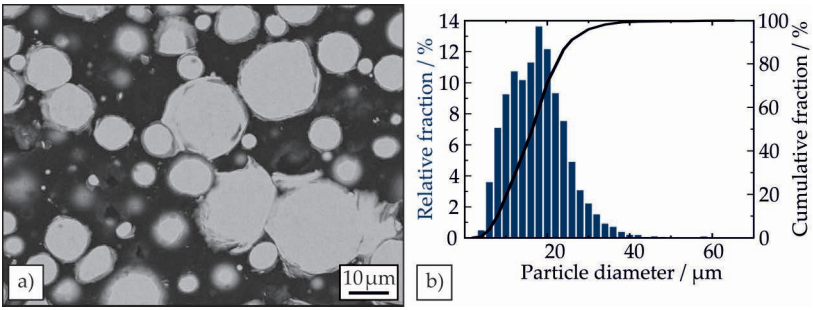

Figure 40: a) SEM image of the filament cross-section showing the good powder quality and achieved distribution of 316L particles b) Particle size distribution of the used gas atomized 316L represented as relative particle fraction within the specific size class and cumulative curve as measured by optical analysis.

The powder content in the filament is 55 vol% and particles are dispersed and encapsulated in the network structure of the organic binder system (Figure 40a). A high nozzle temperature of 290 °C enables a stable printing process using a nozzle diameter of 0.6 mm. The further parameters, which were experimentally determined for printing with high infill, are listed in Table 29 in the appendix B. Following the shaping of green bodies, solvent debinding using cyclohexane was successfully carried out

without any need of additional measures. After extraction of 5.72 wt% of the main binder component, SEM images (Figure 28) provide evidence for the existence of pore channels inside the sample. During thermal debinding in vacuum levels of 1×10^{-3} mbar, oxidation starts on the surface of the steel particles at 750 °C (Figure 41b).

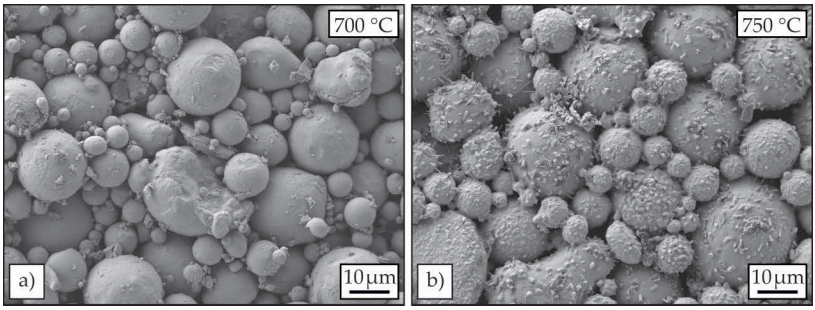

Figure 41: SEM image of the fractured surface after thermal debinding and pre-sintering at a) 700 °C and b) 750 °C in vacuum levels of 1×10^{-3} mbar. The onset of oxidation is clearly visible at 750 °C.

Up to 700 °C, as can be seen in Figure 41a, the particle surfaces are smooth and virtually unaffected by oxidation. In contrast, micrographs after a holding time of 90 min at 750 °C show rod-shaped structures (Figure 41b) on the particle surfaces. EDX measurements show increased oxygen content in case of the higher pre-sintering temperature, indicating oxide formation on particle surfaces. In the pendular state during debinding, these oxides provide increased friction between neighboring powder particles and thus increase the stability of the brown bodies after complete binder removal. In the further course of the process, however, oxides reduce the sintering activity and inhibit the progress of densification [144]. Based on the results of thermal debinding, an atmosphere with low oxygen partial pressure in vacuum levels of 1×10^{-4} mbar was applied in the scope of this work to achieve high sintering densities.

Sintering studies at different sintering temperatures and times show an increase in density with increasing temperature and sintering time. The highest density of 7.56 g m^{-3}, corresponding to a relative density of 95.7 %, was obtained by sintering for 300 min at 1350 °C. All measured densities of the test series for parameter optimization are given in Table 9.

Table 9: Sintered density of 316L parts for thermal debinding and sintering in vacuum.

Temperature °C	Time min	Density g m^{-3}	Relative density %
1290	300	7.11	90.1
1310	300	7.15	90.5
1330	300	7.31	92.5
1340	300	7.44	94.2
1350	300	7.56	95.7
1340	120	7.26	91.9
1340	210	7.35	93.0
1340	300	7.44	94.2

The marked reduction in porosity when increasing the sintering temperature from 1330 °C to 1350 °C is confirmed by light and electron microscopy images presented in Figure 42. In addition to the differing densities, significant distinctions are also apparent with respect to the grain sizes and the local distribution of the grain sizes. Towards the edges, the microstructure is finer, indicating an influence of the atmosphere. Diffusion of oxygen into near-surface regions results in an increased amount of remaining porosity and inhibits grain growth. At the sintering temperature of 1350 °C, regions in the interior of the sample that remain unaffected by the atmosphere are subject to massive grain growth (Figure 42e). A reduction in sintering temperature of just 20 °C considerably reduces the tendency to grain growth and produces a much finer microstructure in the 1330 °C sample (Figure 42a).

SEM images taken in the transition zone from near-surface regions to the coarse grained bulk of the sample (Figure 42b, d & f), reflect the grain growth induced by increased sintering temperatures. This trend is especially evident at 1350 °C. Porosity, consistent with Archimedes density measurements, differs in amount and pore size among the three samples. The high amount of elongated pores in Figure 42b, after sintering at

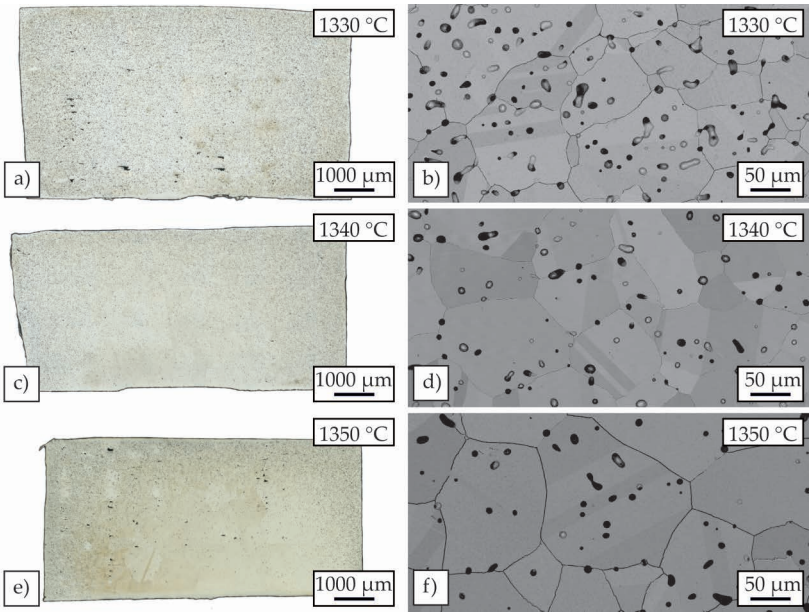

Figure 42: Cross-sectional light microscopy of samples sintered at 1330 °C, 1340 °C and 1350 °C for 300 min demonstrate massive grain growth starting at 1340 °C. In near-surface regions the grain size remains finer due to pinning effects of inter-diffusing atmospheric oxygen.

1330 °C indicates an incomplete sintering progress. At higher temperatures, the pores become increasingly spherical, with the proportion of pores at grain boundaries decreasing with increasing temperature. At 1350 °C, the pores are mostly located inside the strongly grown grains, isolated and detached from the grain boundary (Figure 42f). The pronounced grain growth already occurs at 1340 °C, so that in favor of a higher density, a sintering temperature of 1350 °C was defined as the optimum value, accepting the resulting grain growth.

Since an influence of the atmosphere is clearly recognizable in surface-near regions despite the selected vacuum processing, comparative sintering tests were carried out in argon and forming gas (Ar with 5 % H_2). Sintering at 1340 °C for 300 min was chosen to evaluate the remaining

porosity and grain size. SEM images provided in Figure 43 allow a comparison of the resulting microstructure in dependence of the sintering atmosphere.

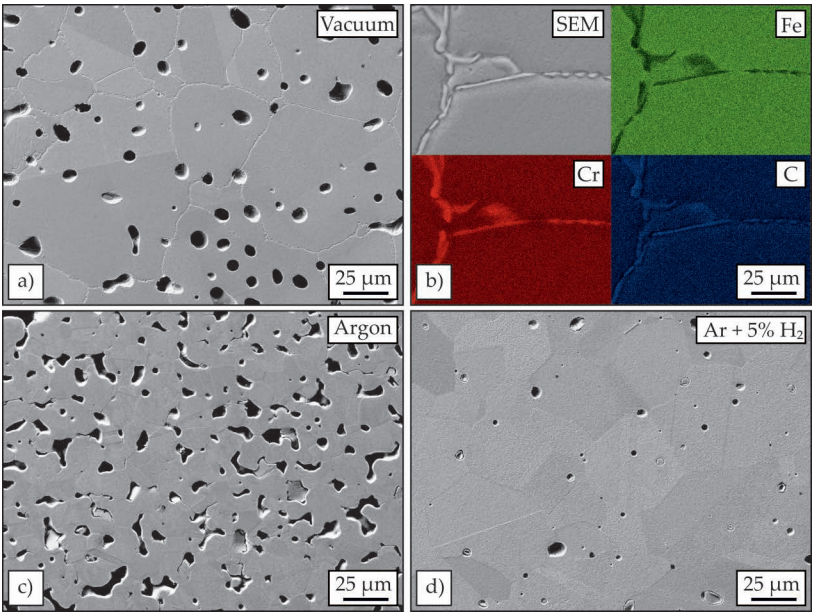

Figure 43: Microstructure of 316L after sintering at 1350 °C for 300 min in a) vacuum, c) argon or d) reducing atmosphere. b) In vacuum sintered samples, a grain boundary phase has been formed, with enrichment of chromium as proven by EDX.

Argon processing results in a high residual porosity of 11.5 % which is clearly visible in Figure 43c. The incomplete densification is the result of oxide formation on particle surfaces which leads to reduced sintering activity. Thus, as a clear result of the comparison of atmospheres, it can be stated that argon could not sufficiently decrease the pO_2 and is unsuitable for achieving high sintering activity. Reducing atmosphere due to the H_2 content in forming gas, on the other hand, produces the lowest residual porosity of only 3.7 % (Figure 43d). For vacuum sintered samples the formation of a GB phase can be clearly detected in Figure 43a. EDX analyses in Figure 43b show an enrichment of chromium in these grain boundary regions, while the iron content is markedly reduced. Since

the carbon concentration is increased as well, the grain boundary phase is identified as $Cr_{23}C_6$ which is the rapidly formed GB carbide in 316L austenitic steels [253]. The formation of this carbide is the result of rapid diffusion along the grain boundaries in combination with carbon uptake during thermal debinding that can be measured as an increase to 0.3 wt%. Nevertheless, it is important to note that no chromium depleted zones were detected in areas close to the grain boundary. The high temperatures and long sintering times give enough time for chromium diffusion and lead to balanced Cr concentrations above the passivation threshold [254]. A reduction in the resistance to intercrystalline corrosion is therefore not expected for MF³ 316L.

Based on the microstructural analysis, processing in forming gas achieves highest densification and homogeneous microstructure. Vacuum processing is also suitable to create high relative density (93.8 %), but removal of binder degradation products is less effective, resulting in the formation of GB carbides. This leads to the conclusion that in addition to density and microstructure, the mechanical properties must also be taken into account in order to determine the processing atmosphere.

Properties of 316L

Mechanial strength was determined under tensile loading. The measured stress-strain curves of micro-tensile tests are shown in Figure 44 in comparison to the benchmark sheet material. The specific values of ultimate tensile strength and fracture elongation of the individual specimens are listed in Table 10.

Table 10: Mechanical properties of 316L specimens in dependence of the sintering atmosphere. Measured values of a conventionally manufactured sheet material serve as a reference.

Specimen -	Tensile strength MPa	Elongation at break %
Reference	511.3 ± 7.3	46.9 ± 0.8
Vacuum	411.6 ± 58.7	33.7 ± 7.8
Ar + 5 % H_2	250.1 ± 55.9	29.1 ± 9.2

The highest tensile strength of MF³ 316L is achieved in the vacuum sintered specimens, which reach 411.6±58.7 MPa compared to a value of

511.3±7.3 MPa that was measured for the reference material. In contrast, the specimens sintered under forming gas exhibit only half the strength of conventional 316L. In terms of ductility, a reduction is observed for MF³ 316L of both sintering atmospheres compared to conventional production. However, one of the forming gas specimens even reaches the elongation at fracture of the reference specimen. As the high standard deviation of sintered MF³ specimens indicates, parts of the specimens in both sintering atmospheres result to have significantly reduced mechanical properties, especially strongly reduced elongation at fracture (Figure 44a). This random occurrence of reduced properties indicates inadequacies in the process chain, presumably in the printing process, which lead to serious defects in the final part. In order to reliably produce good properties, the reproducibility of defect-free shaping must therefore be increased. Then, sintering in vacuum can deliver 316L with high strength at slightly reduced ductility.

Microscopic examinations show strong necking of the reference material during microtensile testing. Fracture surface analyses by SEM confirm the ductile fracture behavior with honeycomb formation. Specimens sintered in forming gas exhibit a similar appearance of fracture surfaces, but with a high percentage of pores inside the significantly larger honeycombs. Vacuum specimens show mixed fracture, due to an increased carbon content resulting from incomplete binder removal. Together with the high amount of pores that is visible in Figure 44d, these brittle regions explain the abrupt fracture of sintered specimens after reaching the yield point.

If major defects can be avoided by optimized processing parameters, 316L can be produced to relative density up to 96.3 % in MF³ by pressureless sintering in vacuum or forming gas. Microtensile tests prove that strains in the range of the conventionally manufactured reference material are achievable for both atmospheres. After sintering in the H_2 containing atmosphere the tensile strength is markedly reduced, making the specimens unsuitable for load-bearing applications. In contrast, the specimens sintered in vacuum achieve high mechanical strength of 80 % of the benchmark sheet material. The lower strength can be attributed to the remaining porosity together with the high grain size after sintering. To increase the mechanical strength, the possibility of obtaining a finer microstructure and lower porosity by sintering under pressure in HIP at a lower sintering temperature below 1340 °C should be investigated in future test series.

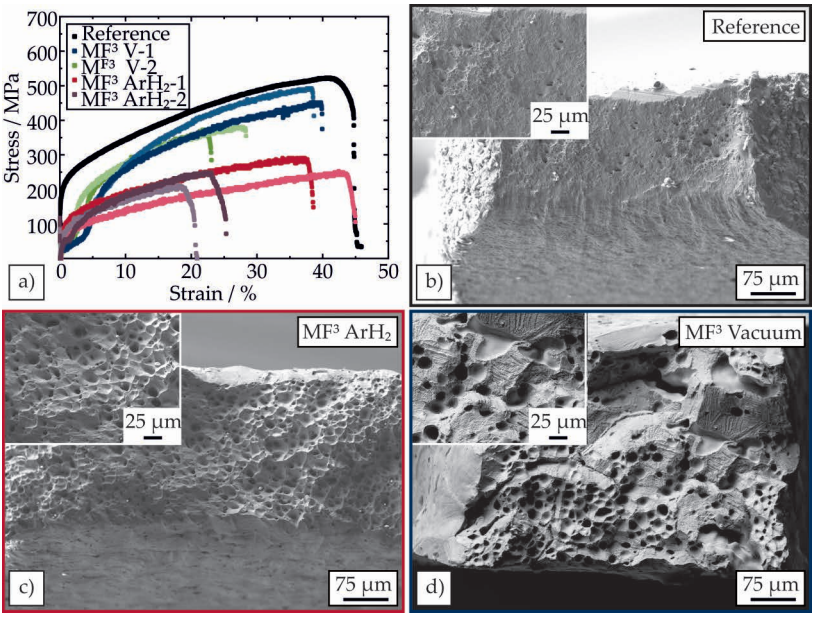

Figure 44: Mechanical performance of 316L as measured by micro-tensile tests: a) Stress-strain curves of conventional rolled material (black) and sintered MF³ specimen of two vacuum batches (green and blue) and two forming gas batches (red and purple). Fractured surface of specimens after micro-tensile testing of b) benchmark sheet 316L, c) MF³ 316L sintered in forming gas and d) vacuum sintered MF³ specimens.

Processing of Ampersint 1557.02

The X40CrMoV5-1 hot work tool steel (Ampersint 1557.02) (H.C. Starck GmbH, Munich, Germany) which was investigated in this work is very similar in composition to the widely used AISI H13. The most important alloying elements are listed in Table 11.

Gas atomized powder with a maximum particle size of 45 µm was used for processing in MF³. Cross-sectional SEM images were used to prove homogeneous particle distribution inside the filament (Figure 45a). Additionally, a good powder quality is shown in Figure 45b, as particles are free of any internal porosity.

Printing of Ampersint 1557.02 green bodies was realized by analogy to other metal-load filaments, with parameters as listed in Table 30 in

Table 11: Composition of Ampersint 1557.02 powder as provided by the supplier.

Fe wt%	C wt%	Cr wt%	Mn wt%	Mo wt%	Si wt%	V wt%
bal.	0.38	5.30	0.51	2.73	0.53	0.55

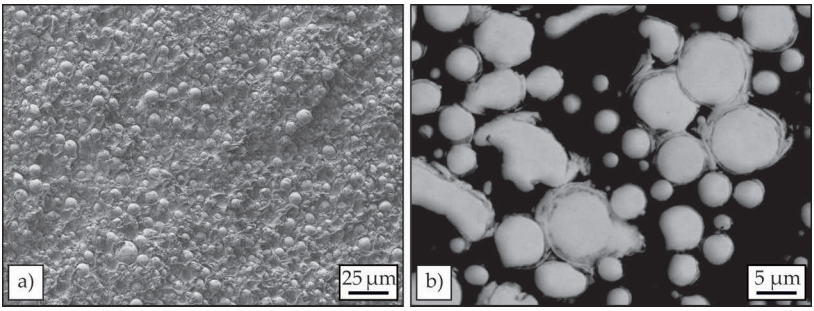

Figure 45: The cross-sectional SEM image of the tool steel filament shows a) homogeneous distribution of powder particles that b) are free of internal porosity.

appendix B. Polymer removal during debinding was successfully carried out using the parameters already optimized for 316L. For thermal debinding, a minimum heating rate of 0.2 °C min^{-1} was selected. Vacuum, argon and forming gas (consisting of Ar with 5 % H_2) were used to investigate the influence of furnace atmospheres on the chemical composition and microstructure after sintering. 300 min at 1275 °C were chosen for first sintering trials and the resulting sintered density and Vickers hardness in the as-sintered state after slow furnace cooling at 3 °C min^{-1} were measured. Table 12 summarizes the results and indicates that the highest density can be obtained in vacuum. Forming gas leads to slightly lower densities while argon processing again gives significantly worse results.

With regard to hardness, the vacuum samples reach 433.2±21.1 $HV_{0.2}$, while both gas atmospheres lead to much lower values. The limit of 250 $HV_{0.2}$ demanded for the solution-annealed condition [255] according to DIN EN ISO 4957:2018, is not achieved for sintering in argon or forming gas. These low hardness values indicate decarburization during sintering, and imply that the two gas atmospheres are not suitable for sintering. Tool steels must necessarily maintain a C-level between 0.35 wt% to 0.40 wt%

to achieve a hardness above 500 $HV_{0.2}$ in heat-treated condition, that is required for the application [255].

Table 12: Sintered density and corresponding hardness of Ampersint 1557.02 parts after sintering at 1275 °C, 300 min in different atmospheres.

Atmosphere -	Density g cm^{-3}	Hardness $HV_{0.2}$
Vacuum	7.32	433 ± 21
Argon	6.96	143 ± 19
Ar + 5 % H_2	7.29	121 ± 11

Based on these results, a series of tests was carried out in vacuum to determine the best combination of sintering temperature and sintering time [256]. Table 13 summarizes the resulting density values and shows an increase in density with increasing sintering temperature and sintering time.

Table 13: Sintered density of Ampersint 1557.02 parts for thermal debinding and sintering in vacuum.

Temperature °C	Time min	Density g m^{-3}	Relative density %
1300	300	7.37	93.9
1325	300	7.30	93.0
1350	300	7.57	96.4
1375	300	7.64	97.3
1350	120	7.37	93.9
1350	210	7.59	96.7
1350	300	7.57	96.4

For further sample preparation 300 min at 1350 °C was chosen as the best parameter combination to reliably achieve high sintered densities.

The tool steel requires a multi-step heat treatment prior to application in order to achieve high hardness and good ductility. For this purpose, hardening is first performed by austenitizing at 1050 °C and oil quenching. A minimum soaking time of 30 min is to be applied. This is followed by two-stage tempering at 500 °C for 2 hours each with air cooling. The standard specifies a slow heating rate during hardening to avoid cracking [257]. To prevent decarburization during the austenitizing process, the hardening treatment was conducted in argon atmosphere. Nevertheless, a decrease in hardness to 377±54 $HV_{0.2}$ was observed after heating with 10 °C min^{-1}, indicating a too long processing time that led to significant decarburization. The use of a stainless steel foil, in which parts are tightly wrapped during austenitization, was suitable to reduce this carbon evaporation. Thus, a higher hardness of 680±32 $HV_{0.2}$ was achieved, which is also higher than in the as-sintered condition (599±54 $HV_{0.2}$). Since no cracking due to thermal stresses during heating is to be expected with the small wall thicknesses of the MF3 samples, austenitizing in a preheated furnace was evaluated as an alternative. For this purpose, the sample without stainless steel foil was inserted at 1050 °C for 30 min and oil quenched. This last procedure resulted in the highest hardness values, i.e. 782±22 $HV_{0.2}$. Both successfully hardened and the as-sintered sample all fulfill the requirement of DIN EN ISO 4957 [255]. Resulting microstructures are shown in Figure 46.

The as-sintered sample, which represents the initial condition, shows a martensitic microstructure despite the slow cooling in the furnace. This confirms the high hardness values measured after vacuum sintering and indicates a high carbon content after MF3 processing. In contrast, in Figure 46b a purely ferritic microstructure can be observed after decarburization during the long heat treatment, including slow furnace heating. This finding matches the low measured hardness of this sample. The two other approaches were suitable to achieve a high density after oil quenching. Consequently, both samples show martensitic microstructure with some amount of retained austenite in SEM images in Figure 46c & d. Based on this microstructural analysis in combination with the results of the Vickers hardness measurements, the method chosen as most successful hardening program was the one in which the sample is placed into the preheated argon furnace. Additional wrapping in stainless steel foil is not necessary in this case. The subsequent tempering was performed in air, as the maximum temperature of 500 °C is low enough and does not lead

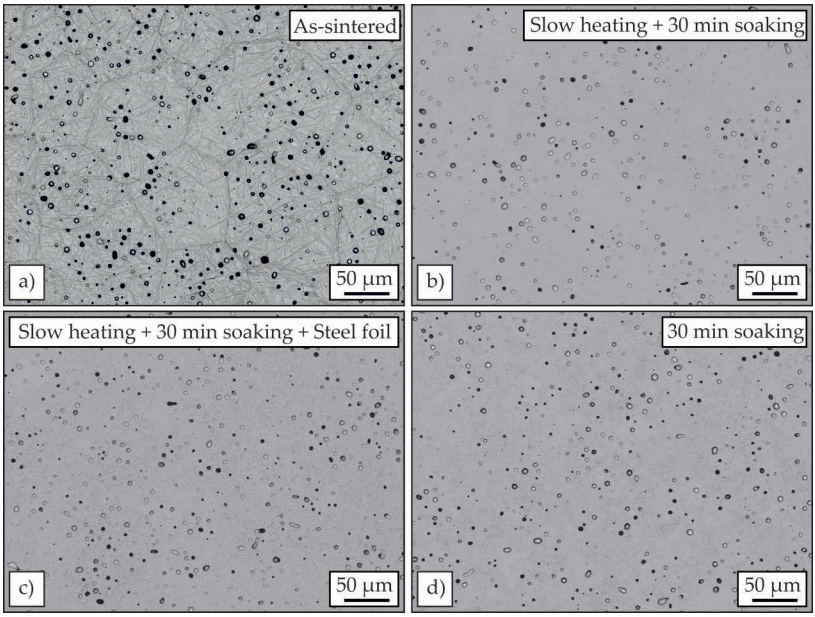

Figure 46: Microstructure of a) as-sintered Ampersint 1557.02 in comparison to different heat-treated microstructures: Slow heating & 30 min soaking b) without wrapping in stainless steel foil and c) using steel foil. d) Demonstrates the microstructure after 30 min soaking without previous slow heating.

to decarburization. Other additive processes investigated for the production of H13 achieve similar hardness levels, with LPBF at 680 HV [258] being higher than EPBF at 500 HV [259]. The resulting hardness in MF³ thus lies in the range of the EPBF material in the as-sintered state and above the values reported for LPBF samples in the Q & T state [258, 259].

Properties of Ampersint 1557.02

Tensile-strength of the MF³ Ampersint 1557.02 was measured by micro-tensile tests. Quenched and tempered specimens were compared to as-sintered specimens and results are presented in form of stress-strain curves in Figure 47a. An average tensile strength of 967.5±148.6 MPa at an average strain at break of 24.7±3.7 % was measured in as sintered state. These values are similar to the mechanical properties of MIM H13 in as-sintered state as reported by Besler et al. [132]. After quenching and tempering, a higher strength of 1316.8±106.7 MPa was achieved,

while the strain at break was slightly reduced to 21.4±1.5 %. Rolled reference H13 in quenched and tempered state shows similar strength (1395.38±23.60 MPa) with significantly lower standard deviation. The major difference lies in the achieved ductility, as the reference material with a higher elongation at fracture of 31.3±1.2 % shows more necking. In comparison to other AM processes, all MF³ specimens exhibit much higher ductility regardless of heat treatment condition, while powder bed processes reach maximum strains below 5 % [260].

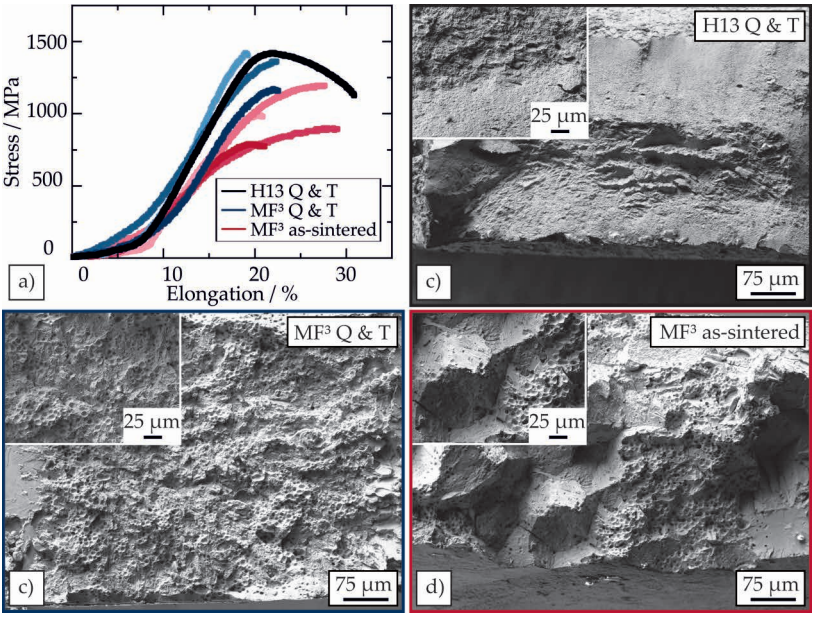

Figure 47: a) Stress-strain curves of MF³ Ampersint 1557.02 tool steel in as-sintered and Q & T state. Conventional H13 in Q & T state was measured as a reference material. Fractured surface of specimen after micro-tensile testing of b) benchmark Q & T H13, c) MF³ Q & T Ampersint 1557.02 and d) as-sintered MF³ Ampersint 1557.02.

The Q & T specimens, both the conventional and MF³ specimens, exhibit brittle fracture behavior, which is evident at the fracture surfaces in the form of a facet-like cleavage fracture. The sintered specimens additionally have a significant amount of remaining pores (Figure 47c & d). The as-sintered sample is distinguished by intergranular cleavage fracture due to weakened grain boundaries (Figure 47d).

The obtained results lead to the conclusion that Ampersint 1557.02 can be manufactured additively by MF³ if decarburization is avoided during the sintering process by using a vacuum atmosphere. As-sintered specimen after slow furnace cooling at 3 °C min^{-1} already show martensite microstructure with high hardness, mean tensile strength of 967.5±148.6 MPa and strain at break above 20 %. If carbon evaporation is prevented by keeping the soaking time short during the hardening procedure, subsequent quenching and tempering reduces the variation in tensile strength and increases the mean tensile strength to 1316.8±106.7 MPa making the additively manufactured steel suitable for application.

6.4.3 Titanium

Processing of cp-Ti

To evaluate the possibility of titanium additive manufacturing, commercially-pure ti-tanium (Gd. 1 as per ASTM F67 [1]) powder was investigated in this work and the outcomes are published in [57]. In addition to targeting high density and good mechanical strength, the focus was placed on obtaining high chemical purity. As a special measure during filament fabrication, argon gas was used in the hopper containing the titanium powder to prevent oxide formation on particle surfaces. SEM analysis of the fractured filament displayed in Figure 48a confirms a homogeneous distribution of particles, that are each individually encapsulated into the polymeric binder network.

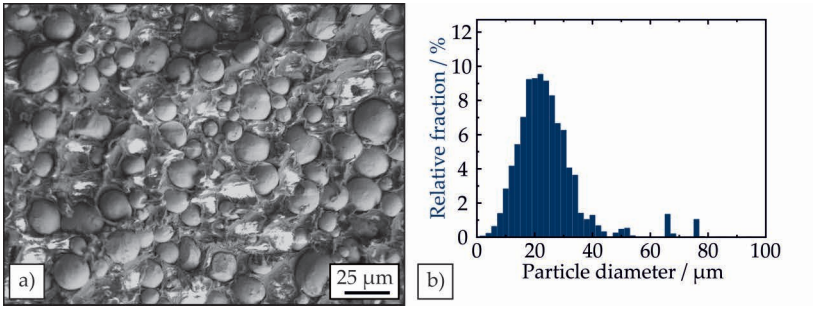

Figure 48: a) Cp-Ti particles inside the filament are homogeneously encapsulated into the polymeric binder network. b) Particle size distribution of titanium powder. Measured particles above 50 µm belong to agglomerates.

By means of optical particle size measurement, the mean particle size was determined to be 23.4 µm (D_{50}=22.1 µm; D_{90}=37.9 µm). 93.5 % of the particles are smaller than 50 µm and registered measurements in Figure 48b that indicate higher values belong to agglomerates rather than individual particles.

3D printing of titanium green bodies was realized using the parameters in Table 31 in Appendix B. Thermal debinding and sintering was carried out at a vacuum of at least 1×10^{-5} mbar, since at higher pO_2 strong oxide formation and consequently inhibited densification occurred. The previously determined temperature program with critical heating rate of 0.2 °C min^{-1} enabled successful thermal debinding. Sintering trials in vacuum at temperatures from 1300 °C to 1400 °C for 90 min, 120 min, 210 min and 300 min served to decide on the best parameter combination for achieving a high sintered density. Table 14 gives the Archimedes density measured on the entire sample after sintering in dependence of sintering temperature and time. It must be noted that the reported measurements include surface near regions that were later identified to be highly porous by SEM analysis (Figure 49b). These results are therefore not representative for the bulk of the sintered samples, that has a higher relative density. As the presented results were all obtained by the same measurement set-up they are comparable and serve for evaluation of the best sintering parameter set.

Table 14: Sintered density of cp-Ti parts for thermal debinding and sintering in vacuum.

Temperature °C	Time min	Density g m^{-3}	Relative density %
1300	90	4.05	90.0
1350	90	4.04	89.7
1400	90	4.13	91.9
1400	90	4.13	91.9
1400	120	4.00	88.9
1400	210	4.19	93.1
1400	300	4.19	93.2

Increasing the sintering temperature leads to only a slight increase in density, whereas it is observed that sintering for at least 210 min is necessary to achieve a density of 4.19 g m^{-3} (corresponding to a relative density of 93.1 %). To reliably obtain high relative density and at the same time limit grain growth that occurs during prolonged sintering at high temperatures, the medium temperature of 1350 °C was combined with an extended sintering time of 300 min. By applying additional compression in the green state as introduced in chapter 6.1.2, relative densities of 94.5 % were repeatedly achieved with this sintering parameters.

The sintered MF³ part is no longer chemically pure titanium, but contains increased carbon and oxygen contents as a result of the processing history. The resulting formation of different phases can be observed in SEM images in Figure 49. The overview image in Figure 49a proves the low remaining porosity that was successfully minimized during sintering. The light matrix structure consists of α-Ti and contains darker areas visible at higher magnification in Figure 49c that reveal differences in elemental composition; i.e. an increased amount of light elements. These darkly appearing phases are assigned to be secondary α-Ti, due to their increased content of oxygen and carbon that both act as α-stabilizing elements. NDIR measurements prove elevated carbon content (0.89±0.03 wt%) resulting from uptake of binder degradation products after processing in vacuum. Argon debinding contributes to a better removal of carbon and reduces the final C-content to 0.12±0.02 wt%, but leads to increased uptake of atmospheric oxygen (1.52±0.18 wt% compared to 0.56±0.01 wt% when using vacuum). As a result, the amount of secondary phases in the final part is lower when vacuum is applied during debinding and sintering and this option is therefore to be preferred. The discrete regions of retained α-phase that are dispersed inside the α-Ti matrix have a much higher hardness than the matrix phase due to solid solution strengthening. The same applies for the oxygen-induced α-*case* formed on the surface up to a depth of 50 µm.

Another particular microstructure can be observed at the grain boundaries in Figure 49d. The light GB-phase is either penetrated by dark lamellae or surrounded by darker regions. APT of the GB identifies the differences in composition compared to the matrix on the atomic scale. Concentrations of elements are given in Figure 49e on a logarithmic scale. The results demonstrate an enrichment of Fe along the grain boundary, together with depletion of carbon and oxygen in this region. Based on these measurements an accumulation of Fe, that is contained as a trace

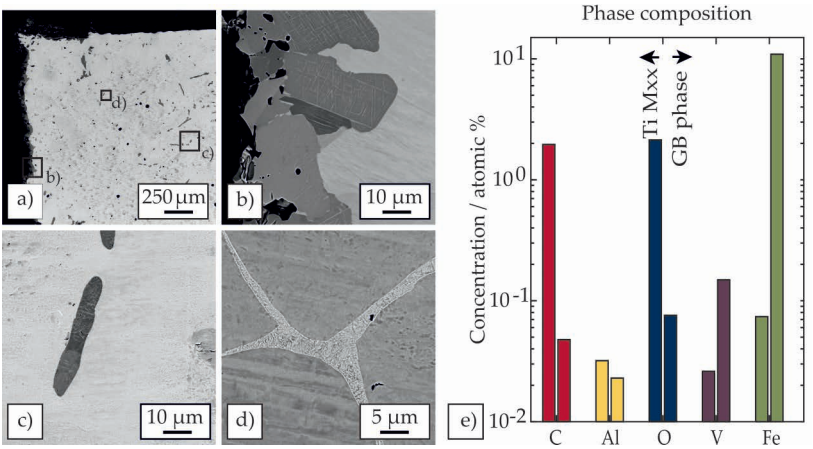

Figure 49: Microstructure of MF³ cp-Ti Titanium after debinding and sintering in vaccum atmosphere: a) Overview of one corner of the sample of which images with higher magnifications were taken, b) clear α-case along the surface with an increased amount of larger pores, c) discrete region of retained α-Ti inside the bulk material and d) lamellar α + β GB-phase. e) Comparison of elemental concentrations of main trace elements in the GB-phase and the matrix (Ti Mxx) analyzed by APT. Reprinted with permission [57].

element in the powder raw material, takes place due to enhanced diffusion along the grain boundaries. Fe acts as a β-stabilizer, conserving the body-centered cubic structure in the GB-phase up to room temperature. If the local Fe concentration exceeds 0.05 wt% the formation of a lamellar structure is induced as the microstructure undergoes an α-Ti + β-Ti two-phase region during cooling [261]. The β-formation is common for sintered titanium and was also reported by Yan et al. [170]. Darker regions that surround this GB-phase indicate depletion of Fe in nearby regions.

Properties of cp-Ti

The sintered titanium was tested in the micro-tensile setup presented before, and its behavior was compared to conventional cp-Ti sheet material. The stress-strain curves in Figure 50a demonstrate premature fracture when reaching uniform elongation that leads to a reduced elongation at break of only 18.4±1.0 % compared to 28.0±1.7 % for the reference specimens. The SEM images of the fracture surface (Figure 50b) reveal a

dimpled surface with a high number of pores. This indicates that breakage occurs as a result of pore accumulation under the applied tensile stress. This behavior can be considered a ductile fracture with micropore aggregation as the fracture mechanism. Another factor affecting the ductility is the influence of solid solution hardening, that further reduces the achieved fracture elongation. For satisfying elongations, the O-content should be limited to 0.3 wt% [73]. As a result of the high impurity content, the MF³ Ti achieves a high microtensile strength, surpassing the strength of the conventional specimen. This increase in strength correlates with the increased hardness, due to impurity uptake during debinding and sintering. It is lower than measured values LPBF Ti with similar hardness of 300 $HV_{0.2}$, for which an ultimate strength above 750 MPa is reported [262]. The measured fracture strength of 325.4±10.3 is a result of the combined effects of solid solution strengthening by impurity elements, that is almost erased by the strength-reducing remaining porosity.

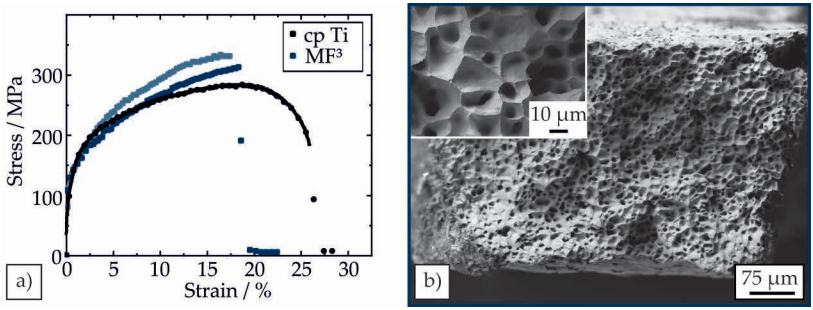

Figure 50: a) Stress-strain curves of sintered and conventionally rolled cp-Ti titanium and b) fractured surface of MF³ specimens. Adapted with permission [57].

To assess the suitability of MF³ Ti for electrochemical applications, an electrochemical potential was imposed on the specimens, followed by an anodic sweep of the potential. Measurements were conducted to record the concentration of dissolved Ti. Details on the applied electrochemical protocol and the results of this measurement are published in [57]. The dissolution of the sintered titanium in both the initial and anodic states is significantly lower than that of the conventional Ti film analyzed as a reference. Given the enhanced stability toward dissolution, MF³ Ti can be considered as a promising material for application as bipolar plates on the anode side.

The possibility of processing titanium by the MF³ process was demonstrated by the results obtained in this work. In vacuum of 1×10^{-5} mbar, a relative density of 94.5 % was repeatedly achieved by sintering at 1350 °C for 300 min. The formation of retained α-phase on the surface and in discrete regions within the grain is due to the high oxygen uptake during processing. It is therefore expected that a more homogeneous microstructure and better mechanical performance (in particular ductility) can be achieved when furnaces with a better vacuum of 1×10^{-7} mbar are used.

6.4.4 Nickel-base and cobalt-base superalloys

Superalloys play an important role in high temperature applications, as they have the ability to operate at a high fraction of their absolute melting temperature [171]. Nickel-base alloys are the most frequently used and thus also most intensively studied group of superalloys. Conventional processing comprises casting and forging as well as powder metallurgical processing. Knowledge of the latter processes can be useful for implementation of MF³ processing especially in terms of choosing the appropriate sintering atmosphere and sintering parameters.

To confirm the processability of superalloys in this newly established AM technique, IN 718 was investigated as an example of commercial Nickel-base superalloys. In addition, an experimental Cobalt-base alloy (CoWAlloy3mod) was examined, that was developed at FAU and modified by a GB pinning phase [189].

Processing of IN 718
Results on parameter optimization for MF³ of the Nickel-base Inconel™alloy 718 are presented and discussed in the following section and have already been published [263]. The chemical composition of the used IN 718 powder according to the supplier (Sandvik Osprey Ltd., GB) is given in Table 15. As previous investigations demonstrate a correlation between the processing history of MF³ and the concentrations of C and O in the final part, the contents of these elements are also included.

Microscopical analysis of fracture surfaces of the fabricated filaments proves, that the demanded homogeneous distribution of particles inside the anorganic binder matrix was achieved (Figure 51a). The particles have strongly different sizes, so that a bimodal particle size distribution

can be assumed. However, no measurements were carried out to support this assumption.

Table 15: Chemical composition of IN 718 powder as provided by the supplier.

Ni wt%	Cr wt%	Fe wt%	Nb wt%	Mo wt%	Ti wt%	Al wt%	C wt%	O wt%
51.5	18.8	bal.	4.98	3.1	0.77	0.2	0.015	N.A.

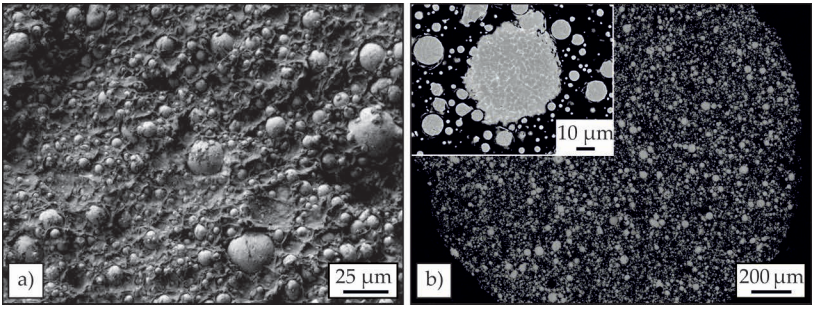

Figure 51: a) Filament fracture surface with dispersed particles embedded into the matrix of the polymeric binder system. b) Cross-section of particles inside the filament. Little amounts of small spherical pores are visible inside the particles. Reprinted with permission [263].

Detailed SEM images in Figure 51b on cross-sections of the powder within the filament show small amounts of internal porosity inside the individual particles. These spherical pores develop during gas atomization of the IN 718 powder and remain inside the material during the whole MF³ processing due to their small size. Image correlation by Image J indicates a powder volume fraction of 50.5 vol% inside the filament, while the measurement of the total binder amount by TGA and reverse calculation of the powder content delivers a value of 53.4 vol%. These analyses indicate that the powder content in the filament is lower than expected, probably due to feeding errors of the co-rotating twin-screw extruder used (ZSE 18 HP-48D Leistritz Extrusionstechnik GmbH, Germany). Despite these deviations of the targeted filament composition, shaping by FFF is possible and the parameters identified for best 3D printing results are given in Table 32 in Appendix B.

The reduced powder content complicates a defect-free debinding, since more polymer must be removed and, at the same time, the quantity and therefore also the proximity of the powder particles is smaller. The stepwise heating program, designed for fast and thorough thermal debinding of previously processed metals, is therefore not applicable in the same way, but the minimum heating rate must be reduced to 0.1 °C min^{-1}. The resulting significantly longer process times have to be accepted to make defect-free binder removal possible for the IN 718 green bodies of low packing density. Successful thermal debinding enables subsequent heating to the sintering temperature at the usual rate of 5 °C min^{-1}. Combined thermal debinding in air, argon or vacuum atmosphere with sintering at 1280 °C for 240 min in vacuum was investigated to evaluate the influence of atmospheric oxygen on the densification behavior.

Table 16: Sintered density of IN 718 after thermal debinding in the indicated atmosphere and sintering in vacuum during 240 min at the indicated temperature.

Debinding atmosphere	Sintering temperature	Density	Relative density
-	°C	g cm^{-3}	%
Air	1280	7.63	92.8
Argon	1260	7.19	87.5
Argon	1280	7.70	93.7
Argon	1300	7.51	91.3
Argon	1320	7.79	94.8
Vacuum	1260	7.73	94.0
Vacuum	1280	7.96	96.8
Vacuum	1300	8.08	98.3
Vacuum	1320	8.18	99.6

The results demonstrate that the final density increases with decreasing pO_2 inside the furnace used for thermal debinding [263]. Thermal debinding in ambient atmosphere is therefore by no means suitable for MF³ of IN 718. Argon gas contributes to maintaining a higher sintering

activity, but a large amount of residual porosity still remains. A summary of sintering tests in Table 16 allows a comparison of the resulting final densities. Further analysis by light and electron microscopy is presented in [263].

Based on these preliminary evaluations of suitable processing atmospheres, vacuum should be used both for thermal debinding and sintering. The microstructure evolution and resulting remaining porosity as a function of the sintering temperature can be observed in SEM images in Figure 52.

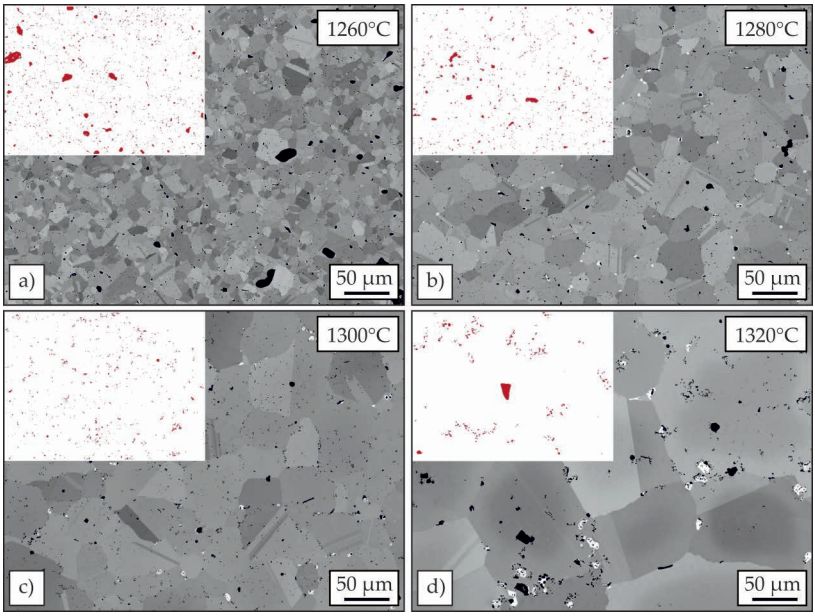

Figure 52: Microstructure evolution after debinding and sintering in vacuum of 1×10^{-4} mbar at a) 1260 °C, b) 1280 °C, c) 1300 °C and d) 1320 °C for 240 min. The small pictures in the upper left corners display the residual porosity marked in red. Reprinted with permission [263].

The small sections in the upper left corners show binarized images that allow a comparison of the residual porosities. While an increased sintering temperature enhances the density up to a limit of 1300 °C, grain growth takes place simultaneously. Starting at 1300 °C (Figure 52c), large

grains are formed, which reduce the mechanical strength. Since the density gain is no longer significant above 1280 °C, but grain growth increases massively at higher temperatures, sintering at 1280 °C for 240 min was the best choice for IN 718. This parameter set allows to reliably achieve relative densities of 96.8 % in pressureless vacuum sintering at levels of 1×10^{-4} mbar. It was used for fabrication of all specimens investigated with regard to precipitation hardening and selected for mechanical property testing.

To make IN 718 suitable for application, it must be heat treated to initiate targeted precipitation of γ" and γ' strengthening phases. Solution annealing is first carried out to dissolve previously formed precipitates and carbides and to produce homogeneous Nb distribution [183]. This is followed by two-step aging to create an ordered γ" / γ' microstructure [180]. TEM analysis in Figure 53 confirms that precipitates are already formed during slow furnace cooling when crossing the respective precipitation windows [264].

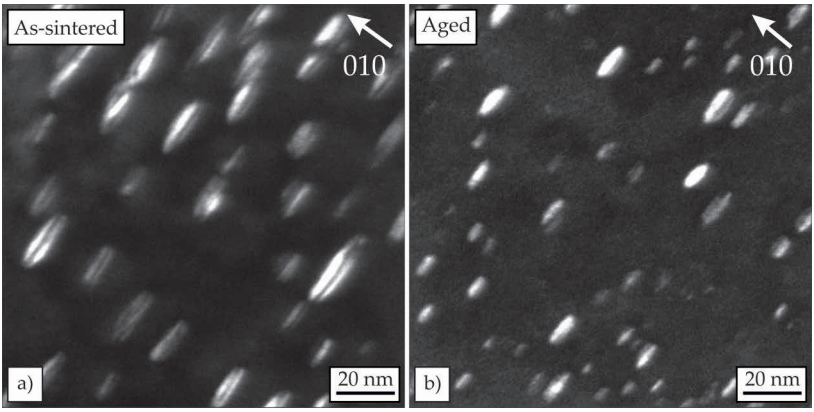

Figure 53: TEM micrographs of a) as-sintered and b) heat-treated IN 718 taken with g = 010 (displaced aperture dark field) in two-beam conditions. a) Precipitation of disk-like γ' / γ" co-precipitates already occurs during slow furnace cooling at 3 °C min^{-1}. b) Finer disk-like γ" and γ' / γ" co-precipitates are achieved after aging. Reprinted with permission [263].

In as-sintered state, mainly γ' / γ" co-precipitates with a disk-like shape are present that lead to a high hardness of 350±45 $HV_{0.2}$. During subsequent solution annealing at 980 °C for 1 h these precipitates are dissolved

resulting in a supersaturated solid solution. Rapid air cooling after solution annealing prohibits the formation of precipitates and results in a much lower hardness of 191±9 $HV_{0.2}$. After two-step aging at 720 °C and 620 °C for 8 h each, a hardness of 446±17 $HV_{0.2}$ indicates successful precipitation, as theses values are similar to those measured for conventional cast and forged IN 718 in identical heat-treated condition (452±9 $HV_{0.2}$).

In a direct comparison of TEM images the heat-treated sample in Figure 53b has finer disk like γ"-precipitates than the as-sintered state. Some γ' / γ" co-precipitates can also be distinguished after aging. The TEM analysis proves that γ' and γ"-precipitates can be formed in MF³ IN 718. Conventional heat treatment comprising solution annealing and two-step aging can successfully dissolve the initially formed precipitates after sintering. It thereby produces a homogeneous Nb distribution, allowing to subsequently form a γ' / γ" microstructure in the two-step aging process. The presence and shape of the precipitates can also be detected by APT measurements as displayed in Figure 54b & c.

APT allows a detailed identification of elemental differences in chemical composition between the distinct phases present in the heat-treated IN 718 material. Concentration profiles in Figure 54a demonstrate a high content of Cr and Fe inside the γ matrix. γ"-precipitates can be identified by enrichment ob Nb, while Al, Ti and Nb show a strong partitioning towards the γ'-phase (Figure 54b). Based on these results, isosurfaces of Al (blue) and Nb (orange) are chosen to visualize γ' and γ"-precipitates inside the γ-matrix (Figure 54c).

Peak deconvolution based on isotopic abundances enables a calculation of the chemical composition of all three identified phases. Values are given in Table 17 and are close to the composition of commercial Alloy 718 that was equally heat-treated [265]. In comparison with the original composition measured by the supplier (given in Table 15), a reduction in the Cr content by 3 at% can be observed. Such a decrease was reported in literature before and is the result of evaporation during vacuum sintering [266]. The MF³ processing history additionally influences the final content of C and O. Spark spectrometry proves that a minor carbon uptake has taken place resulting in a total value of 0.1 at% that is in the range measured after MIM processing [183]. Of the contained carbon, the APT measurements show a very low content of dissolved C, which indicates a localization of C in discrete carbides that can be observed as bright phases in SEM (Figure 52).

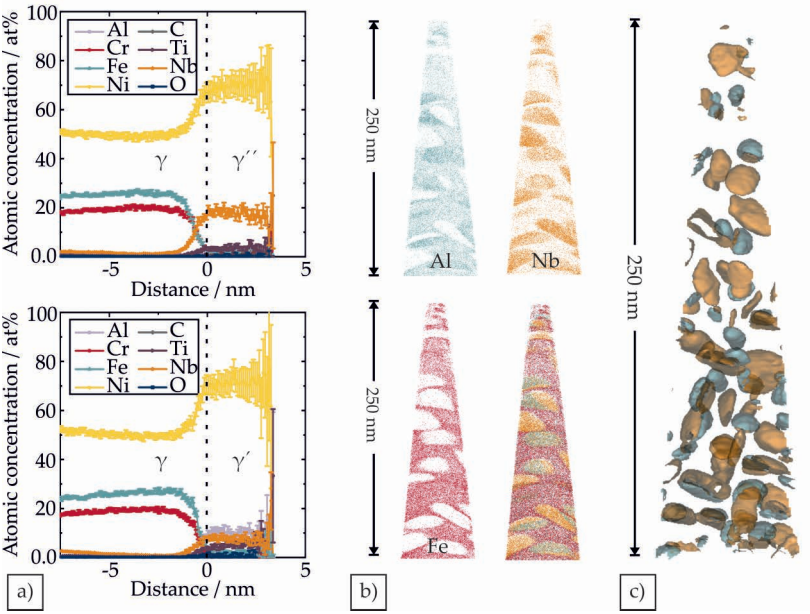

Figure 54: APT data of the sintered (vacuum, 1280 °C, 240 min and heat-treated (air, 980 °C, 1 h; 720 °C, 8 h, 620 °C, 8 h)) sample: a) Proxigrams of elements showing the transition of matrix phase into the γ" and the γ'-phase. b) Ion distribution for the strongly partitioning elements Al, Nb and Fe. c) Isosurfaces of 6.5 at% Al and 11.5 at% Nb representing the γ' and γ"-precipitates respectively. Reprinted with permission [263].

As a high amount of stable carbides can reduce mechanical properties of IN 718, an increased C amount is not desirable [187]. The presented measurements prove that the material manufactured in this work fulfills the specifications of the maximum C content according to data sheets that are in compliance with AMS 5662 and AMS 5664 [267].

Oxide formation on particle surfaces must generally be prevented in MF³ to maintain a high sintering activity during processing. This also applies to IN 718 [76]. Oxygen detected in the APT tip is not localized in a separate oxide phase, but recorded as metal oxides, i.e., Fe-, Al-, Nb-, Ni-, Mo-, and parts of Co-oxides. It emerges from uptake of atmospheric oxygen during heat treatments and most probably also from electropolishing during sample preparation.

Table 17: Chemical composition of the overall sintered and heat-treated compound and of the γ, γ' and γ"-phases as determined by APT. The carbon measurement summarizes atomic C as well as FeC and NbC. Oxygen includes the sum of all metal oxides occurring in the atom probe measurement. These are Fe-, Al-, Nb-, Ni-, Mo-, and parts of Co-Oxides [263].

Phase -	Ni at%	Nb at%	Cr at%	Fe at%	Ti at%	Al at%	Mo at%	Co at%	C at%	O at%
Overall	51.6	3.0	17.1	23.0	0.8	1.2	2.3	0.4	0.02	0.3
γ	47.9 ±0.05	0.6 ±0.1	20.1 ±0.1	27.3 ±0.4	0.2 ±0.0	0.5 ±0.1	2.6 ±0.1	0.2 ±0.0	0.01 ±0.0	0.2 ±0.0
γ'	70.9 ±1.2	7.6 ±0.5	0.4 ±0.1	2.5 ±0.2	6.0 ±0.1	10.6 ±0.8	0.6 ±0.2	0.6 ±0.1	0.06 ±0.0	0.4 ±0.1
γ"	70.2 ±2.6	18.3 ±1.6	1.5 ±0.0	1.8 ±0.0	3.5 ±0.3	0.6 ±0.1	2.1 ±0.2	0.7 ±0.1	0.04 ±0.0	0.4 ±0.1

The results of this presented chemical analyses by APT and spark spectrometry suggest that vacuum debinding and sintering are suitable for MF³ production of IN 718. The sintered material can be heat-treated in the same way as conventionally produced IN 718 and shows the expected precipitation phases, which are important for achieving good mechanical properties.

Properties of IN 718

For an evaluation of room temperature mechanical strength, microtensile testing was chosen, and heat-treated MF³ specimens were measured in direct comparison to conventional cast and wrought and identically heat-treated material. Since the Nickel-base alloy is typically used in high temperature applications, the creep behavior was additionally tested by measurements at 650 °C and 650 MPa, 700 MPa, 750 MPa and 800 MPa compressive stress.

Microtensile testing of heat-treated MF³ specimens reveals a higher strength of 1247.0±139.5 MPa compared to values of 1089.3±62.4 MPa for the cast and wrought material in heat treated state. However the elongation at break is reduced to about a half by MF³ processing, resulting in only 6.6±0.5 %, while the conventional material achieves 12.4±0.8 %. Consistent with the measured strains, the blue graphs in Figure 55a show that almost no macroscopic ductile deformation of the MF³ specimens has taken place.

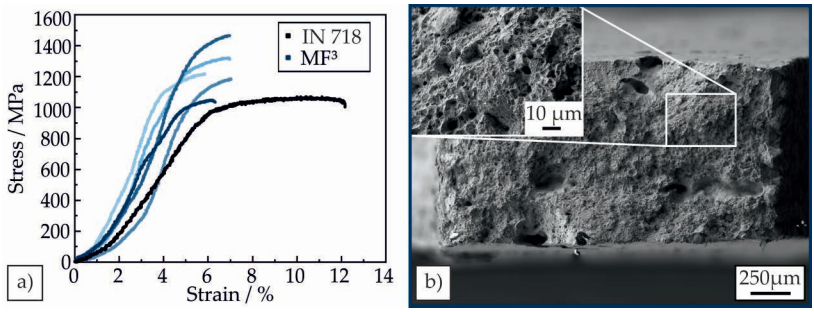

Figure 55: a) Micro-tensile strength of reference (black) and representative sintered and heat-treated MF³ specimen (displayed in different shades of blue for visual clarity). b) The fracture surface of an MF³ specimen contains a few dispersed pores up to 10 µm in size. Intermediate pore free regions show dimples that are characteristics for ductile fracture. Reprinted with permission [263].

The rapid fracture after reaching uniform elongation is due to remaining pores that are elongated under the applied stress as observable in SEM images of fractured surfaces (Figure 55b). The remaining porosity significantly reduces the load-bearing cross-section so that it cannot withstand strong deformations. Since the crack initiating pores are unevenly distributed, the performance of MF³ specimens exhibits large variations. However, the presented measurements prove that optimized debinding and sintering delivers IN 718 material that fulfills the requirements of AMS 5917 (MIM fabrication) [179]. The heat-treatment induced the formation of γ"-precipitates of a size of 26.5±3.6 nm, that matches the optimal value for maximum room temperature yield strength (27.0 nm) [268]. The optimum precipitate size corresponds to the value at which the shear stress required for cutting through the precipitates is equal to the stress required for the dislocations to bow out between the particles.

At a temperature of 650 °C the minimum strain rate of MF³ specimens increases as the applied compressive strength is raised (Figure 56). Compared to cast and wrought material measured in the same creep test setup, the MF³ specimens exhibit a lower minimum creep rate [269–271].

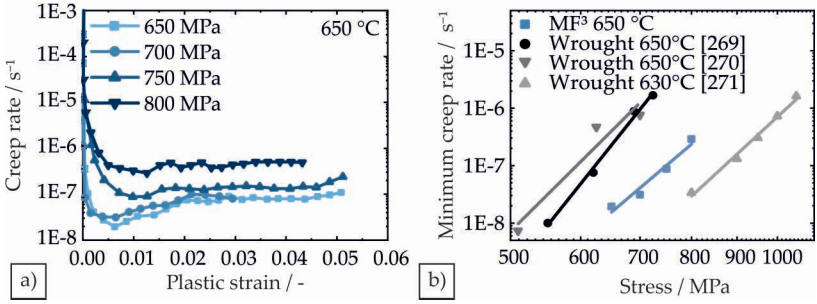

Figure 56: a) Creep behavior of sintered and heat-treated MF³ specimens at 650 °C and applied constant stresses of 650 MPa, 700 MPa, 750 MPa and 800 MPa as a plot of the logarithmic creep rate as a function of plastic strain. b) Norton plot of benchmark wrought IN 718 in tensile [269, 270] and compression creep tests [271] and MF³ material. Reprinted with permission [263].

An evaluation of the Norton plot gives an creep stress exponent of n = 13 for the MF³, which is similar to values for forged IN 718 under tensile creep loading [268–270, 272]. For the investigated temperature and stress range, it is expected that dislocation creep with dislocation slip and glide is the dominant mechanism that critically defines the lifetime during

steady state creep [268, 272]. Diffusion creep along grain boundaries does not significantly contribute to creep deformation at the applied test parameters, especially not for the MF³ specimens because of the large grain size after sintering.

The Norton plot allows a comparison of the creep behavior of the specimens fabricated in this work to conventional material. The lower slope of the linear fit implies an enhanced resistance against creep damage, especially under lower stresses. The superior performance despite the remaining porosity of up to 5 % is a result of the processing history that creates a δ (Ni_3Nb) precipitate-free (Ni_3Nb) microstructure with coarse grains. Without these precipitates, a higher amount of Nb is available for γ" formation, most likely resulting in a higher volume fraction of this strengthening phase [273]. The optimal γ" size for a high creep strength is 23.2 nm, which is slightly smaller than the value for highest room temperature yield strength. This is due to the fact that dislocation climb is activated at high temperature, which leads to self-annihilation and reduces the required stress for dislocation bow out between precipitates [272]. The obtained γ" size of 26.5±3.6 nm is close to this optimum. The absence of the δ-phase, which in the conventional material helps to prevent grain growth at high temperatures, is compensated for in the sintered IN 718 by grain boundary pores and grain boundary carbides with equal effect. In terms of creep behavior, δ-free microstructure with large grains produces creep behavior that exceeds that of the conventional material.

MF³ IN 718 was successfully fabricated by thermal debinding and sintering in vacuum. A relative density of 97 % was reached when sintering at 1280 °C for 240 min and conventional heat-treatment was suitable to induce precipitation of the γ' / γ" strengthening phases. The hardness in the aged condition is similar to conventional heat-treated Nickel-base superalloy IN 718, at a value of 447 $HV_{0.2}$. Microtensile tests demonstrate that, despite the remaining porosity, the mechanical requirements of the AMS 5917 standard were met and the specimens exhibit high strength and slightly reduced ductility [179]. Under compressive stress, creep behavior similar to that of conventional IN 718 is achieved, making the MF³ material particularly promising for high-temperature applications.

Processing of CoWAlloy3mod
The CoWAlloy3 was modified for the purpose of additive manufacturing. The content of carbide-forming elements such as Zr and Hf was reduced to prevent the formation of brittle phases during processing. The new alloy is designated CoWAlloy3mod. With regard to a processability in MF³, the GB-pinning μ-phase can have a positive effect on avoiding grain growth during sintering. Parts of the presented results were obtained in the scope of the Master thesis of Annalena Meermeier [274].

Powder with particle size below 45 μm (corresponding to the sieved fine fraction of EPBF powder) was provided by Nanoval GmbH & Co. KG (Berlin, Germany) with nominal composition as listed in Table 18.

Table 18: Nominal chemical composition of CoWAlloy3mod powder as provided by the supplier.

Co	Ni	Cr	Al	W	Mo	Ti	Ta	C	B	Hf
at%	at%	at%	at%	at%	at%	at%	at%	at%	at%	at%
40.33	32.00	12.00	9.00	5.00	1.00	0.30	0.20	0.08	0.06	0.03

Filament fabrication was successfully performed at MUL using the same binder system that was previously applied for IN 718 and all other materials. A homogeneous particle distribution was achieved at a powder content of 54.5 vol% that was proven by microscopical analysis of filament cross-sections. The SEM images in Figure 57a reveal some microporosity inside the powder particles. These develop during powder fabrication by gas atomization and remain inside the material during the whole processing chain of MF³. It is an additional challenge to remove these small spherical pores during the sintering step.

The particles used in this work are mainly spherical and have a smooth surface, but some are irregularly shaped and contain pores due to deficiencies during powder synthesis (Figure 57b). An improved powder quality can be achieved in the atomization process and should be targeted in the future to enhance the resulting properties of the MF³ material.

Shaping of green bodies was performed by FFF with the parameters given in Table 33 in Appendix B similar to all other metal filaments. Thermal debinding with the step-wise heating program and minimal heating rate of 0.2 °C min^{-1} is suitable for binder removal. Preliminary tests in the

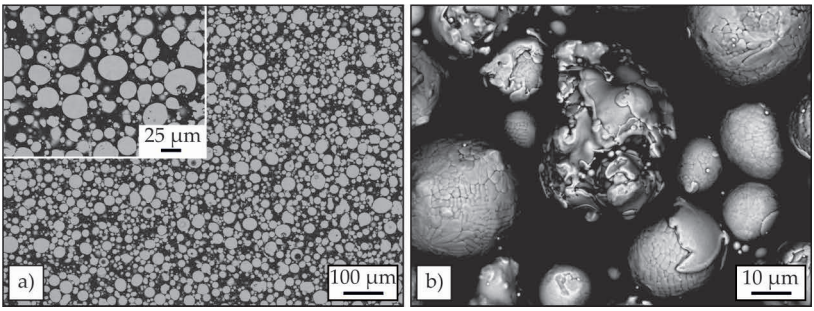

Figure 57: a) Filament with homogeneous particle distribution. Some particles contain spherical pores due to deficiencies during powder atomization. b) The CoWAlloy3mod particles are mainly spherical with smooth particle surface.

different available furnace atmospheres (Ar, Ar+5 % H_2 and vacuum) led to the conclusion that vacuum must be used prevent oxide formation on particle surfaces and successfully initiate sintering densification. Systematic sintering trials in vacuum of 1×10^{-4} mbar were used to identify the temperature-time parameter set for highest final density.

Table 19 shows that the density increases with increasing sintering temperature but, contrary to expectations, decreases with longer sintering time when sintering at 1360 °C. The decreasing density at long sintering duration could indicate degassing of certain alloying elements at higher temperature, however this was not proven analytically. Since a slight loss of shape occurred when sintering at 1360 °C, this temperature is too high and not suitable for sintering of CoWAlloy3.

Based on the density measurements, the sintering temperature of 1355 °C must be applied to achieve a high density without the risk of shape loss. Since grain growth is pronounced when increasing the sintering duration to 240 min, sintering for 180 min at 1355 °C was chosen as the best parameter set.

The sintered CoWAlloy3mod still contains a high amount of residual pores at GBs that are clearly visible in Figure 58a. Many of these pores are still not spherically, indicating the sintering process was not completed. However, significant grain growth has already taken place resulting in a coarse grained microstructure.

Table 19: Sintered density of CoWAlloy3mod parts for thermal debinding and sintering in vacuum at the indicated temperature and time.

Temperature °C	Time min	Density g m^{-3}	Relative density %
1350	180	7.94	89.8
1350	240	8.02	90.7
1350	300	8.38	94.8
1355	180	8.54	96.6
1355	240	8.54	96.6
1355	300	8.42	95.3
1360	180	8.66	98.0
1360	240	8.51	96.3
1360	300	8.38	94.8

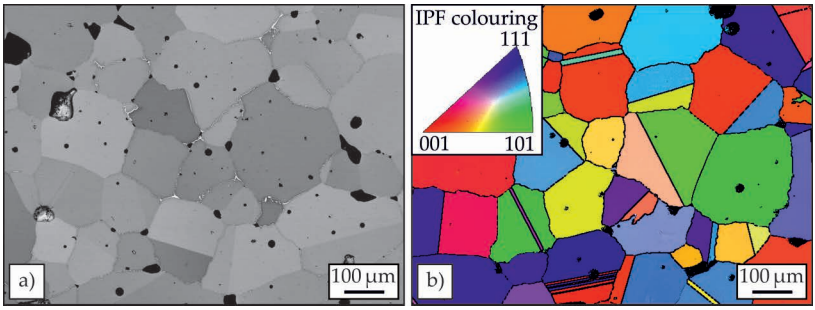

Figure 58: Microstructure of CoWAlloy3mod after sintering at 1350 °C for 180 min: a) Coarse grains with high amount of big grain boundary pores. Some µ-phase can be distinguished at the grain boundaries. b) EBSD measurements visualize the size and shape of the coarse grain structure. The IPF coloring indicates no preferred grain orientation.

EBSD measurements (Figure 58b) allow discrimination between individual grains and were used to measure the grain size of the sintered MF3 material. Based on IPF coloring, no preferred direction of grain orientations can be identified. The median value of 97.1 µm obtained after sintering for 180 min at 1355 °C is significantly higher than the value of 10.1 µm that was measured for the conventionally manufactured CoWAlloy3mod [274].

To make the MF3 material suitable for load-bearing application, samples were subjected to a heat treatment developed to induce formation of strengthening γ'-precipitates. The complete heat-treatment comprises solution annealing at 1250 °C for 3 h with subsequent water quenching, followed by two step aging at 900 °C/4 h and 750 °C/16 h, each concluded by air cooling [189]. The microstructure of the as-sintered, solution annealed and aged state is presented in Figure 59.

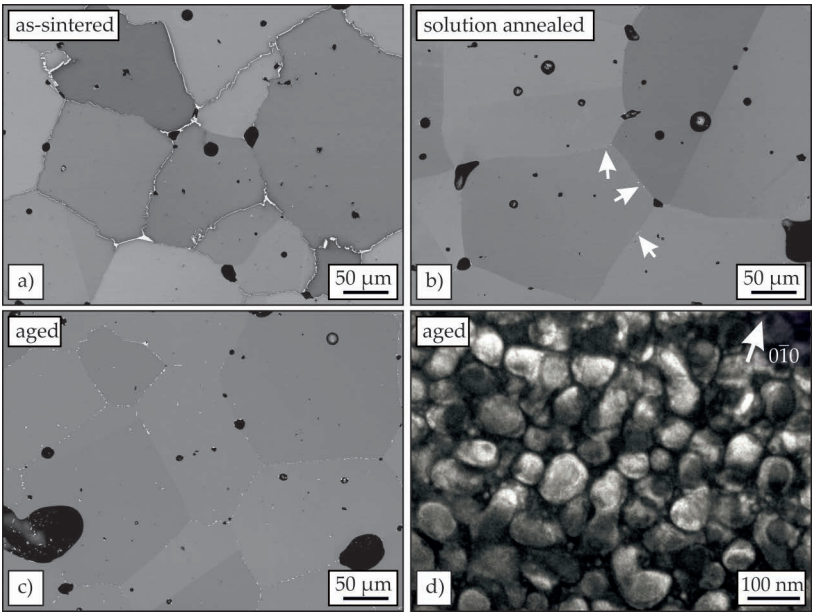

Figure 59: SEM images of MF3 CoWAlloy3mod a) in as-sintered condition, b) after solution annealing and c) in aged condition. d) TEM micrograph of the heat-treated CoWAlloy3mod taken with g = 010 (displaced aperture dark field) in two-beam conditions close to the [001] zone axis.

As previously discussed, the grain size after sintering is coarse, despite the presence of μ-precipitates along grain boundaries, that can be distinguished as a white GB-phase in Figure 59a. This indicates that the pinning effect of the μ-precipitates was not successful in limiting the strong grain growth during sintering.

The applied solution heat treatment causes dissolution of the μ-phase and uniform element distribution. This condition is largely maintained by rapid water cooling, and re-precipitation of μ only occurred in isolated places at grain boundaries (marked by arrows in Figure 59b). The grain size in the annealed condition is similar to that in the as-sintered state, which means that despite solution annealing above the μ-solvus temperature, no significant grain growth has taken place. Although dissolution of the GB-pinning phase occurred during solution annealing, residual elemental segregation, which also impedes grain boundary movement, is the reason for the lack of grain coarsening [275]. In particular, tungsten diffuses very slowly into cobalt [276], which results in W remaining at grain boundaries even after dissolution of the μ-phase and retarding grain boundary motion.

In aged condition, the μ-phase is finely distributed along the grain boundaries (Figure 59c). The strength of co-based superalloys is strongly influenced by the presence and volume content of γ'-precipitates. While no primary γ' is visible in the SEM micrographs, TEM analysis in Figure 59d shows both secondary and much smaller tertiary γ'-precipitates, which have a round shape due to their low lattice mismatch to the γ-matrix. They are less regular than in conventionally produced CoWAlloy3mod, but of similar size and volume fraction [274]. Together with the microstructural changes, the heat treatment causes a change in hardness by inducing the precipitation of strengthening phases. Starting at 348±35 $HV_{0.2}$ after sintering, the hardness is first decreased by dissolution of formed precipitates during solution annealing. The annealed state after water quenching has a hardness of 192±12 $HV_{0.2}$ that is afterwards raised to 364±12 $HV_{0.2}$ by the applied two-step aging. This is close to the measured value of 380±10 $HV_{0.2}$ for the conventionally manufactured CoWAlloy3mod and another proof for the successful formation of γ'-precipitates.

To increase the relative density of the fabricated CoWAlloy3mod, HIP was applied on as-sintered material. Several sintered samples of 87.5 % to 91.3 % relative density were subjected to HIP at 1250 °C under 100 MPa for 30 min to evaluate the influence of external pressure on the densification

of CoWAlloy3mod. The results show that a relative density of 88.4 % ass required to increase the density, as closed pores are necessary for HIP to be effective. In the samples with relative density above 91.1 %, a relative density of 99.1 % was achieved by successful HIP, creating a nearly pore-free microstructure (Figure 60a). In aged condition, grain boundaries of HIPed samples are largely covered by μ-precipitates. However, the EBSD measurements show a large increase in grain size, which can be attributed to enhanced grain growth after dissolution of the μ-phase during the HIP treatment. The additional soaking for 30 min at 1250 °C during HIP corresponds to a prolongation of the solution annealing and effectively causes a removal of the grain boundary pinning phase. The extended soaking at 1250 °C gives more time for diffusion, contributing to a reduction in elemental segregation at grain boundaries. Since the residual pores are additionally removed as a result of densification by HIP, no grain boundary pinning effect remains and unimpeded grain growth occurs during aging. A median grain size of 228.3 μm was measured for the HIPed and aged sample of 99.4 % relative density.

To achieve a smaller grain size, the application of two-step sintering was tested to take advantage of the GB-pinning effect of the μ-phase for limiting grain growth. A pre-sintering step slightly below the μ-solvus temperature (1124 °C) was implemented at 1000 °C for 240 min to generate densification while triggering precipitation of the μ-phase. Together with reducing the sintering time at 1355 °C to 60 min, a relative density of 97.1 % was achieved with a grain size of 67.4 μm measured by EBSD [274]. Further heat treatment with the established program (solution annealing 1250 °C/3 h, water quenching and two-step aging 900 °C/4 h & 750 °C/16 h, air cooling) did not induce grain growth as demonstrated by EBSD images in Figure 60d. The resulting microstructure that is shown in Figure 60c has a significantly smaller grain size than the material sintered directly at 1355 °C presented in Figure 59c. Remaining pores are located both at the grain boundaries and inside the grains. At the same time, a large amount of μ-precipitates can be seen from the bright contrast in the BSE image, especially located at the grain boundaries. In addition, μ-precipitates of block-like morphology are formed inside the grains (red arrow in Figure 60c), partially surrounded by an MC-type carbide (blue arrow in Figure 60c). This structure is caused by nucleation and growth of the μ-phase due to degeneration of the MC-carbide [277]. The different morphology of the μ-precipitates is due to different orientation relationships with the matrix [278].

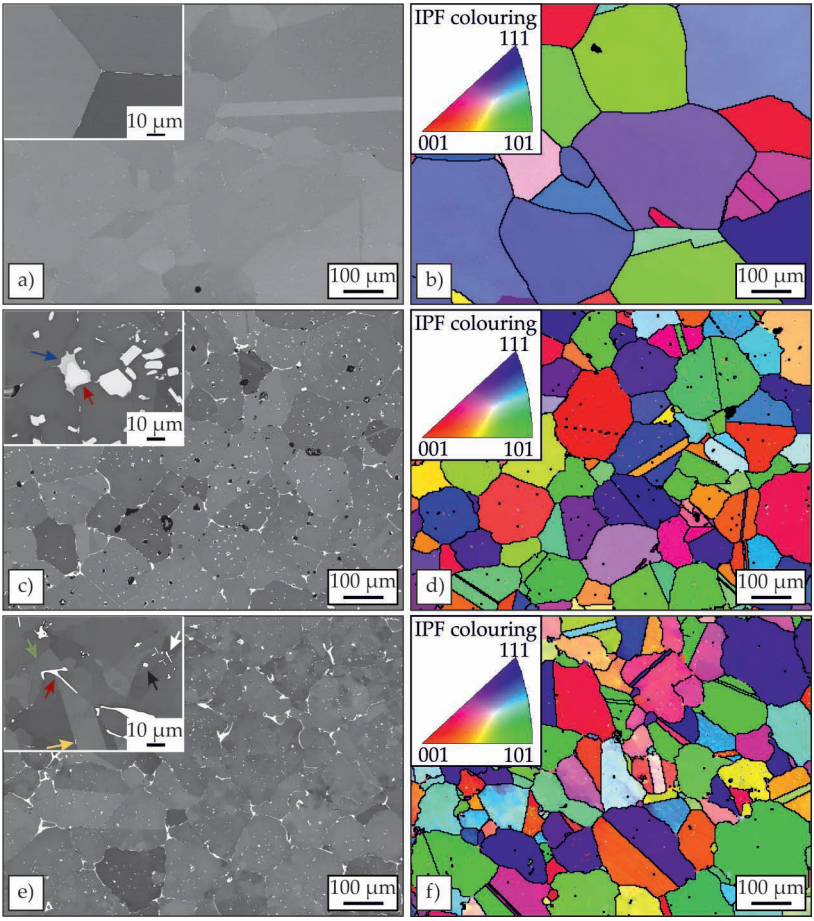

Figure 60: Microstructure of CoWAlloy3mod in aged condition after different sintering programs: a) HIP creates high density with very few small isolated pores. Dispersed µ-phase at GBs can by recognized. b) EBSD images show a large grain size. c) Two-step sintering with pre-sintering step at 1000 °C below the µ-solvus temperature creates a large amount of µ-precipitates. d) The GB-pinning effect of the µ-phase is evident in the resulting smaller grain size. e) Additional HIP after two-step sintering creates a dense microstructure. d) The two-step HIP treatment is successful in creating high densification while maintaining a small grain size.

For an optimized microstructure with high density and small grain size, a combination of the two-step sintering program with subsequent HIP was tested. To limit grain growth during compression at high temperatures, the HIP treatment was performed in two steps: The pressure of 100 MPa was first applied below the μ-solvus temperature, i.e., at 1100 °C for 120 min, and then at 1250 °C for 60 min to improve densification. By this program, a relative density of 99.9 % was achieved. The sintered material was quenched at the end of HIP, delivering samples in solution-annealed condition and only aging needed to be performed afterwards. The aged samples achieve a hardness of 402±20 $HV_{0.2}$, which is slightly higher than the value of 380±10 $HV_{0.2}$ of the conventionally manufactured CoWAlloy3mod. Resulting microstructures have similar grain size to samples without HIP(Figure 60e). EBSD analyses, presented in Figure 60f, demonstrate that the arbitrary grain orientation is preserved and deliver a median grain size of 59.7 μm.

Note should be taken of the different morphology of the μ-phase that can be observed at higher magnification in Figure 60e. The precipitation occurred partly in form of large, irregularly shaped phases at the grain boundaries (red arrow), but partly also in a fine pearl string-like distribution along the grain boundaries (green arrow). Occasionally, μ-precipitates are found attached to twin grain boundaries (yellow arrow). If precipitation of the μ-phase occurs inside the grain, both a block-like (black arrow) and a rod-like morphology (white arrow) are formed. The different morphologies are the result of different crystallographic orientation relationships with the matrix [278]. The 90° angle between the rod-shaped precipitates (white arrow) shows very well the strict adherence to this orientation relation [279].

Properties of CoWAlloy3mod

The effect of relative density and grain size on mechanical properties was evaluated in compression tests, conducted at RT and at a temperature of 650 °C and 750 °C. A direct comparison made in Figure 61 reveals that only the two-stage sintered and HIPed specimen with high density and at the same time small grain size achieves mechanical properties in the range of the conventionally manufactured material. All other processing methods result in a significantly lower yield strength, with HIP for increased density having a positive effect on mechanical properties only at RT.

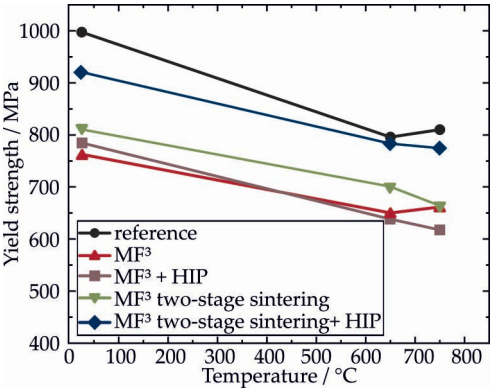

Figure 61: Comparison of yield strength measured for aged CoWAlloy3 specimens in compression tests at room temperature and at elevated temperatures.

At elevated temperatures the large grain size causes a decrease in yield strength, even below the strength of the solely sintered material with higher remaining porosity. The low compressive strength of MF³ CoWAlloy3mod is therefore attributed to the large grain size and the resulting loss of Hall-Petch strengthening. This result is consistent with results for the base alloy CoWAlloy3 found by Lisa Freund, who calculated more than half of the strength resulting from the Hall-Petch effect [189]. A decrease in grain size as achieved by pre-sintering at 1000 °C contributes to higher yield strength at room temperature, however the performance decreases to levels of the conventionally sintered material at 650 °C. For high-temperature applications, such as those planned for the co-base superalloy, HIP must therefore be added to the developed sintering program with pre-sintering step in order to achieve a high relative density at small grain size.

Further mechanical characterization was obtained by micro-tensile testing of specimens prepared by the optimized temperature program with two-stage sintering and HIP. Stress-strain curves in Figure 62a show a decrease in mechanical strength of MF³ specimens by approx. 300 MPa compared to the reference material to a value of 787.2±46.7 MPa. Again, a strong deviation between the behavior of the individual specimens is measured, while the results of the conventional ones are very close to each other, delivering a tensile strength of 1097.6±8.0 MPa. The elongation at break of 31.1±1.7 % is similar to that of conventionally manufactured CoWAlloy3mod with a value of 29.7±2.2 % [274].

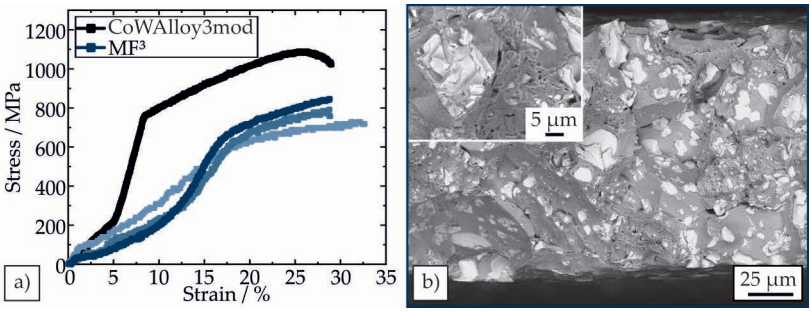

Figure 62: a) Stress-strain curves of micro-tensile tests. The CoWAlloy3mod MF³ samples were fabricated by two-stage sintering and HIP. b) The corresponding fracture surface of the MF³ specimens is penetrated by brittle precipitates.

The fracture surface of the MF³ specimen presented in Figure 62b is permeated by a high amount of brittle fractured precipitates, and only small honeycomb-like areas remain next to the cleavage-like fracture regions. The results of these micro-tensile tests show that the precipitation of brittle phases must be reduced to improve the ductility of MF³ CoWAlloy3mod. This can be achieved by an optimized heat treatment, but in that case the associated grain growth must be limited. Apart from this, carbon uptake during thermal debinding is another factor contributing to increased precipitation, that needs to be limited in the future by using a furnace with debinding trap for more thorough removal of binder degradation products.

The presented results on MF³ manufacturing of CoWAlloy3 prove the possibility of additive manufacturing of co-base superalloys by the newly developed technology. Due to the complex microstruture of this alloy, an additional pre-sintering step was needed to limit grain growth during sintering. Since a significant strength contribution in CoWAlloy3 originates from Hall-Petch hardening, it is crucial to keep the grain size small for good mechanical performance. Additional HIP contributed to enhanced densification and when applied in a two-step program with predensification for 120 min at 1100 °C and 60 min at 1250 °C a fine grained microstructure is maintained parallel to pore elimination. The resulting specimens have a yield strength in compression tests that is reduced by 100 MPa compared to conventional CoWAlloy3 at room temperature, while the micro-tensile strength lies 300 MPa below the reference value.

Despite the high amount of brittle phases, a high ductility with an elongation at break of 31.1±1.7 % was achieved. The developed sintering program with pre-sintering stage and two-step HIP treatment is based on these results considered successful in enabling MF³ fabrication of CoWAlloy3mod with mechanical properties close to conventionally fabricated material at room temperature.

6.4.5 Copper

Processing of Copper
UltraFine®Copper-MIM powder (Carpenter Powder Products Inc., RI, USA) with D_{50} = 14.55 µm and D_{90} = 29.69 µm was used in the scope of this work. The chemical analysis as provided by the supplier is shown in Table 20.

Table 20: Composition of copper powder as provided by the supplier.

Cu wt%	Fe wt%	Ag wt%	Sn wt%	Zn wt%	C wt%	S wt%	O wt%	N wt%
bal.	0.01	0.001	n/d	n/d	0.001	n/d	0.05	0.0001

Prior to filament processing, the powder morphology was investigated with SEM and optical size analysis (Camsizer XT, Retsch Technology, Germany) was performed to determine the particle size distribution. Results of this powder analysis are shown in Figure 63 and prove that agglomerations can be nearly completely prevented.

Preparation of copper filaments was successfully performed at MUL, implying a powder content of 55 vol% was achieved while conserving homogenous particle distribution. During printing, nozzle temperatures were reduced to 250 °C as the high thermal conductivity of copper particles induces faster melting of the binder polymer [235, 236]. Further parameters are almost the same as used for other metal filled filaments (Table 34 in Appendix B). The previously established two-step debinding can be identically applied for removal of organic binder components.

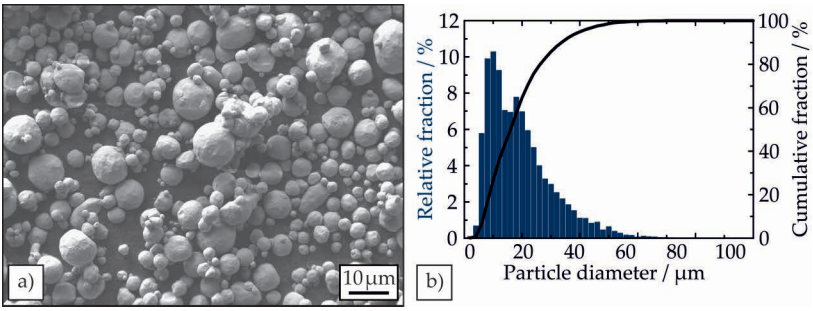

Figure 63: a) Loose copper powders with spherical morphology in SEM. b) Particle size distribution measured by optical size analysis demonstrate the abscence of stable agglomerates.

Processing at elevated temperatures in vacuum at a level of 1×10^{-4} mbar and below cannot induce relevant sintering activity in densely packed copper powder bodies. After sintering at 1060 °C for 600 min the particles are still loose and no sinter neck formation or relevant densification occurred (Figure 64a). The lack of sintering activity is due to the formation of continuous oxide layers on the surface of the copper particles. These oxide shells, that are visible in Figure 64b, hinder sintering to a large extend and only few sintering necks have formed despite sintering close to the melting temperature.

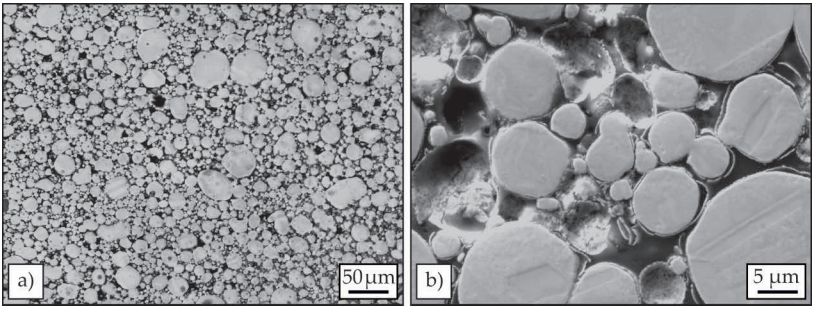

Figure 64: a) Cross-sectional SEM image of copper bodies sintered at 1060 °C for 600 min in vacuum show that particles remain loose after sintering and no densification was achieved. b) Continuous oxide formation on the surface of copper particles sintered at 1050 °C for 90 min in vacuum of 1×10^{-4} mbar [280].

All samples processed in vacuum remain highly porous with interconnected open porosity due to adsorption of atmospheric oxygen content remaining inside the furnace [280]. As a result to this strong oxide formation, vacuum processed samples do not exceed a relative density of 81.1 %. Argon processing, that was investigated in the bachelor thesis of Maximilian Marschall, did not produce a significant increase in density either [281].

To increase the sintered density and enhance the performance of MF³ copper parts, an oxide reducing atmosphere (95 % Ar + 5 % H_2) was used. As previously deduced for 316L, the glas flow inside the tube furnace allows accelerated thermal debinding, leading to a halving of total debinding duration. Several sintering temperatures and sintering times were tested to evaluate optimal parameters in terms of highest final density. As shown in table 21, high temperatures and long sintering times are needed to increase densification.

Table 21: Density of MF³ copper after sintering in 95 % Ar + 5 % H_2 at the indicated temperature and time.

Temperature °C	Time min	Density g m^{-3}	Relative density %
1050	120	7.76	86.7
1060	120	7.94	88.6
1070	120	7.40	82.6
1080	120	7.73	86.3
1060	120	7.70	85.9
1060	300	7.77	86.8
1060	600	8.15	91.0
1060	3000	8.15	91.0

SEM images of the test series conducted for evaluation of the sintering time show a microstructure in the intermediate stage of the sintering process, in accordance with the measured density. After 120 min, the remaining pores are interconnected in a channel-like manner (Figure 65a).

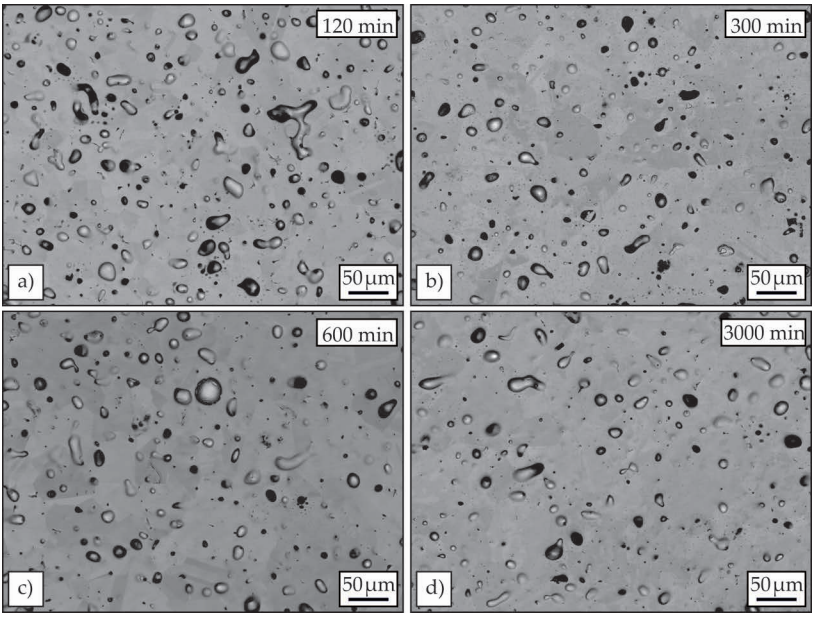

Figure 65: Microstructure of MF³ copper samples sintered at 1060 °C for a) 120 min, b) 300 min, c) 600 min and d) 3000 min.

At longer sintering times, the proportion of elongated pores decreases and closed spherical pores appear more frequently (Figure 65b & c). However, the proportion of residual porosity is still 9.0 % even after 3000 min of sintering (Figure 65d), so that the sintering process cannot be considered complete.

Properties of Copper

Since copper is used in most applications due to its good electrical conductivity, the MF³ samples were tested with respect to this property. The results show a strong correlation between relative density and electrical conductivity (Figure 37b), indicating a strong decrease in conductivity across the pores. In the best case, a value of 74.5 % IACS of pure copper was obtained for the sample with 89.1 % relative density [281].

Mechanical properties of MF³ copper were evaluated for samples sintered at 1050 °C for 3000 min. All specimens had a relative density of 89.4 %. Despite the high amount of residual porosity, the copper specimens

show high ductility, which even exceeds the elongation at break of the reference material (Figure 66a). On the other hand, the tensile strength of MF³ specimens is significantly reduced to 88.0±11.5 MPa compared to 132.3±7.5 MPa. The high remaining porosity causes strong variations in the stress-strain curve due to the breakup of individual pores during testing, resulting in stress dips.

The fracture surface in Figure 66b demonstrates the high proportion of pores. In agreement with the ductile fracture behavior, a dimpled fracture surface can be identified, which results from the growth of voids up to coalescence [282].

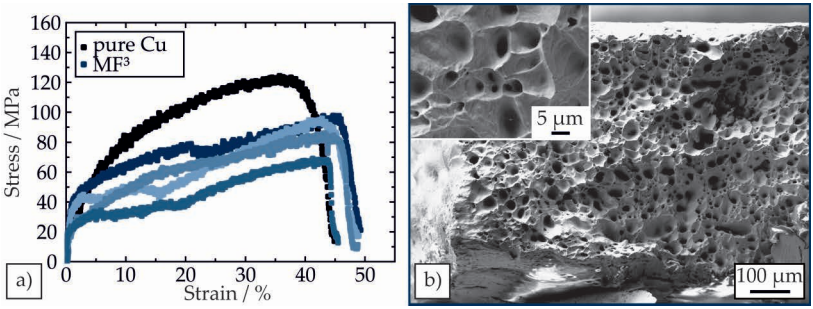

Figure 66: a) Stress-strain curves of pure copper and sintered MF³ copper. Cracking of individual pores during ongoing testing produces an irregular strength curve. b) Fracture surface of MF³ specimen after micro-tensile testing.

In conclusion, a reducing atmosphere of Ar + 5 % H_2 was necessary to limit oxide formation during processing of copper to the extent that a relative density of 91.0 % was achieved. Despite the remaining porosity, the specimens exhibit high ductility with an elongation at break of 48.2±1.4 % at a tensile strength of 88.0±11.5 MPa.

6.5 Multi-material additive manufacturing

A major advantage of MF³ over other additive processes is the possibility of manufacturing multi-material components. The use of the same binder system allows the combination of different materials inside the same component during the printing process [211]. For example, by using multiple nozzles, differently filled filaments can be extruded in parallel. The challenge in MF³ manufacturing of laminates lies in achieving high

densification during co-sintering of materials with very different sintering kinetics and sintering start temperature [214].

In the scope of this work, different material combinations were chosen for first feasibility studies and as a starting point for further investigations. The combination of 316L with IN 718 was selected after the studies of the individual materials delivered similar sintering parameters. Additionally, Copper - 316L and combinations of 316L and copper with Al_2O_3 were chosen due to their differing thermal properties and thus high interest for functional applications.

In a second part of this chapter the fabrication of complex geometries by using sacrificial ceramic support structures was investigated as a modification of dual-material manufacturing in section 6.5.2.

6.5.1 Manufacturing of composites

Bi-metallic laminates and metal-ceramic composites were printed by FFF with the Panowin F1 printer with custom-built dual nozzle setup. The first layer of the secondly extruded material was placed 0.1 mm downwards to promote interface adhesion. Since the same binder system was used in the different filaments, a good bonding in the green body was achieved for all material combinations. Laminates of 316L-IN 718 as well as 316L-Cu and Al_2O_3-Cu were printed with 3 mm height of each phase, resulting in a total sample thickness of 6 mm. Figure 67 shows printed and compressed 316L-Cu composites in green state. Light microscopy images of the interface (Figure 67a) show that good bonding and dense particle packing between the different materials was achieved. This observation is confirmed by BSE images in Figure 67b, that demonstrate the close proximity of copper and steel particles.

The green bodies of the other material combinations, including the composites with ceramics, were also printed with good interfacial quality.

Solvent debinding was performed identically to the single-phase components. Due to the different densities of the incorporated powders, the success of the solvent extraction can no longer be determined from the obtained mass loss. To ensure complete TPE removal, immersion times were set to 10 days based on experience gained from preliminary studies.

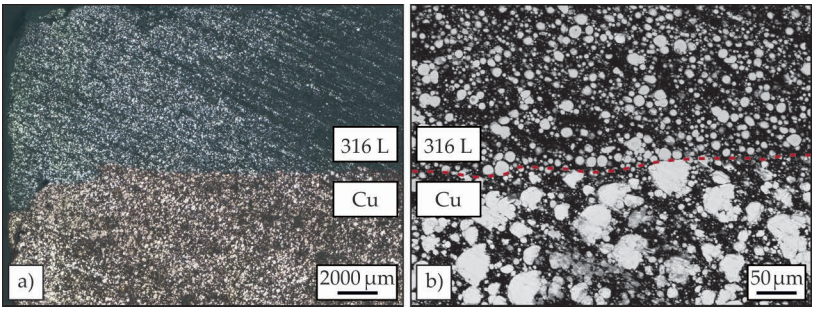

Figure 67: a) Light microscopy of the printed 316L - copper laminates in green state proves that particles are densely packed along the interface. b) SEM images confirm the close proximity of the different powder particles.

The election of a suitable furnace atmosphere for thermal debinding was based on the more oxidation-susceptible component to avoid sinter-inhibiting oxide formation in both phases. Composites containing copper were processed in forming gas and vacuum was used for all other samples. The developed step-wise heating program with minimum heating rates of 0.2 °C min^{-1} in vacuum and 0.5 °C min^{-1} in Ar+5 %H_2 atmosphere was successfully applied for thermal debinding.

Sintering of the composites exhibits a major challenge due to the differing thermal properties of the combined materials. The combination of 316L and IN 718 was chosen due to their similar sintering behavior. Based on experimental investigations on the single materials, sintering at 1350 °C for 240 h in vacuum was applied. The laminate was thermally debound with a critical heating rate of 0.1 °C min^{-1} to account for the reduced powder content of the IN 718 filament, discussed in chapter 6.4.4. With this heating rate, it was possible to produce a crack- and bubble-free composite.

The comparison of 316L-IN 718 laminates in green state and after sintering, in Figure 68 demonstrates that very good densification can be achieved if the optimum sintering parameters for both alloys are used. The process-induced big pore at the interface that can be recognized in Figure 68b is a result of systematic printing defects, due to deficiencies in the layer bonding of the first IN 718 layer on the previously deposited 316L strands. This porosity can be avoided by optimization of the FFF

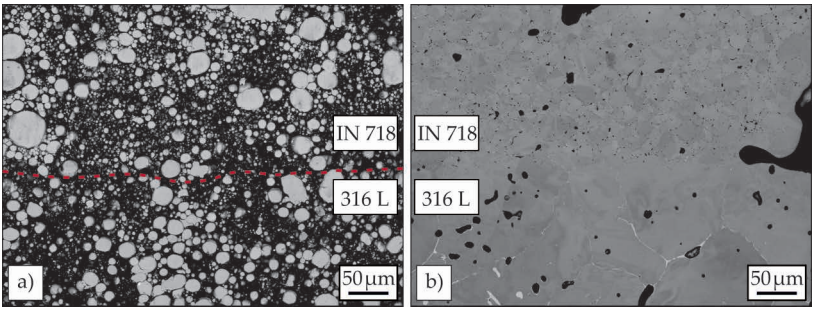

Figure 68: Laminate of 316L - IN 718 a) in green state and b) after sintering at 1350 °C in vacuum.

process. Other remaining pores inside the bulk of the two phases are a result of pressureless sintering, and their removal is more difficult.

A detailed analysis of the individual phases shows that the 316L in the laminate exhibits a coarse-grained microstructure with grain boundary carbides, as is also formed in single-material MF³ (Figure 69a). Likewise, a similar microstructure was obtained for IN 718 as in the separate production by MF³. Only few isolated larger pores are visible in Figure 69c, which are probably a result of printing deficiencies during dual-material FFF. Apart from that, the residual porosity and the grain size are very similar to those of the samples fabricated in chapter 6.4.4. Based on the microstructure analysis, the formation of an interfacial bonding can be considered successful, although no mechanical tests were performed to evaluate the interface strength.

With other laminates, densification is more challenging because the sintering temperatures are very different, resulting in one phase having too little sintering activity. This is the case for 316L -Al_2O_3 composites, where the ceramic should ideally be sintered at temperatures higher than the melting temperature of the steel. At the sintering temperature of 1350 °C identified as optimal for 316L, incomplete densification of the ceramic phase is to be expected. In experimental trials, the mismatch caused cracks that emerged in the ceramic due to different shrinkage resulting from uneven densification of the two combined materials (Figure 69f). Despite this crack formation that occurred parallel to the interface at a distance of approx. 50 µm, a good bonding between 316L and Al_2O_3 was achieved (Figure 69e). The steel was successfully sintered to high

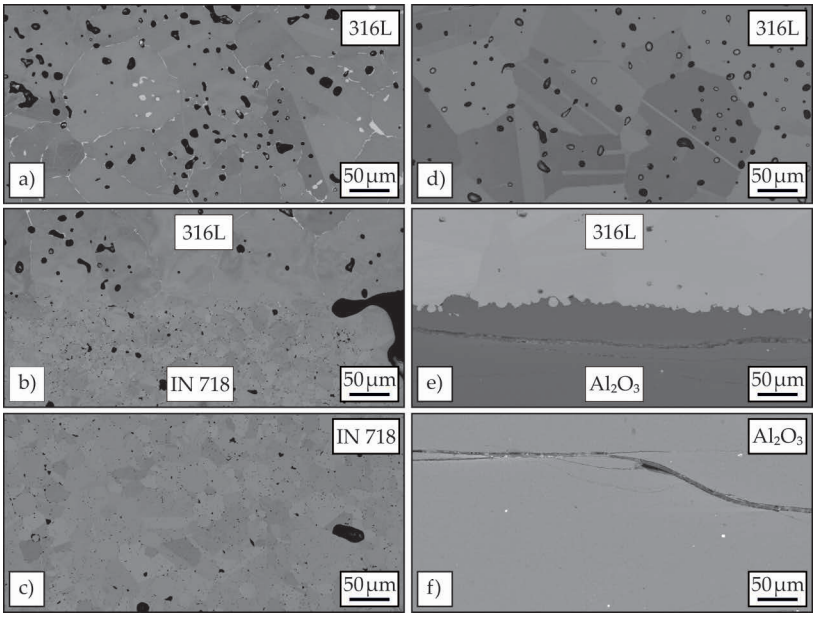

Figure 69: Sintered 316L laminates: Interfaces of b) 316L - IN 718 and e) 316L - Al_2O_3 and SEM images of the respective single phases in these laminates: a) & d) 316L, c) IN 718 and f) Al_2O_3.

relative density, and the ceramic also attained a high relative density in areas not affected by cracking. The fact that densification of the ceramic takes place despite the low sintering temperature is due to the small grain size of the ceramic particles, which provides high sintering activity even at temperatures below the optimum value [140]. For a good quality of steel-ceramic laminates and to avoid cracking due to shrinkage differences, the powder content of the ceramic should be adjusted in future tests. If the shrinkage of the ceramic layer is matched to the shrinkage of the steel, a good layer bond can be achieved without generating internal stresses and resulting cracking.

Another example of such material combinations is 316L-Cu, where the sintering temperature of copper lies 300 °C below the value suitable for steel. In consequence, the 316L exhibits little sintering activity at the applied 1060 °C and light microscopy reveals a high amount of elongated pores resulting from improper adhesion of neighboring layers (Figure 70a

& e). Additionally, different shrinkage of the two layers was observed on macroscopic level for this combination.

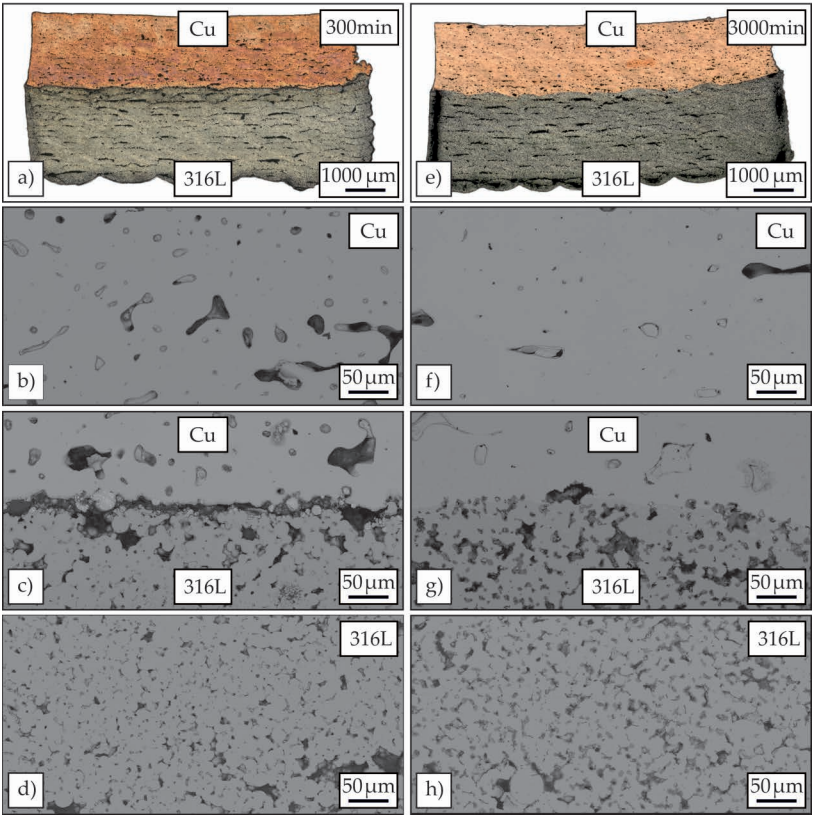

Figure 70: Sintered 316L-Cu composites sintered at 1075 °C a-d) for 300 min, e-h) 3000 min.

In order to nevertheless create densification in the 316L phase, long sintering durations up to 3000 min were experimentally investigated. Figure 70 shows SEM images of the different composite regions and the interface in dependence of the sintering dwell time. Even after extended sintering, the 316L phase in this composite only reaches the intermediate stage of the sintering process, still containing a high proportion of interconnected tubular pores (Figure 70d & h). Densification of copper is enhanced by prolonged sintering, and when sintered for 3000 min the copper phase

achieves similar densification to single-phase sintering with both elongated and closed porosity. In terms of interface bonding, the influence of longer sintering time is decisively noticeable and good bonding is achieved after 3000 min, while a clear separation of the two phases is visible after 300 min in Figure 70c. Nevertheless, both manufactured composites are stable and withstand handling and cutting.

The most difficult material combination investigated in this work is Cu-Al_2O_3, due to their very different melting temperatures. Nevertheless, an initially stable composite was produced by sintering for 3000 min at 1060 °C. However, during the subsequent mechanical preparation by cutting and grinding, some parts of the ceramic phase fractured in a brittle manner. This happened especially in near-interface regions, as can be detected in Figure 71a, and is due to insufficient densification at the low sintering temperature.

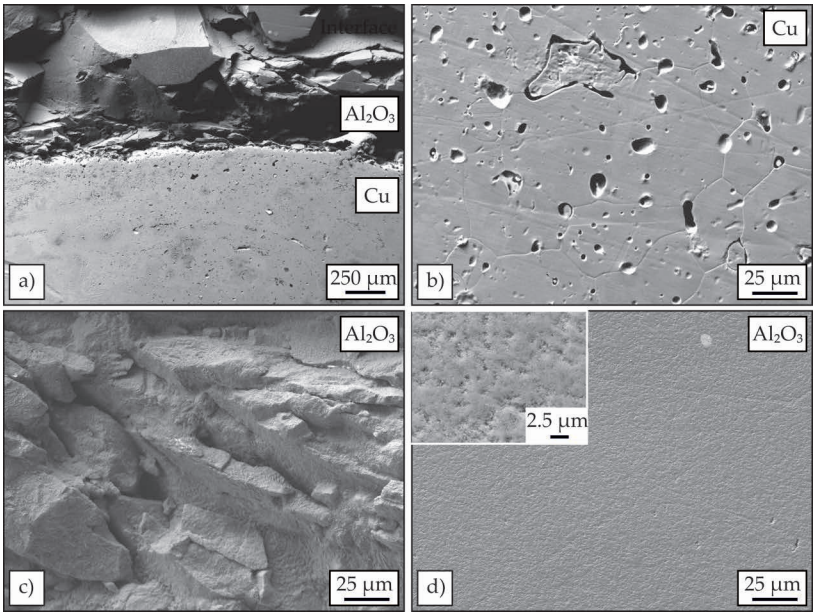

Figure 71: Sintered Cu-Al_2O_3 composites: a) Interface with improperly sintered and after mechanical preparation fractured Al_2O_3. b) SEM images of the Cu phase and comparison of c) fractured Al_2O_3 and d) densified Al_2O_3 regions.

The brittle fracture mode that results in a fissured fracture surface is confirmed at higher magnification in Figure 71c. In other areas of the Al_2O_3, however, high densification was obtained, which can be verified in Figure 71d. The copper phase of the composite uniformly reaches the final density achievable in pressureless sintering (Figure 71b). The formation of a $CuAlO_2$ phase along the interface that was reported to promote a toughening of the interphase in sintering of Cu-Al_2O_3 composites was not observed [283].

Based on these results, the combination of copper and Al_2O_3 into a composite can not be considered successful. However, the successfully sintered areas within the ceramic are promising, so that further investigations should be carried out at different sintering parameters in order to enable additive manufacturing of this material combination, which is very attractive for functional applications.

Independently of the differing densification and shrinkage behaviors, a form-fit joint was formed in all material combinations as a result of the printing process. Due to the layered structure and the overfilling of the individual printing layers, a very high surface roughness is present after the printing process. This creates an interlock between the different materials, resulting in a form fit. Material combinations with very different sintering behavior, in which a material bond cannot be created at the interface, nevertheless exhibit interface strength that creates a connected component.

The results of the very first trials of multi-material MF³ obtained in this work are very promising, especially if the combined materials have similar sintering temperatures. Further investigations should be carried out to match the sintering and shrinkage behavior of the two materials involved and to enable the production of defect-free composites. It is expected that sufficient interfacial strength can be generated to enable functional applications. For the sintered phases, relative densities above 90 % are achievable or were already obtained.

6.5.2 Manufacturing of complex geometries

The manufacturing of complex geometries by MF³ processing requires the use of supporting elements for overhanging structures. Ceramics, which have a significantly higher sintering temperature than the metal powders used for the component, are particularly suitable for use as support material, if a dual-material set-up is available. The application of a ceramic interlayer for separable support structures is the subject of a patent [226]. For a feasibility study within the scope of this work, Al_2O_3 filament was used exemplary to build the support structure. An easily available and inexpensive powder with coarse particle size (D_{50} = 34.4 µm, D_{90} = 47.2 µm) was used. In addition to the coarse particle size, the irregular particle shape limits the achievable packing density. The filaments used for printing of the support structures have a powder content of 50 vol%. The lower powder fraction of the filament is advantageous for the intended use as a support material for several reasons: On the one hand, it was demonstrated in chapter 6.3 for Ampersint 1557.02 that the lower green density reduces the final density after sintering. This facilitates the removal of the support structure with reduced force. On the other hand, the lower green density causes increased shrinkage already in early sintering stages and can thus compensate for shrinkage differences between the shrinking metallic component and the non-densified ceramic support structure [74]. During processing, the irregular particle shape enhances the stability of structures by creating increased friction. The use of coarse powder particles additionally reduces the sintering activity of the Al_2O_3. This improves easy removability after the sintering process.

The support material was applied to test the feasability of manufacturing complex geometries in the MF³. The 316L, investigated in chapter 6.4.2, was chosen as component material. The focus of the performed tests is on the generation of a sufficient supporting effect by the ceramic structure during the entire process. SA residue-free removal at the end of the process route should be possible. Strongly differing shrinkage, which the different sintering behavior can entail, must be avoided to prevent internal stresses. Some of the presented results were obtained as part of the bachelor thesis of Yannick Utz [284].

The geometry of the support structure must be designed to fit the complex shape of the part. Since in dual FFF each nozzle is assigned its own model, the construction of a separate body is necessary. During printing, both

materials are extruded simultaneously with their respective optimum parameters and the green body consisting of the component geometry and support structure is built up layer by layer. Figure 72 shows results of printing tests for some representative overhang angles. The ceramic filament has a slightly darker shade of gray than the steel filament, so that a visual distinction between the two different materials is possible.

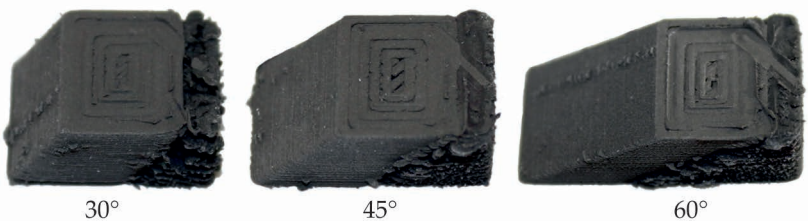

Figure 72: Printed 316L overhangs of 30°, 45° and 60° supported by ceramic support of coarse Al_2O_3.

In solvent debinding, a complete extraction of the contained TPE content was achieved without endangering the stability of the sample. For thermal debinding, removal of the ceramic structure at the end of the debinding process and before sintering was tested for an overhang angle of 45° (Figure 73a). After applying the established pre-sintering program with soaking for 90 min at 750 °C, the metallic geometry already has sufficient self-contained strength. However, no firm bond is formed between the component and the support structure until this point, and the two bodies can be easily separated. The ceramic remains stable during the debinding process due to the spattered particle shape that results in a high level of friction between the particles. Thereby it provides sufficient support to stabilize overhanging regions. However, the temperatures are not high enough for sintering of the ceramic. After removing the ceramic structure, the metallic brown body was sintered without additional support. No shape loss nor distortion occurred during the subsequent densification. Supporting of overhanging structures until the end of the thermal debinding process is by this test proven sufficient and the use of support structures can be dispensed with in the further course of the process.

The quality of the fabricated overhanging surface was investigated using light and electron microscopy. Notably, the interface of the steel sample that was in contact with the ceramic support shows a greatly increased

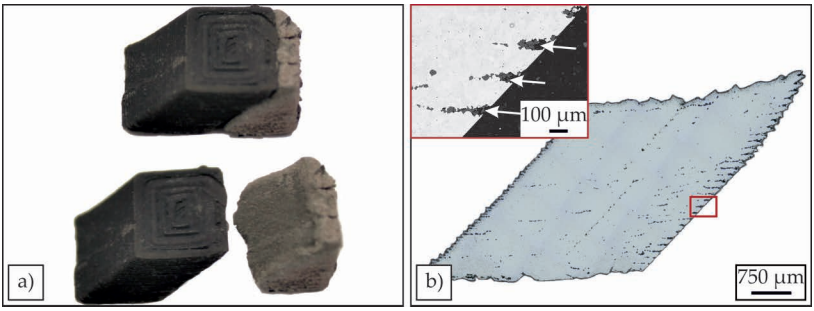

Figure 73: a) Overhang angle of 45° after thermal debinding and pre-sintering. The completely debound metallic brown body remains stable after removal of the ceramic support structure. b) Characterization of the overhanging surface: The roughness emerging from green body FFF is increased by imprinted ceramic particles (marked by white arrows in the BSE image in the upper left corner) that prevent shrinkage during sintering of the 316L structure.

roughness after the sintering process (Figure 73b). On the one hand, this is due to the layer by layer built-up in the course of green body FFF, which leads to a stepped character of the interface. On the other hand, BSE imaging shows that imprinted ceramic particles that were not completely removed after debinding. They prevent shrinkage of the steel along this interface and thereby increase the effect of the layered structure. This effect can be reduced by optimizing the FFF parameters, which will be discussed later in this section.

The removal of the ceramic support structure before the final sintering process requires particularly careful handling as the densification of the component has not yet been completed in this state. Single powder particles that can be detached during separation of the component and the support are respiratory due to their small size and thus additional precautions for work safety are required. It is beneficial to remove the support structure after the sintering process has been completed. In this state, the ceramic particles are pre-sintered and fragments that arise when the support structure is mechanically detached can no longer pose a threat. To investigate this alternative strategy, the formerly presented overhanging angle of 45° with all-ceramic support structure was directly sintered for 120 min at 1350 °C after thermal debinding. During sintering, the shrinkage of the two different materials is strongly dissimilar. The 316L was densified to a large extent and experienced a linear shrinkage

of 15 %. In contrast, almost no shrinkage of the ceramic occurred owing to its less pronounced sintering activity at the selected temperature of 1350 °C. As both materials are in direct surface contact during processing, such strong differences in shrinkage create mutual tensions. These can lead to distortion or cracking of the steel component, that was in the performed tests observed in some corners of the sintered part.

One strategy to relieve tension caused by shrinkage mismatch is a reduced usage of ceramics. Instead of the all-ceramic structure, the support can be provided by the same metal used in the complex component. The ceramic is in this case just applied as an interlayer to prevent sintering activities between the component and the support structure. The CAD design adapted for this strategy of component and support structure made of 316L and an Al_2O_3 interlayer can be implemented by dual FFF as shown in Figure 74. It allows additive shaping with the known printing parameters. A thickness of 0.8 mm for the ceramic interlayer corresponds to the nozzle diameter used for the extrusion of ceramic filaments and results in printing of a single ceramic strand. It is suitable to preserve the stability of the overhanging region during processing and prevent distortion. A removal of the support structure, however, was not possible, as an inseparable bond between the component and support structure was formed. As distinguishable in BSE images of the printed interface in Figure 74b, building up of a complete ceramic separating layer between the two steel components was not achieved. The printed ceramic layers are separated from each other by steel particles that were deposited by smearing of the nozzle. The created continuous 316L layers form a direct bonding between the component and the main support structure, that prevents easy removal after sintering.

To overcome this problem and prevent the steel particles from smearing into the intermediate ceramic layer, a z-lift of the extruder was implemented for traveling movements during the printing process. This produces a shift of the nozzle by 5 mm in positive z-direction if crossing of the ceramic layer is necessary when changing between the component and the support structure. The increased distance of the nozzle to the topmost printed layer serves to avoid crossing of the nozzle through already deposited material during travel movements. This measure was supplemented by a redesign of the support structure and the insertion of a small gap between the component and the ceramic separating layer as sketched in Figure 74c.

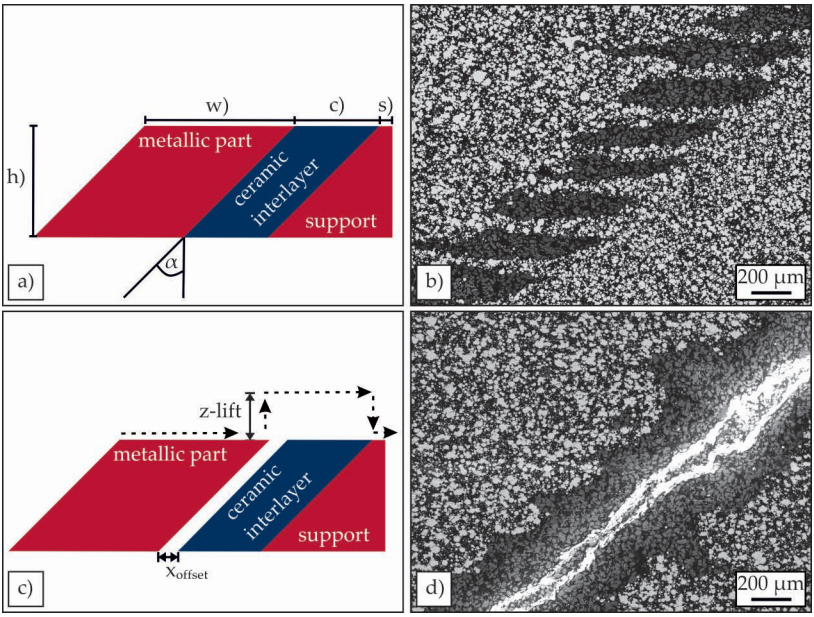

Figure 74: a) Constructive design of the ceramic interlayer between the steel part and the support structure of the same metal. b) BSE image of a printed green body with ceramic interlayer. Continuous strands of steel particles can be recognized as a result of smearing of protruding filament during the printing process. c) Implementation of a constructive 0.3 mm offset between component and support structure and of a 5 mm z-lift during travel movements to avoid smearing of metallic particles into the ceramic interlayer. d) BSE images prove the successful printing of a continuous ceramic layer.

An offset of 0.3 mm inserted on the component side can create a sharp separation at the corresponding interface. In combination with a broadening of the ceramic layer to a thickness of 1.5 mm and the previously described extruder z-lift, a continuous ceramic interface can be printed between component and support structure and verified by BSE (Figure 74d) in green body state. After completion of sintering, the ceramic layer and with it the support structure can be easily separated from the component.

A 90° round structure was chosen to demonstrate the applicability of the developed supports for fabrication of arbitrary complex geometries. The combination of a design offset of 0.3 mm and a 5 mm nozzle z-lift during

printing allows FFF of a continuous ceramic interface between component and support. Afterwards, debinding and sintering can be performed using parameters for single-metal MF³ while the support structure provides mechanical integrity of overhanging regions. A separating ceramic layer of at least 1.5 mm thickness allows easy removal of the supporting structure after sintering.

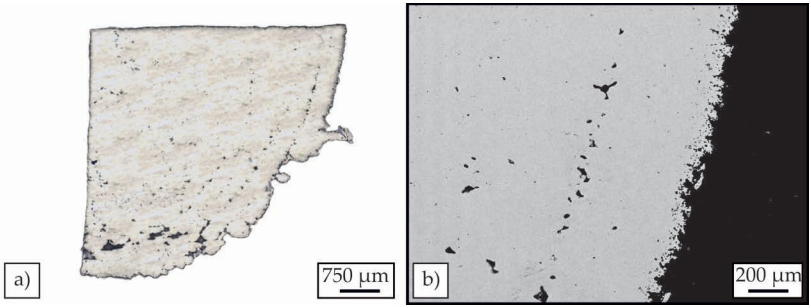

Figure 75: a) Overview of a round structure fabricated with a ceramic interlayer printed with an offset of 0.3 mm and 5 mm nozzle z-lift. b) A low surface roughness was achieved.

The produced part with a round surface is shown in cross-section in Figure 75a. Defects in the interior of the component can be clearly identified as systematic printing defects and can be eliminated in the future by optimizing the printing parameters and, in particular, the layer bonding of the first layers. No stress induced defects are observed. Figure 75b shows that by optimizing the printing strategy, it was possible to produce a good surface quality with significantly lower roughness compared to Figure 73b.

The results of the print strategy optimization proves that in MF³ the use of a thin ceramic interlayer between the component and the support structure is well suited for manufacturing of complex components. Taking advantage of the low sintering activity of the ceramic allows easy removal of the support structures, and costly post-processing is only necessary if particularly good surface quality and low roughness are required.

7 Summary and conclusions

In this final chapter, an evaluation of the potential of the developed MF³ process is made. First, the critical parameters are summarized and requirements for successful MF³ processing are derived. The second part evaluates the necessary measures for the processing of selected metals. A best-functioning strategy is elaborated for each investigated material.

A proof of concept of multi-material MF³ for fabrication of composites or complex geometries is presented in section 7.3. Section 7.4 finally contains a conclusion and further requirements that should be addressed before the process can be reliably used for additive manufacturing of metals.

7.1 General MF³ processing

The basis of successful MF³ production is the additive manufacturing of a solid green body, with uniformly high packing density in every spatial direction and free of printing-induced voids. In the FFF of the highly-filled filaments, the shaping of suitable parts is favored by a high infill density, low layer height, high printing temperature and slow printing speed. Green bodies manufactured according to this concept can subsequently be sintered to relative densities above 90 %. Higher final densities are achieved if the particle packing is increased by additional compression in the green state. As demonstrated in this work, this can be realized with readily available equipment such as a hot mounting press. Ideally, the targeted isostatic compression is generated by using liquids or gases, which increases the homogeneity of the component compared to the method shown.

Removal of the polymeric binder system that serves for shaping is realized in two stages, in which the main binder component is first extracted by using a solvent. In this step, interconnected pore channels are formed inside the component, which serve as transport routes during the subsequent thermal debinding. By this step, the mechanical strength of the parts is reduced only to the extent that dimensional stability is not affected. Since the attack of the solvent progresses from the surface to the interior, a strong dependence of the required immersion time on the thickness of the samples was observed.

Thermal debinding is the most critical step along the process chain and can lead to complete destruction of the part. Binder components that are decomposed during heating must be removed via the previously formed pore channels. The evaporation of the decomposition products is the time-dominating process and the decomposition rate, which is controlled by the heating rate, must be adjusted correspondingly. If the decomposition rate is too fast, pressure builds up in the component, resulting in the formation of defects in the form of bubbles and cracks. In parallel, rearrangements of the particles must be generated during thermal debinding in order to create a denser particle packing and thus higher friction between the particles. This provides particle adhesion that ensures sufficient initial strength to maintain dimensional stability. The heating rates that can be realized depend on the wall thickness, which constitutes the length of the evaporation path. The time for evaporation is largely dependent on the furnace atmosphere. To prevent oxide formation before the following sintering step, an atmosphere of low pO_2 must be selected, although oxygen accelerates binder decomposition and would be beneficial during debinding. For cylindrical samples of 6 mm height evaluated in this work, a rate of 0.5 °C min^{-1} was suitable when debinding in gas atmosphere, while vacuum debinding was only successful at reduced rates of 0.2 °C min^{-1}. The critical temperature range in which the decomposition of the binder takes place was determined by means of TGA and is between 170 °C and 450 °C. The minimum heating rate is used in this temperature range in a stepwise heating program. By rapid heating below this critical temperature range, the total duration of thermal debinding was reduced to 24 h. The thermal debinding step is completed by a soaking time of 60 min at 450 °C, which provides sufficient time for the removal of all organic components.

Thermal debinding passes directly into a pre-sintering process in which the mechanical stability of the parts is restored by initiating sinter neck formation. Sufficient sintering activity was generated at 750 °C in a vacuum atmosphere for most investigated metals. For copper, oxidation of the particle surfaces must be counteracted in an atmosphere containing hydrogen. Sufficient strength of pre-sintered copper parts was only achieved at 900 °C. At the determined temperatures, a soaking time of 90 min produces sufficient mechanical strength that allows stable handling of the samples. Debound and pre-sintered parts have a relative density between 85 % and 90 %.

Sintering serves for final densification to high relative densities and makes the manufactured parts suitable for application. High temperatures and long sintering times contribute to increased final densities, while grain growth must be limited with respect to mechanical strength. A trade-off must be found for each single material, to adjust the microstructure in the best possible way. According to the studies of several different metals, sintering times of 120 min to 300 min have proven beneficial if oxidation can be controlled. Maintaining sintering activity by preventing the formation of oxides induced by atmospheric oxygen is the essential requirement for successful sintering. With the exception of copper, a vacuum atmosphere with low oxygen partial pressure is suitable for the investigated metals in order to produce high sintering activity and high final density. Alternative sintering in an argon atmosphere results in significantly higher residual porosity. The fact that vacuum delays the evaporation of the binder decomposition products and prolongs the duration of thermal debinding must be accepted. Copper, which has a very strong tendency to oxide formation, can only be consolidated to relative densities of 90 % if atmospheres containing hydrogen provide oxide reduction and restore sintering activity. If HIP is used, as exemplary tested for CoWAlloy3mod, a relative density of 99 % and more is achieved. HIP is therefore a good option when the targeted application requires high density or excellent mechanical properties.

In summary, the optimum conditions for thermal debinding and sintering are opposing and a best trade-off must be found in the choice of the most suitable atmosphere. The focus is on achieving the highest possible density by limiting oxygen uptake. At the same time, a fine microstructure is targeted by appropriate choice of sintering parameters. The MF³ process can then be used for additive manufacturing of metallic components with relative densities of 94 % to 97 %, suitable for functional applications in the medium mechanical stress range. At the same time, the selective fabrication of porous structures is possible, which opens up new applications, e.g. as gas diffusion barriers.

7.2 MF³ processing of selected metals

The applicability of the MF³ process for the production of various metals was demonstrated in this work. In order to achieve optimum parameters in each case, it is crucial to make an individual choice of atmosphere, sintering temperature and sintering time. The special requirements for the respective materials as well as the process parameters that produce the best results are summarized in the following chapter.

7.2.1 Steels

Steels were successfully manufactured by MF³ and sintered to relative density above 95 %. Massive grain growth occurs at high sintering temperatures, yet high strength (approx. 80 % of the reference value) is still achieved with ductility reduced to about 80 % of the elongation at break of a conventional material. Maintaining the carbon content is crucial for high mechanical strength, since C, as an important alloying element, determines the final microstructure. To avoid decarburization, a vacuum atmosphere must be used during thermal debinding and sintering. This is particularly evident in the case of the hot work tool steel Ampersint 1557.02. The most suitable sintering parameters and resulting mechanical properties of the investigated steels 316L and Ampersint 1557.02 are summarized in Table 22.

Table 22: Results on optimal MF³ sintering parameters and achieved mechanical properties for the investigated steels.

Parameter	Sintering temperature	Sintering time	Vickers hardness	Micro-tensile strength	Elongation at break
-	°C	min	$HV_{0.2}$	MPa	%
316L	1350	300	133 ±89	411.6 ±58.7	33.7 ±7.8
Ampersint 1557.02	1350	300	782 ±22	1316.8 ±106.7	21.4 ±1.5

In detail, 316L sintered in vacuum develops a coarse microstructure with $Cr_{23}C_6$ formation at grain boundaries as a result of the long sintering

at 1350 °C. Due to carbon uptake during thermal debinding, a mixed fracture mode with ductile and brittle components is developed, leading to a reduction of the strain at break.

The resulting microstructure of Ampersint 1557.02 is more fine-grained in comparison. Given the high carbon content after thermal debinding and sintering in vacuum, a martensitic microstructure with some amount of retained austenite is formed even after slow furnace cooling. For further hardening, a protective foil must be used to prevent decarburization and the soaking time for austenitization is to be kept short for the same reason. In case of the small component volumes investigated in this work a soaking time of 30 min in the pre-heated was considered sufficient. Further tempering can be conducted in ambient atmosphere, as the temperature is low enough to prevent decarburization. The final Q & T specimen achieves a tensile strength above 1300 MPa at medium ductility with elongation at break around 20 %.

7.2.2 Titanium

Cp-Ti titanium was successfully fabricated in MF³ by using vacuum both during thermal debinding and sintering. Relative sintered density of 94.5 % was achieved when combining green body compression with optimized sintering at 1350 °C for 300 min. As Ti is highly susceptible to oxidation it is indispensable to conduct all processing steps in atmospheres of very low pO_2, i.e. vacuum levels of 1×10^{-5} mbar or below are required. Nevertheless an α-case surface layer of up to 50 µm in depth is formed on the samples. The final parts exhibit a multi-phase microstructure, with the α-matrix containing distributed regions of retained α-phases. These are formed due to increased C and O concentrations as a result of the processing history and, like the surface α-case layer, exhibit strongly increased hardness. Lamellar α + β GB phases develop due to Fe enrichment at GBs if the Fe concentration surpasses 0.5 wt%. This is common with sintered Ti if the original powder contains Fe impurities, since at elevated temperatures Fe diffusion along the grain boundaries is accelerated. The solid solution strengthening by impurity elements contributes to an increased tensile strength of MF³ titanium despite the high amount of remaining pores. These cause premature failure when reaching uniform elongation, leading to a reduced elongation at break compared to conventional cp-Ti titanium. A summary of mechanical properties of the sintered Ti specimens is given in Table 23.

Table 23: Results on optimal MF³ sintering parameters and achieved mechanical properties of titanium.

Parameter	Sintering temperature	Sintering time	Vickers hardness	Micro-tensile strength	Elongation at break
-	°C	min	$HV_{0.2}$	MPa	%
Ti	1350	300	320 ±58	325.4 ±10.3	18.4 ±1.0

The achieved mechanical properties make the MF³ Ti suitable for non load-bearing applications. Such are electrochemical applications that seem particularly suitable due to the high resistance of sintered Ti to electrochemical dissolution. If better vacuum levels in the range of 1×10^{-7} mbar were available, a lower uptake of impurities with consequently more uniform microstructure and higher ductility is to be expected.

7.2.3 Nickel-base and cobalt-base superalloys

Nickel- and cobalt-base superalloys can be successfully fabricated in MF³ and established heat treatments initiate precipitation of strengthening phases. While IN 718 can tolerate a larger grain size after sintering due to these strengthening phases, in the case of the investigated CoWAlloy3mod measures have to be taken to maintain a fine microstructure for achieving high mechanical strength and ductility. After sintering, both superalloys exhibit a homogeneous microstructure in which neither concentration variations nor preferential grain orientations are present.

In detail, the findings on processing of superalloys can be summarized as follows: In case of IN 718 additional difficulties were encountered during debinding, as the initial filament powder content of approx. 52 % was lower than targeted. By decreasing the minimal heating rate, applied between 170 °C and 450 °C, to 0.1 °C min^{-1}, defect free binder removal was realized. Sintering for 300 min at 1280 °C was identified as a best trade-off for achieving high density while suppressing major grain growth. The as-sintered parts have a relative density of 96.2±1.7 % and, due to slow furnace cooling (at 3 °C min^{-1}) after sintering, already contain γ'/γ"

co-precipitates. As a result, IN 718 in as sintered state already exhibits high hardness of 350±45 $HV_{0.2}$. For superior mechanical properties, a heat treatment established for MIM IN 718 was applied that consists of solution annealing followed by two-step aging to induce formation of precipitates. Hardness measurements after the individual steps prove the success of this treatment that leads to the targeted γ'/γ" microstructure. The mechanical strength of MF³ IN 718 is similar to reference values, while the ductility is reduced by the remaining porosity. An overview of processing parameters and resulting room temperature properties is provided in Table 24. The high temperature creep behavior of the sintered and heat-treated IN 718 was evaluated at 650 °C under compressive stress between 650 MPa to 800 MPa. A comparison to wrought material tested under tensile load demonstrates high creep resistance of the MF³ specimens with lower minimum creep rate. Dislocation creep was identified as the dominant creep mechanism and the γ" size of 27±4 nm optimally contributes to a high creep strength.

Table 24: Results on optimal MF³ sintering parameters and achieved mechanical properties of superalloys in aged condition: IN 718 after solution annealing at 980 °C, 1 h with air cooling and two-step aging at 720 °C/8 h and 620 °C/8 h. CoWAlloy3mod after presintering at 1000 °C for 240 min, sintering at 1350 °C for 60 min, and two-stage HIP for 120 min at 1100 °C and 60 min at 1250 °C followed by aging at 900 °C/4 h and 750 °C/16 h, each concluded by air cooling.

Parameter	Sintering temperature	Sintering time	Vickers hardness	Micro-tensile strength	Elongation at break
-	°C	min	$HV_{0.2}$	MPa	%
IN 718	1280	240	446 ±17	1247.0 ±139.5	6.6 ±0.5
CoW Alloy3 mod	1350	60	402 ±20	787.2 ±46.7	31.1 ±1.7

MF³ of the co-base superalloy CoWAlloy3mod resulted more complex, as a small grain size must be maintained during sintering to achieve high mechanical strength. To limit grain growth an additional soaking at 1000 °C was integrated into the temperature program prior to reaching the sintering temperature, in order to induce the formation of the GB

pinning μ-phase. A comparison of as-sintered CoWAlloy3mod with and without the additional soaking step demonstrates the increased amount of μ-precipitates along grain boundaries, that contributes to achieving a finer microstructure at similar relative density. Additional HIP served for removal of remaining pores. When applied in a two-step program with 120 min at 1100 °C and 60 min at 1250 °C, grain coarsening during HIP can be prevented. In aged condition specimens reach a mechanical strength of 700 MPa, which is 300 MPa below the strength of the conventionally manufactured material.

The excellent mechanical performance that was achieved in this work demonstrates MF³ as a suitable process for additive manufacturing of IN 718. Despite the low powder content in the original filament, a high relative density was consistently achieved. The duration of the debinding step can be reduced in the future if the commonly used powder content of 55 % is reached. The identified sintering program is suitable to create good densification while limiting grain growth. For the application, high mechanical strength is achieved by the established heat treatment of solution annealing and two-step aging to form the γ'/γ" microstructure characteristic of IN 718.

For CoWAlloy3mod, a suitable sintering program was identified which, in addition to a high degree of densification, preserves a small grain size. To enhance the mechanical properties, a two-stage HIP was additionally developed, delivering a relative density above 99 %. In aged condition, the specimens achieve a slightly reduced strength with very good ductility, which is similar to conventionally manufactured material.

7.2.4 Copper

MF³ processing of copper resulted challenging as densification during sintering was only achieved by using reducing atmosphere during thermal debinding and sintering. When forming gas containing 5 % of H_2 was applied, the relative density reached 90 %. Long sintering times of 3000 min at 1050 °C were chosen in pressureless sintering. The final copper parts have reduced tensile strength due to the high residual porosity. Nevertheless, they exhibit excellent ductility, with elongations at break higher than those of the conventionally manufactured material. The best sintering parameters as based on the outcome of this work with their resulting mechanical properties are presented in Table 25.

Table 25: Results on optimal MF³ sintering parameters and achieved mechanical properties of copper.

Parameter	Sintering temperature	Sintering time	Micro-tensile strength	Elongation at break
-	°C	min	MPa	%
Cu	1050	3000	88.0 ±11.5	48.2 ±1.4

Given the high amount of remaining pores even after prolonged sintering, the MF³ with pressureless sintering cannot be recommended for additive manufacturing of copper parts. For functional, non-load-bearing applications, the manufactured samples may be suitable, although the electrical conductivity is reduced to 75 % IACS due to the residual porosity and impurities. The results of this work therefore suggest that an alternative sintering method should be investigated, for example application of HIP, to produce copper with relative density of at least 95 %. Additionally, the use of a different copper powder with higher chemical purity can enhance sintering. If the targeted densification can be produced, MF³ is a promising method for additive manufacturing of pure copper that can overcome the high costs and required additional measures of beam-based processes.

7.3 Multi-material MF³ processing

A major advantage of MF³ compared to conventional additive manufacturing processes is the capability of multi-material fabrication. A customized FFF printer was used in this work to test several material combinations for fabrication of metal laminates as well as metal-ceramic compounds. Additionally, the dual set-up was investigated for manufacturing of complex parts by using ceramics in the support structure to allow an easy removal at the end of the processing chain.

Although these efforts should be considered as preliminary studies, promising results were obtained in fabricating composites with sufficient interfacial strength to withstand handling and cutting. Interface

adhesion is enhanced by stair-case effects of the printed layers that contribute to an interlocking connection between the different phases. Of the investigated compounds, the interface strength was most critical for the combination of 316L and Cu. Besides the interface, both individual phases must reach a certain densification level of at least 90 % to ensure a basic mechanical strength. In case of the Cu-Al_2O_3 combination, this was not achieved for the ceramic phase, that broke under low mechanical stress. Best results were obtained when combining materials of similar sintering kinetics as are 316L-IN 718 and 316L-Al_2O_3. In both cases, high densification was obtained for the bulk of the two phases. The use of the same powder content in the original filaments resulted in similar shrinkage and allowed a good interface adhesion.

For manufacturing of complex geometries, an interlocking interface was not targeted. To achieve a smooth interface free of remaining ceramic particles of the support structure, some constructive adjustments were evaluated. A combination of implementing a z-lift during printing and incorporating an offset between the part and the support structure proved best to avoid smearing between adjacent materials during filament extrusion. An all-ceramic support structure allowed the fabrication of complex overhangs, but the different shrinkage of the two phases induced internal stresses that lead to cracking of the part. This was overcome by applying the ceramic only as a separating layer between the component and the support, which are both made of the same material and exhibit the same shrinkage behavior. An interlayer width of 1.5 mm together with a constructive offset of 0.3 mm between the metal and the ceramic and a nozzle z-lift of 5 mm when crossing along the interface proved to be suitable for fabrication of an overhanging round surface.

Dual-material MF³ was demonstrated as a versatile option for the production of composites with good interfacial adhesion and for the use of easily removable supports to fabricate complex geometries. If the use of more than one material is already considered in the planning and the original filaments are optimized for the targeted application, better results in terms of achievable densities and matching shrinkage behavior can be achieved. Under this condition, the MF³ process is promising for multi-material AM and can become interesting for a wide range of applications.

7.4 Conclusions

Based on the outcome of this thesis, I would like to point out some requirements that must be met for successful MF³ processing. The crucial task is the specific choice of suitable furnace atmospheres and sintering parameters for each processed material. For shaping and solvent debinding, processing of different materials can be realized with largely the same settings by using the same binder system in all filaments. For successful sintering, the furnace atmosphere must be individually matched to the material from the start of thermal debinding. Prevention of oxide formation and, associated with the removal of the binder, the control of the carbon content are crucial for achieving the targeted microstructure. The chemical purity of fabricated parts can be enhanced by thermal debinding in furnaces designed for this purpose, which are equipped with a debinding trap. Such equipment ensures removal of the binder decomposition products from the furnace atmosphere and reduces contamination of component surfaces. Further improvements in mechanical and functional properties can be achieved by using separate furnaces for debinding and sintering. In the present work, it was proven that pre-sintered samples have sufficient mechanical strength to be transferred from one furnace to another. Sintering can then be realized in a clean atmosphere where no residues from the debinding process affect the parts. In addition, sintering under external pressure (HIP), which is commonly applied in MIM, can increase the relative density to more than 99 %. When using existing equipment, this step slightly adds to the total costs, especially since it can be combined with subsequent heat treatments, as demonstrated for the co-based superalloy.

In this work, I was able to show that a wide range of metals can be additively manufactured with MF³ using low-cost equipment. The sometimes large variations in the results of the executed experiments can be reduced by using more sophisticated equipment, and a reliable and reproducible process chain can be established. Filament-based shaping enables easy and safe 3D printing, with the ability of using fine powder fractions that are left over from conventional PBF processes. The MF³ process provides a high utilization of the invested powder material. Support structures for complex geometries can be manufactured from a different, less expensive material than the actual component by using the multi-material option.

At the same time, manufacturing of composites is possible. Thanks to polymer-based shaping of green bodies and sinter-based consolidation, even combinations of metal and ceramic can be produced. At this point, the MF³ process has an advantage over the established powder bed processes, where the joining of different materials into one component is difficult to realize.

Considering all obtained results, I advise to investigate the MF³ in production-scale equipment in order to explore possible applications. By providing thorough debinding and a clean sintering atmosphere, dense components with high mechanical strength can be produced. These can also compete with parts fabricated in powder bed processes, requiring significantly lower investment costs for powder raw materials and equipment.

Appendix

A Debinding of metal injection molding components

Table 26: Debinding methods for different binder systems [69].

Primary binder -	Secondary binder -	Primary debinding method -	Debinding rate mm h^{-1}
Wax-based			
Paraffin wax	Polypropylene	Heptane	1.5
Synthetic wax	Polypropylene	Perchloro-ethylene	2
Water-soluble			
Polyehtylglycol	Polypropylene	Water	0.3
Polyehtylglycol	Polyacetal	Water	0.5
Catamold			
Polyacetal	Polyethylene	Nitric acid catalyst	1.5

Table 27: Thermal properties of different binder systems [60].

Binder -	Melting temperature °C	Decomposition temperature °C
Polypropylene	158	330-460
Stearic acid	60	190-280
High density polyethylene	132	420-550
Paraffin wax	58	230-400

B Parameters for FFF printing of specific powder-filled filaments

Table 28: FFF process parameters for shaping of Al_2O_3 green bodies with a 0.8 mm nozzle diameter.

Process parameter	Unit	Value
Printing speed	mm s^{-1}	10
Nozzle temperature	°C	280
Bed temperature	°C	90
Layer height	mm	0.2
Extrusion multiplier	-	1.1
Infill overlap	%	90

Table 29: FFF process parameters for shaping of 316L green bodies with a 0.6 mm nozzle diameter.

Process parameter	Unit	Value
Printing speed	mm s^{-1}	10
Nozzle temperature	°C	290
Bed temperature	°C	100
Layer height	mm	0.2
Extrusion multiplier	-	1.05
Infill overlap	%	25

Table 30: FFF process parameters for shaping of Ampersint 1557 green bodies with a 0.6 mm nozzle diameter.

Process parameter	Unit	Value
Printing speed	mm s^{-1}	10
Nozzle temperature	°C	200
Bed temperature	°C	25
Layer height	mm	0.2
Extrusion multiplier	-	1.2
Infill overlap	%	20

Table 31: FFF process parameters for shaping of cp-Ti green bodies with a 0.6 mm nozzle diameter.

Process parameter	Unit	Value
Printing speed	mm s^{-1}	10
Nozzle temperature	°C	200
Bed temperature	°C	25
Layer height	mm	0.2
Extrusion multiplier	-	1.2
Infill overlap	%	15

Table 32: FFF process parameters for shaping of IN 718 with a 0.6 mm nozzle diameter.

Process parameter	Unit	Value
Printing speed	mm s^{-1}	10
Nozzle temperature	°C	280
Bed temperature	°C	20
Layer height	mm	0.1
Extrusion multiplier	-	1.2
Infill overlap	%	20

Table 33: FFF process parameters for shaping of CoWAlloy3 with a 0.6 mm nozzle diameter.

Process parameter	Unit	Value
Printing speed	mm s^{-1}	10
Nozzle temperature	°C	290
Bed temperature	°C	20
Layer height	mm	0.1
Extrusion multiplier	-	1.2
Infill overlap	%	20

Table 34: FFF process parameters for shaping of copper green bodies with a 0.6 mm nozzle diameter.

Process parameter	Unit	Value
Printing speed	mm s^{-1}	10
Nozzle temperature	°C	250
Bed temperature	°C	90
Layer height	mm	0.1
Extrusion multiplier	-	1.2
Infill overlap	%	20

Bibliography

[1] F04 Committee: *ASTM F67-13, Standard Specification for Unalloyed Titanium, for Surgical Implant Applications (UNS R50250, UNS R50400, UNS R50550, UNS R50700)*. West Conshohocken, PA: ASTM International, 2013.

[2] Hull, C. W.; Gabriel, S.: Apparatus for Production of Three-Dimensional Objects by Stereolithography. U.S. pat. 4575330. 1986.

[3] Hernandez Korner, M. E.; Lambán, M. P.; Albajez, J. A.; Santolaria, J.; Ng Corrales, L. d. C.; Royo, J.: Systematic Literature Review: Integration of Additive Manufacturing and Industry 4.0. In: *Metals* 10.8 (2020), 1061.

[4] Kadir, A. Z. A.; Yusof, Y.; Wahab, M. S.: Additive Manufacturing Cost Estimation Models-a Classification Review. In: *The International Journal of Advanced Manufacturing Technology* 107.9 (2020), 4033–4053.

[5] Agarwala, M. K.; Mukesh, K.; Weeren, R. van; Bandyopadhyay, A.; Safari, A.; Danforth, S. C.; Priedeman, W. R.: *Filament Feed Materials for Fused Deposition Processing of Ceramics and Metals*. In: *Proceedings of the Solid Freeform Fabrication Symposium*. Austin, TX, USA, 1996, 451–458.

[6] Wu, G.; Langrana, N. A.; Rangarajan, S.; McCuiston, R.; Sadanji, R.; Danforth, S.; Safari, A.: *Fabrication of Metal Components Using FDMet: Fused Deposition of Metals*. In: *In Proceedings of the Solid Freeform Fabrication Symposium*. Austin, TX, USA, 1999, 775–782.

[7] Wu, G.; Langrana, N. A.; Sadanji, R.; Danforth, S.: Solid Freeform Fabrication of Metal Components Using Fused Deposition of Metals. In: *Materials & Design* 23.1 (2002), 97–105.

[8] BASF Launches Ultrafuse 316LX for Fused Filament Fabrication of Metal Parts. Metal Additive Manufacturing. 2017. URL: https://www.metal-am.com/basf-launches-ultrafuse-316lx-fused-filament-fabrication-metal-parts/ (visited on 12/06/2018).

[9] Markforged: Complete 3D Metal Printing Solution. Metal X. 2018. URL: https://markforged.com/metal-x/ (visited on 12/06/2018).

[10] Desktop Metal: Introducing Two Metal 3D Printing Systems for the Full Product Life Cycle – from Prototyping to Mass Production. 2018. URL: https://www.desktopmetal.com/ (visited on 06/26/2018).

[11] Burkhardt, C.; Freigassner, P.; Weber, O.; Imgrund, P.; Hampel, S.: *Fused Filament Fabrication (FFF) of 316L Green Parts for the MIM Process*. In: *Proceedings of the World PM2016 Congress & Exhibition*. Hamburg, Germany, 2016, 1–7.

[12] Lieberwirth, C.; Harder, A.; Seitz, H.: Extrusion Based Additive Manufacturing of Metal Parts. In: *Journal of Mechanics Engineering and Automation* 7.2 (2017).

[13] Kukla, C.; Duretek, I.; Schuschnigg, S.; Gonzalez-Gutierrez, J.; Holzer, C.: *Properties for PIM Feedstocks Used in Fused Filament Fabrication*. In: *World PM 2016 Congress and Exhibition*. Hamburg, Germany, 2016.

[14] Andersen, O.; Riecker, S.; Studnitzky, T.; Hein, S.; Lohse, U.; Kie, B.: *Manufacturing and Properties of Metal Parts Made by Fused Filament Fabrication*. In: *Proceedings - Euro PM 2018*. Powder Metallurgy Congress & Exhibition. Vol. SIS - Additive Manufacturing. Bilbao, Spain, 2018, 1–6.

[15] Bose, A. et al.: Traditional and Additive Manufacturing of a New Tungsten Heavy Alloy Alternative. In: *International Journal of Refractory Metals and Hard Materials* 73 (2018), 22–28.

[16] Damon, J.; Dietrich, S.; Gorantla, S.; Popp, U.; Okolo, B.; Schulze, V.: Process Porosity and Mechanical Performance of Fused Filament Fabricated 316L Stainless Steel. In: *Rapid Prototyping Journal* 25.7 (2019), 1319–1327.

[17] Gonzalez-Gutierrez, J.; Arbeiter, F.; Schlauf, T.; Kukla, C.; Holzer, C.: Tensile Properties of Sintered 17-4PH Stainless Steel Fabricated by Material Extrusion Additive Manufacturing. In: *Materials Letters* 248 (2019), 165–168.

[18] Lengauer, W.; Duretek, I.; Fürst, M.; Schwarz, V.; Gonzalez-Gutierrez, J.; Schuschnigg, S.; Kukla, C.; Kitzmantel, M.; Neubauer, E.; Lieberwirth, C.; Morrison, V.: Fabrication and Properties of Extrusion-Based 3D-printed Hardmetal and Cermet Components. In: *International Journal of Refractory Metals and Hard Materials* 82 (2019), 141–149.

[19] Riecker, S.; Hein, S. B.; Studnitzky, T.; Andersen, O.; Kieback, B.: *3D Printing of Metal Parts by Means of Fused Filament Fabrication - A Non Beam-Based Approach*. In: *Euro PM2017 Congress & Exhibition*. Vol. AM Alternative Technologies. Milan, Italy, 2017, 1–6.

[20] Altan, T.; Miller, R. A.: Design for Forming and Other Near Net Shape Manufacturing Processes. In: *CIRP Annals* 39.2 (1990), 609–620.

[21] Cominotti, R.; Gentili, E.: Near Net Shape Technology: An Innovative Opportunity for the Automotive Industry. In: *Robotics and Computer-Integrated Manufacturing* 24.6 (2008), 722–727.

[22] Doege, E.; Thalemann, J.: Near Net-Shape Forming in Sheet-Metal Forming and Forging. In: *CIRP Annals* 38.2 (1989), 609–616.

[23] Marini, D.; Cunningham, D.; Corney, J. R.: Near Net Shape Manufacturing of Metal: A Review of Approaches and Their Evolutions. In: *Proceedings of the Institution of Mechanical Engineers, Part B: Journal of Engineering Manufacture* 232.4 (2018), 650–669.

[24] Marini, D.; Corney, J. R.: Process Selection Methodology for near Net Shape Manufacturing. In: *The International Journal of Advanced Manufacturing Technology* 106.5 (2020), 1967–1987.

[25] Kumar, S.: *Additive Manufacturing Processes*. Cham; Germany: Springer International Publishing, 2020. 205 pp.

[26] Gibson, I.; Rosen, D. W.; Stucker, B.: *Additive Manufacturing Technologies: Rapid Prototyping to Direct Digital Manufacturing*. London; New York: Springer, 2010. 459 pp.

[27] Herzog, D.; Seyda, V.; Wycisk, E.; Emmelmann, C.: Additive Manufacturing of Metals. In: *Acta Materialia* 117 (2016), 371–392.

[28] Bhuvanesh Kumar, M.; Sathiya, P.: Methods and Materials for Additive Manufacturing: A Critical Review on Advancements and Challenges. In: *Thin-Walled Structures* 159 (2020), 107228.

[29] Cooke, S.; Ahmadi, K.; Willerth, S.; Herring, R.: Metal Additive Manufacturing: Technology, Metallurgy and Modelling. In: *Journal of Manufacturing Processes* 57 (2020), 978–1003.

[30] Gokuldoss, P. K.; Kolla, S.; Eckert, J.: Additive Manufacturing Processes: Selective Laser Melting, Electron Beam Melting and Binder Jetting - Selection Guidelines. In: *Materials* 10.6 (2017), 672.

[31] Gu, D. D.; Meiners, W.; Wissenbach, K.; Poprawe, R.: Laser Additive Manufacturing of Metallic Components: Materials, Processes and Mechanisms. In: *International Materials Reviews* 57.3 (2012), 133–164.

[32] Sames, W. J.; List, F. A.; Pannala, S.; Dehoff, R. R.; Babu, S. S.: The Metallurgy and Processing Science of Metal Additive Manufacturing. In: *International Materials Reviews* 61.5 (2016), 315–360.

[33] ISO/ASTM 52900(En), Additive Manufacturing - General Principles - Terminology. URL: https://www.iso.org/obp/ui/#iso:std:iso-astm:52900:dis:ed-2:v1:en (visited on 12/22/2020).

[34] *ASTM F2792-12a, Standard Terminology for Additive Manufacturing Technologies, (Withdrawn 2015)*. In: ASTM International, West Conshohocken. Conshohocken, PA, 2012.

[35] Peng, X.; Kong, L.; Fuh, J. Y. H.; Wang, H.: A Review of Post-Processing Technologies in Additive Manufacturing. In: *Journal of Manufacturing and Materials Processing* 5.2 (2021), 38.

[36] Kok, Y.; Tan, X.; Wang, P.; Nai, M.; Loh, N.; Liu, E.; Tor, S.: Anisotropy and Heterogeneity of Microstructure and Mechanical Properties in Metal Additive Manufacturing: A Critical Review. In: *Materials & Design* 139 (2018), 565–586.

[37] Bandyopadhyay, A.; Zhang, Y.; Bose, S.: Recent Developments in Metal Additive Manufacturing. In: *Current Opinion in Chemical Engineering* 28 (2020), 96–104.

[38] Kontis, P.; Chauvet, E.; Peng, Z.; He, J.; da Silva, A. K.; Raabe, D.; Tassin, C.; Blandin, J.-J.; Abed, S.; Dendievel, R.; Gault, B.; Martin, G.: Atomic-Scale Grain Boundary Engineering to Overcome Hot-Cracking in Additively-Manufactured Superalloys. In: *Acta Materialia* 177 (2019), 209–221.

[39] Ardila, L.; Garciandia, F.; Gonzalez-Diaz, J.; Alvarez, P.; Echeverria, A.; Petite, M.; Deffley, R.; Ochoa, J.: Effect of IN718 Recycled Powder Reuse on Properties of Parts Manufactured by Means of Selective Laser Melting. In: *Physics Procedia* 56 (2014), 99–107.

[40] Casati, R.; Coduri, M.; Lecis, N.; Andrianopoli, C.; Vedani, M.: Microstructure and Mechanical Behavior of Hot-Work Tool Steels Processed by Selective Laser Melting. In: *Materials Characterization* 137 (2018), 50–57.

[41] Facchini, L.; Magalini, E.; Robotti, P.; Molinari, A.; Höges, S.; Wissenbach, K.: Ductility of a Ti-6Al-4V Alloy Produced by Selective Laser Melting of Prealloyed Powders. In: *Rapid Prototyping Journal* 16.6 (2010), 450–459.

[42] Feng, K.-y.; Liu, P.; Li, H.-x.; Sun, S.-y.; Xu, S.-b.; Li, J.-n.: Microstructure and Phase Transformation on the Surface of Inconel 718 Alloys Fabricated by SLM under 1050°C Solid Solution + Double Ageing. In: *Vacuum* 145 (2017), 112–115.

[43] Koike, M.; Greer, P.; Owen, K.; Lilly, G.; Murr, L. E.; Gaytan, S. M.; Martinez, E.; Okabe, T.: Evaluation of Titanium Alloys Fabricated Using Rapid Prototyping Technologies - Electron Beam Melting and Laser Beam Melting. In: *Materials* 4.10 (2011), 1776–1792.

[44] Li, X.; Shi, J.; Wang, C.; Cao, G.; Russell, A.; Zhou, Z.; Li, C.; Chen, G.: Effect of Heat Treatment on Microstructure Evolution of Inconel 718 Alloy Fabricated by Selective Laser Melting. In: *Journal of Alloys and Compounds* 764 (2018), 639–649.

[45] Liverani, E.; Toschi, S.; Ceschini, L.; Fortunato, A.: Effect of Selective Laser Melting (SLM) Process Parameters on Microstructure and Mechanical Properties of 316L Austenitic Stainless Steel. In: *Journal of Materials Processing Technology* 249 (2017), 255–263.

[46] Mazur, M.; Leary, M.; McMillan, M.; Elambasseril, J.; Brandt, M.: SLM Additive Manufacture of H13 Tool Steel with Conformal Cooling and Structural Lattices. In: *Rapid Prototyping Journal* 22.3 (2016), 504–518.

[47] Vilaro, T.; Colin, C.; Bartout, J. D.: As-Fabricated and Heat-Treated Microstructures of the Ti-6Al-4V Alloy Processed by Selective Laser Melting. In: *Metallurgical and Materials Transactions A* 42.10 (2011), 3190–3199.

[48] Guschlbauer, R.; Momeni, S.; Osmanlic, F.; Körner, C.: Process Development of 99.95% Pure Copper Processed via Selective Electron Beam Melting and Its Mechanical and Physical Properties. In: *Materials Characterization* 143 (2018), 163–170.

[49] Raab, S. J.; Guschlbauer, R.; Lodes, M. A.; Körner, C.: Thermal and Electrical Conductivity of 99.9% Pure Copper Processed via Selective Electron Beam Melting: Conductivities of Pure SEBM-Copper. In: *Advanced Engineering Materials* 18.9 (2016), 1661–1666.

[50] Murr, L. E.; Li, S.: Electron-Beam Additive Manufacturing of High-Temperature Metals. In: *MRS Bulletin* 41.10 (2016), 752–757.

[51] Duda, T.; Raghavan, L. V.: 3D Metal Printing Technology. In: *IFAC-PapersOnLine* 49.29 (2016), 103–110.

[52] Ding, D.; Pan, Z.; Cuiuri, D.; Li, H.: Wire-Feed Additive Manufacturing of Metal Components: Technologies, Developments and Future Interests. In: *The International Journal of Advanced Manufacturing Technology* 81.1 (2015), 465–481.

[53] Ge, J.; Ma, T.; Chen, Y.; Jin, T.; Fu, H.; Xiao, R.; Lei, Y.; Lin, J.: Wire-Arc Additive Manufacturing H13 Part: 3D Pore Distribution, Microstructural Evolution, and Mechanical Performances. In: *Journal of Alloys and Compounds* 783 (2019), 145–155.

[54] Satish Kumar, P.; Suvarna Raju, L.; Siva Rama Krishna, L.: A Review on Wire Arc Additive Manufacturing (WAAM) Fabricated Components of Ti6AL4V and Steels. In: *International Conference on Emerging Trends in Engineering (ICETE)*. Ed. by Satapathy, S. C.; Raju, K. S.; Molugaram, K.; Krishnaiah, A.; Tsihrintzis, G. A. Vol. 2. Learning and Analytics in Intelligent Systems. Cham, Germany: Springer International Publishing, 2020, 587–600.

[55] Wang, F.; Williams, S.; Colegrove, P.; Antonysamy, A. A.: Microstructure and Mechanical Properties of Wire and Arc Additive Manufactured Ti-6Al-4V. In: *Metallurgical and Materials Transactions A* 44.2 (2013), 968–977.

[56] Liu, J.; Xu, Y.; Ge, Y.; Hou, Z.; Chen, S.: Wire and Arc Additive Manufacturing of Metal Components: A Review of Recent Research Developments. In: *The International Journal of Advanced Manufacturing Technology* 111.1 (2020), 149–198.

[57] Thompson, Y.; Polzer, M.; Gonzalez-Gutierrez, J.; Kasian, O.; Heckl, J. P.; Dalbauer, V.; Kukla, C.; Felfer, P. J.: Fused Filament Fabrication-based Additive Manufacturing of Commercially Pure Titanium. In: *Advanced Engineering Materials* 23.12 (2021), 2100380.

[58] Vaezi, M.; Drescher, P.; Seitz, H.: Beamless Metal Additive Manufacturing. In: *Materials* 13.4 (2020), 922.

[59] Wheat, E.; Vlasea, M.; Hinebaugh, J.; Metcalfe, C.: Sinter Structure Analysis of Titanium Structures Fabricated via Binder Jetting Additive Manufacturing. In: *Materials & Design* 156 (2018), 167–183.

[60] Ali, M.; Ahmad, F.; Melor, P. S.; Yahya, N.; Altaf, K.; Omar, M. A.; Aslam, M.: Binder Removal by a Two-Stage Debinding Process for Powder Injection Molding Fe–50Ni Alloy Parts. In: *Materials Research Express* 6.8 (2019), 0865e3.

[61] Hwang, K. S.; Lin, H. K.; Lee, S. C.: Thermal, Solvent, and Vacuum Debinding Mechanisms of PIM Compacts. In: *Materials and Manufacturing Processes* 12.4 (1997), 593–608.

[62] Fan, Y.-L.; Hwang, K.-S.; Wu, S.-H.; Liau, Y.-C.: Minimum Amount of Binder Removal Required during Solvent Debinding of Powder-Injection-Molded Compacts. In: *Metallurgical and Materials Transactions A* 40.4 (2009), 768–779.

[63] Dwivedi, A.; Speyer, R. F.: Rate-Controlled Organic Burnout of Multilayer Green Ceramics. In: *Thermochimica acta* 247.2 (1994), 431–438.

[64] Enneti, R. K.; Park, S. J.; German, R. M.; Atre, S. V.: Review: Thermal Debinding Process in Particulate Materials Processing. In: *Materials and Manufacturing Processes* 27.2 (2012), 103–118.

[65] Chen, X.: Particle Packing, Compaction and Sintering in Powder Metallurgy. PhD thesis. University of Alberta, 1998.

[66] German, R. M.: *Gravitational Effects on Distortion in Sintering*. In: *2002 Microgravity Materials Science Conference*. Huntsville, Alabama USA, 2003, 1–6.

[67] Lu, P.; Xu, X.; Yi, W.; German, R. M.: Porosity Effect on Densification and Shape Distortion in Liquid Phase Sintering. In: *Materials Science and Engineering: A* 318.1 (2001), 111–121.

[68] Tandon, R.: Metal Injection Molding. In: *Encyclopedia of Materials: Science and Technology*. Ed. by Buschow, K. J.; Cahn, R. W.; Flemings, M. C.; Ilschner, B.; Kramer, E. J.; Mahajan, S.; Veyssière, P. Oxford: Elsevier, 2001, 5439–5442.

[69] Heaney, D. F., ed.: *Handbook of Metal Injection Molding*. Woodhead Publishing Series in Metals and Surface Engineering. Oxford Cambridge Philadelphia New Delhi: Elsevier Science, 2012.

[70] Suwanpreecha, C.; Manonukul, A.: A Review on Material Extrusion Additive Manufacturing of Metal and How It Compares with Metal Injection Moulding. In: *Metals* 12.3 (2022), 429.

[71] Berginc, B.; Kampus, Z.; Sustarsic, B.: Influence of Feedstock Characteristics and Process Parameters on Properties of MIM Parts Made of 316L. In: *Powder Metallurgy* 50.2 (2007), 172–183.

[72] Carvalho, M. A.; Wendhausen, P. A.; Hartwig, T.: Production of Composite Parts of H13 and 316L by Two Components Injection Molding. In: *Materials Science Forum* 530–531 (2006), 236–241.

[73] Ebel, T.; Friederici, V.; Imgrund, P.; Hartwig, T.: 19 - Metal Injection Molding of Titanium. In: *Titanium Powder Metallurgy*. Ed. by Qian, M.; (Sam) Froes, F. H. Boston: Butterworth-Heinemann, 2015, 337–360.

[74] German, R.: *Powder Injection Molding*. Princeton, N.J.: Metal Powder Industries Federation, 1990.

[75] German, R.: Progress in Titanium Metal Powder Injection Molding. In: *Materials* 6.8 (2013), 3641–3662.

[76] Horke, K.; Meyer, A.; Singer, R. F.: 24 - Metal Injection Molding (MIM) of Nickel-Base Superalloys. In: *Handbook of Metal Injection Molding (Second Edition)*. Ed. by Heaney, D. F. Woodhead Publishing Series in Metals and Surface Engineering. Woodhead Publishing, 2019, 575–608.

[77] Veltl, G.; Hartwig, T.; Petzoldt, F.; Kunze, H.-D.: Investigations on Metal Injection Molding of 316L Stainless Steel. In: *Materials and Manufacturing Processes* 10.3 (1995), 425–438.

[78] Wu, Y.; Blaine, D.; Schlaefer, C.; Marx, B.; German, R. M.: Sintering Densification and Microstructural Evolution of Injection Molding Grade 17-4 PH Stainless Steel Powder. In: *Metallurgical and materials transactions A* 33.7 (2002), 2185–2194.

[79] Froes, F.: Getting Better: Big Boost for Titanium MIM Prospects. In: *Metal Powder Report* 61.11 (2006), 20–23.

[80] Gonzalez-Gutierrez, J.; Duretek, I.; Kukla, C.; Poljšak, A.; Bek, M.; Emri, I.; Holzer, C.: Models to Predict the Viscosity of Metal Injection Molding Feedstock Materials as Function of Their Formulation. In: *Metals* 6.6 (2016), 129.

[81] Gonzalez-Gutierrez, J.; Cano, S.; Schuschnigg, S.; Kukla, C.; Sapkota, J.; Holzer, C.: Additive Manufacturing of Metallic and Ceramic Components by the Material Extrusion of Highly-Filled Polymers: A Review and Future Perspectives. In: *Materials* 11.5 (2018), 840.

[82] Chong, J. S.; Christiansen, E. B.; Baer, A. D.: Rheology of Concentrated Suspensions. In: *Journal of applied polymer science* 15.8 (1971), 2007–2021.

[83] Honek, T.; Hausnerova, B.; Saha, P.: Relative Viscosity Models and Their Application to Capillary Flow Data of Highly Filled Hard-Metal Carbide Powder Compounds. In: *Polymer Composites* 26.1 (2005), 29–36.

[84] Kate, K. H.; Enneti, R. K.; Park, S.-J.; German, R. M.; Atre, S. V.: Predicting Powder-Polymer Mixture Properties for PIM Design. In: *Critical Reviews in Solid State and Materials Sciences* 39.3 (2014), 197–214.

[85] Kong, X.; Barriere, T.; Gelin, J.: Determination of Critical and Optimal Powder Loadings for 316L Fine Stainless Steel Feedstocks for Micro-Powder Injection Molding. In: *Journal of Materials Processing Technology* 212.11 (2012), 2173–2182.

[86] Bek, M.; Gonzalez-Gutierrez, J.; Kukla, C.; Pušnik Črešnar, K.; Maroh, B.; Slemenik Perše, L.: Rheological Behaviour of Highly Filled Materials for Injection Moulding and Additive Manufacturing: Effect of Particle Material and Loading. In: *Applied Sciences* 10.22 (2020), 7993.

[87] Kukla, C.; Duretek, I.; Gonzalez-Gutierrez, J.; Holzer, C.: Rheology of Highly Filled Polymers. In: *Polymer Rheology*. Ed. by Rivera-Armenta, J. L.; Cruz, B. A. S. IntechOpen, 2018, 153–173.

[88] Strano, M.; Rane, K.; Briatico Vangosa, F.; Di Landro, L.: Extrusion of Metal Powder-Polymer Mixtures: Melt Rheology and Process Stability. In: *Journal of Materials Processing Technology* 273 (2019), 116250.

[89] Gong, H.; Snelling, D.; Kardel, K.; Carrano, A.: Comparison of Stainless Steel 316L Parts Made by FDM- and SLM-Based Additive Manufacturing Processes. In: *JOM* 71.3 (2019), 880–885.

[90] Agarwala, M. K.; Weeren, R. V.; Bandyopadhyay, A.; Whalen, P. J.; Safari, A.; Danforth, S. C.: *Fused Deposition of Ceramics and Metals: An Overview*. In: *1996 International Solid Freeform Fabrication Symposium*. Austin, Texas, USA, 1996.

[91] Pekin, S.; Bukowski, J.; Zangvil, A.: *A Study on Weight Loss Rate Controlled Binder Removal from Parts Produced by FDC*. In: *1998 International Solid Freeform Fabrication Symposium*. Austin, Texas, USA, 1998, 651–660.

[92] Abel, J.; Scheithauer, U.; Janics, T.; Hampel, S.; Cano, S.; Müller-Köhn, A.; Günther, A.; Kukla, C.; Moritz, T.: Fused Filament Fabrication (FFF) of Metal-Ceramic Components. In: *Journal of Visualized Experiments* 143 (2019), e57693.

[93] Gonzalez-Gutierez, J.; Godec, D.; Guráň, R.; Spoerk, M.; Kukla, C.; Holzer, C.: 3D Printing Conditions Determination for Feedstock Used in Fused Filament Fabrication (FFF) of 17-4PH Stainless Steel Parts. In: *Metalurgija* 57.1-2 (2018), 117–120.

[94] Gonzalez-Gutierrez, J.; Godec, D.; Kukla, C.; Schlauf, T.; Burkhardt, C.; Holzer, C.: *Shaping, Debinding and Sintering of Steel Components via Fused Filament Fabrication*. In: *16th International Scientific Conference on Production Engineering - Computer Integrated Manufacturing and High Speed Machining*. Zadar, Croatia: 16, 2017, 99–104.

[95] Kukla, C.; Gonzalez-Gutierrez, J.; Duretek, I.; Schuschnigg, S.; Holzer, C.: *Effect of Particle Size on the Properties of Highly-Filled Polymers for Fused Filament Fabrication*. In: *AIP Conference Proceedings*. Vol. 1914. Lyon, France, 2017, 190006.

[96] Dimitri, C.; Mohamed, S.; Thierry, B.; Jean-Claude, G.: Influence of Particle-Size Distribution and Temperature on the Rheological Properties of Highly Concentrated Inconel Feedstock Alloy 718. In: *Powder Technology* 322 (2017), 273–289.

[97] Yang, W.-W.; Yang, K.-Y.; Wang, M.-C.; Hon, M.-H.: Solvent Debinding Mechanism for Alumina Injection Molded Compacts with Water-Soluble Binders. In: *Ceramics International* 29.7 (2003), 745–756.

[98] Yang, X.; Jia, C.; Xie, Z.; Liu, W.; Liu, Q.: Water-Soluble Binder System Based on Poly-Methyl Methacrylate and Poly-Ethylene Glycol for Injection Molding of Large-Sized Ceramic Parts. In: *International Journal of Applied Ceramic Technology* 10.2 (2013), 339–347.

[99] Yang, X.; Petcavich, R. J.: Powder and Binder Systems for Use in Metal and Ceramic Powder Injection Molding. U.S. pat. 6008281. 1999.

[100] Ren, L.; Zhou, X.; Song, Z.; Zhao, C.; Liu, Q.; Xue, J.; Li, X.: Process Parameter Optimization of Extrusion-Based 3D Metal Printing Utilizing PW–LDPE–SA Binder System. In: *Materials* 10.3 (2017), 305.

[101] Khan, S.; Prud'homme, R.: Melt Rheology of Filled Thermoplastics. In: *Reviews in Chemical Engineering* 4.3-4 (1987), 205–272.

[102] Vand, V.: Viscosity of Solutions and Suspensions. I. Theory. In: *The Journal of Physical and Colloid Chemistry* 52.2 (1948), 277–299.

[103] Tsutsumi, A.; Yoshida, K.; Yui, M.; Kanamori, S.; Shibata, K.: Shear Viscosity Behavior of Flocculated Suspensions. In: *Powder Technology* 78.2 (1994), 165–172.

[104] Pal, R.: New Generalized Viscosity Model for Non-Colloidal Suspensions and Emulsions. In: *Fluids* 5.3 (2020), 150.

[105] Mueller, S.; Llewellin, E. W.; Mader, H. M.: The Rheology of Suspensions of Solid Particles. In: *Proceedings of the Royal Society A: Mathematical, Physical and Engineering Sciences* 466.2116 (2010), 1201–1228.

[106] Graham, A. L.: On the Viscosity of Suspensions of Solid Spheres. In: *Applied Scientific Research* 37.3-4 (1981), 275–286.

[107] Krieger, I. M.; Dougherty, T. J.: A Mechanism for Non-Newtonian Flow in Suspensions of Rigid Spheres. In: *Transactions of the Society of Rheology* 3.1 (1959), 137–152.

[108] Mooney, M.: The Viscosity of a Concentrated Suspension of Spherical Particles. In: *Journal of colloid science* 6.2 (1951), 162–170.

[109] Rueda, M. M.; Auscher, M.-C.; Fulchiron, R.; Périé, T.; Martin, G.; Sonntag, P.; Cassagnau, P.: Rheology and Applications of Highly Filled Polymers: A Review of Current Understanding. In: *Progress in Polymer Science* 66 (2017), 22–53.

[110] Beran, T.; Mulholland, T.; Henning, F.; Rudolph, N.; Osswald, T. A.: Nozzle Clogging Factors during Fused Filament Fabrication of Spherical Particle Filled Polymers. In: *Additive Manufacturing* 23 (2018), 206–214.

[111] Sharp, K. V.; Adrian, R. J.: On Flow-Blocking Particle Structures in Microtubes. In: *Microfluidics and Nanofluidics* 1.4 (2005), 376–380.

[112] Bellehumeur, C.; Li, L.; Sun, Q.; Gu, P.: Modeling of Bond Formation Between Polymer Filaments in the Fused Deposition Modeling Process. In: *Journal of Manufacturing Processes* 6.2 (2004), 170–178.

[113] Sun, Q.; Rizvi, G. M.; Bellehumeur, C. T.; Gu, P.: *Experimental Study of the Cooling Characteristics of Polymer Filaments in FDM and Impact on the Mesostructures and Properties of Prototypes*. In: *2003 Solid Freeform Fabrication Symposium*. Austin, Texas, USA, 2003.

[114] Parenti, P.; Cataldo, S.; Grigis, A.; Covelli, M.; Annoni, M.: Implementation of Hybrid Additive Manufacturing Based on Extrusion of Feedstock and Milling. In: *Procedia Manufacturing* 34 (2019), 738–746.

[115] Hamidi, M. F. F. A.; Harun, W. S. W.; Khalil, N. Z.; Ghani, S. A. C.; Azir, M. Z.: Study of Solvent Debinding Parameters for Metal Injection Moulded 316L Stainless Steel. In: *IOP Conference Series: Materials Science and Engineering*. IOP Publishing 257.1 (2017), 012035.

[116] Zaky, M. T.: Effect of Solvent Debinding Variables on the Shape Maintenance of Green Molded Bodies. In: *Journal of Materials Science* 39.10 (2004), 3397–3402.

[117] Van Brakel, J.: Pore Space Models for Transport Phenomena in Porous Media Review and Evaluation with Special Emphasis on Capillary Liquid Transport. In: *Powder Technology* 11.3 (1975), 205–236.

[118] Lii, D.-F.; Huang, J.-L.; Lin, C.-H.; Lu, H.-H.: The Effects of Atmosphere on the Thermal Debinding of Injection Moulded Si3N4 Components. In: *Ceramics international* 24.2 (1998), 99–104.

[119] Li, R. K. Y.; Wu, C. M. L.; Wong, T. L.: Thermogravimetric and Binder Removal Analysis of Injection Moulded Reinforced Ceramic Composite. In: *Composite structures* 38.1-4 (1997), 483–487.

[120] Seerane, M.; Chikwanda, H.; Machaka, R.: Determination of Optimum Process for Thermal Debinding and Sintering Using Taguchi Method. In: *Materials Science Forum* 828 (Trans Tech Publications Ltd 2015), 138–144.

[121] Becker, F.: Debinding Processes - Physical and Chemical Conclusions and Their Practical Realisations. In: *Ceramic Forum International* 83.5 (2006), 88–99.

[122] Supriadi, S.; Suharno, B.; Hidayatullah, R.; Maulana, G.; Baek, E. R.: Thermal Debinding Process of SS 17-4 PH in Metal Injection Molding Process with Variation of Heating Rates, Temperatures, and Holding Times. In: *Solid State Phenomena* 266 (Trans Tech Publications Ltd 2017), 238–244.

[123] Derfuss, B.; Gruhl, M.; Rottmair, C.; Volek, A.; Singer, R.: Net-Shape Production of Graphite Parts via Powder Injection Moulding of Carbon Mesophase. In: *Journal of Materials Processing Technology* 208.1-3 (2008), 444–449.

[124] Witt, J.; Speyer, R. F.; Murali, L.: Binder Extraction from Green Multilayer Ceramics Using a Weight Loss Rate-Controlled Thermogravimetric Analyzer. In: *Review of Scientific Instruments* 68.6 (1997), 2546–2549.

[125] Pietsch, W.; Rumpf, H.: Haftkraft, Kapillardruck, Flüssigkeitsvolumen und Grenzwinkel einer Flüssigkeitsbrücke zwischen zwei Kugeln: Haftkraft, Kapillardruck, Flüssigkeitsvolumen und Grenzwinkel einer Flüssigkeitsbrücke zwischen zwei Kugeln. In: *Chemie Ingenieur Technik* 39.15 (1967), 885–893.

[126] Schubert, H.: Grundlagen des Agglomerierens. In: *Chemie Ingenieur Technik* 51.4 (1979), 266–277.

[127] German, R. M.: *Strength Evolution in Debinding and Sintering*. In: *Proceedings of the 3rd International Conference on the Science, Technology & Applications of Sintering*. 2003, 15–17.

[128] Shibo, G.; Xuanhui, Q.; Xinbo, H.; Ting, Z.; Bohua, D.: Powder Injection Molding of Ti–6Al–4V Alloy. In: *Journal of Materials Processing Technology* 173.3 (2006), 310–314.

[129] Jordan, C. B.; Duwez, P.: The Densification of Copper Powder Compacts in Hydrogen and in Vacuum. In: *JOM* 1.2 (1949), 96–99.

[130] Munir, Z. A.: Analytical Treatment of the Role of Surface Oxide Layers in the Sintering of Metals. In: *Journal of Materials Science* 14.11 (1979), 2733–2740.

[131] Ho, Y. L.; Lin, S. T.: Debinding Variables Affecting the Residual Carbon Content of Injection-Molded Fe-2 Pct Ni Steels. In: *Metallurgical and Materials Transactions A* 26.1 (1995), 133–142.

[132] Besler, R.; Bauer, M.; Furlan, K. P.; Klein, A. N.; Janssen, R.: Effect of Processing Route on the Microstructure and Mechanical Properties of Hot Work Tool Steel. In: *Materials Research* 20.6 (2017), 1518–1524.

[133] German, R. M.: Coarsening in Sintering: Grain Shape Distribution, Grain Size Distribution, and Grain Growth Kinetics in Solid-Pore Systems. In: *Critical Reviews in Solid State and Materials Sciences* 35.4 (2010), 263–305.

[134] Kruis, F. E.; Kusters, K. A.; Pratsinis, S. E.; Scarlett, B.: A Simple Model for the Evolution of the Characteristics of Aggregate Particles Undergoing Coagulation and Sintering. In: *Aerosol Science and Technology* 19.4 (1993), 514–526.

[135] German, R. M.; Park, S. J.: *German, Randall M., and Seong Jin Park. Handbook of Mathematical Relations in Particulate Materials Processing: Ceramics, Powder Metals, Cermets, Carbides, Hard Materials, and Minerals*. Hoboken, NJ, USA: John Wiley & Sons, 2009.

[136] Coble, R. L.: Sintering Crystalline Solids. I. Intermediate and Final State Diffusion Models. In: *Journal of Applied Physics* 32.5 (1961), 787–792.

[137] Geach, G. A.: The Theory of Sintering. In: *Progress in Metal physics* 4 (1953), 174–204.

[138] Harun, A.; Holm, E.; Clode, M.; Miodownik, M.: On Computer Simulation Methods to Model Zener Pinning. In: *Acta Materialia* 54.12 (2006), 3261–3273.

[139] German, R. M.: Coarsening in Sintering: Grain Shape Distribution, Grain Size Distribution, and Grain Growth Kinetics in Solid-Pore Systems. In: *Critical Reviews in Solid State and Materials Sciences* 35.4 (2010), 263–305.

[140] German, R.: *Sintering: From Empirical Observations to Scientific Principles*. Butterworth-Heinemann, 2014.

[141] Weiser, M. W.: Rearrangement during Sintering of Two Dimensional Arrays of Spheres. M.Sc. Thesis. Lawrence Berkeley Laboratory, University of California, 1985.

[142] Olevsky, E. A.; German, R. M.: Effect of Gravity on Dimensional Change during Sintering - I Shrinkage Anisotropy. In: *Acta materialia* 48.5 (2000), 1153–1166.

[143] Kurose, T.; Abe, Y.; Santos, M. V. A.; Kanaya, Y.; Ishigami, A.; Tanaka, S.; Ito, H.: Influence of the Layer Directions on the Properties of 316L Stainless Steel Parts Fabricated through Fused Deposition of Metals. In: *Materials* 13.11 (2020), 2493.

[144] Thümmler, F.; Thomma, W.: The Sintering Process. In: *Metallurgical Reviews* 12.1 (1967), 69–108.

[145] Moore, J. A.; Jarding, B. P.; Lograsso, B. K.; Anderson, I. E.: Atmosphere Control during Debinding of Powder Injection Molded Parts. In: *Journal of Materials Engineering and Performance* 4.3 (1995), 275–282.

[146] Kankawa, Y.: Effects of Polymer Decomposition Behavior on Thermal Debinding Process in Metal Injection Molding. In: *Materials and Manufacturing Processes* 12.4 (1997), 681–690.

[147] Rane, K.; Strano, M.: A Comprehensive Review of Extrusion-Based Additive Manufacturing Processes for Rapid Production of Metallic and Ceramic Parts. In: *Advances in Manufacturing* 7.2 (2019), 155–173.

[148] Rahaman, M.: *Ceramic Processing and Sintering, Second Edition*. CRC press, 2017, 1–875. 876 pp.

[149] Stanimirovi, Z.: Ceramic Injection Molding. In: *Some Critical Issues for Injection Molding*. Ed. by Wang, J. Rijeka, Croatia: InTech, 2012, 131–148.

[150] Grida, I.; Evans, J. R.: Extrusion Freeforming of Ceramics through Fine Nozzles. In: *Journal of the European Ceramic Society* 23.5 (2003), 629–635.

[151] Enneti, R. K.: Thermal Analysis and Evolution of Shape Loss Phenomena during Polymer Burnout in Powder Metal Processing. PhD thesis. The Pennsylvania State University, 2005.

[152] Schatt, W., Wieters, K.-P., Kieback, B., eds.: *Pulvermetallurgie: Technologien und Werkstoffe*. 2., bearb. und erw. Aufl. VDI. Berlin: Springer, 2007. 552 pp.

[153] Pulgarín, H. L. C.; Albano, M. P.: Sintering and Microstrusture of Al2O3 and Al2O3-ZrO2 Ceramics. In: *Procedia Materials Science* 8 (2015), 180–189.

[154] Danninger, H.; Gierl, C.; Kremel, S.; Leitner, G.; Jaenicke-Roessler, K.; Yu, Y.: Degassing and Deoxidation Processes during Sintering of Unalloyed and Alloyed PM Steels. In: *Powder Metallurgy Progress(Slovak Republic)* 2.3 (2002), 125–140.

[155] Lin, S. T.: Interface Controlled Decarburisation Model for Injection Moulded Parts During Debinding. In: *Powder Metallurgy* 40.1 (1997), 66–72.

[156] Han, G.; Lu, Z.; Ru, X.; Chen, J.; Zhang, J.; Shoji, T.: Properties of Oxide Films Formed on 316L SS and Model Alloys with Modified Ni, Cr and Si Contents in High Temperature Water. In: *Corrosion Science* 106 (2016), 157–171.

[157] Ji, C. H.; Loh, N. H.; Khor, K. A.; Tor, S. B.: Sintering Study of 316L Stainless Steel Metal Injection Molding Parts Using Taguchi Method: Final Density. In: *Materials Science and Engineering: A* 311.1 (2001), 74–82.

[158] Kurgan, N.: Effects of Sintering Atmosphere on Microstructure and Mechanical Property of Sintered Powder Metallurgy 316L Stainless Steel. In: *Materials & Design (1980-2015)* 52 (2013), 995–998.

[159] Li, S.; Huang, B.; Li, D.; Li, Y.; Liang, S.; Zhou, H.: Influences of Sintering Atmospheres on Densification Process of Injection Moulded Gas Atomised 316L Stainless Steel. In: *Powder Metallurgy* 46.3 (2003), 241–245.

[160] Yoon, T. S.; Lee, Y. H.; Ahn, S. H.; Lee, J. H.; Lee, C. S.: Effects of Sintering Conditions on the Mechanical Properties of Metal Injection Molded 316L Stainless Steel. In: *ISIJ International* 43.1 (2003), 119–126.

[161] Kriaa, A.; Hamdi, N.; Sidhom, H.: Assessment of Intergranular Corrosion of Heat Treated Austenitic Stainless Steel (AISI 316L Grade) by Electron Microscopy and Electrochemical Tests. In: *Protection of Metals* 44.5 (2008), 506–513.

[162] Danninger, H.; Gierl, C.: Processes in PM Steel Compacts during the Initial Stages of Sintering. In: *Materials Chemistry and Physics* 67.1-3 (2001), 49–55.

[163] De Oro Calderon, R.; Gierl-Mayer, C.; Danninger, H.: Application of Thermal Analysis Techniques to Study the Oxidation/Reduction Phenomena during Sintering of Steels Containing Oxygen-Sensitive Alloying Elements. In: *Journal of Thermal Analysis and Calorimetry* 127.1 (2017), 91–105.

[164] Pasang, T.; Chen, Z.; Ramezani, M.; Neitzert, T.; Au, D.: The Effect of Heat Treatment Atmosphere on Hardening of Surface Region of H13 Tool Steel. In: *Journal of Materials Science and Chemical Engineering* 1.6 (2013), 20–29.

[165] Guanghua, Y.; Xinmin, H.; Yanqing, W.; Xingguo, Q.; Ming, Y.; Zuoming, C.; Kang, J.: Effects of Heat Treatment on Mechanical Properties of H13 Steel. In: *Metal Science and Heat Treatment* 52.7 (2010), 393–395.

[166] Mutlu, I.; Oktay, E.; Ekinci, S.: Characterization of Microstructure of H13 Tool Steel Using Ultrasonic Measurements. In: *Russian Journal of Nondestructive Testing* 49.2 (2013), 112–120.

[167] German, R. M.: Titanium Sintering Science: A Review of Atomic Events during Densification. In: *International Journal of Refractory Metals and Hard Materials* 89 (2020), 105214.

[168] Akechi, K.; Hara, Z.: Increase of Sintering Rate of Titanium Powder During Cyclic Phase Transformation. In: *Powder Metallurgy* 24.1 (1981), 41–46.

[169] Lütjering, G.; Williams, J. C.: *Titanium*. 2nd ed. Springer-Verlag Berlin Heidelberg, 2007.

[170] Yan, M.; Luo, S. D.; Schaffer, G. B.; Qian, M.: Impurity (Fe, Cl, and P)-Induced Grain Boundary and Secondary Phases in Commercially Pure Titanium (CP-Ti). In: *Metallurgical and Materials Transactions A* 44.8 (2013), 3961–3969.

[171] Akca, E.; Gürsel, A.: A Review on Superalloys and IN718 Nickel-Based INCONEL Superalloy. In: *Periodicals of Engineering and Natural Sciences (PEN)* 3.1 (2015), 15–27.

[172] Bürgel, R.; Maier, H.-J.; Niendorf, T.; Maier, H. J.: *Handbuch Hochtemperatur-Werkstofftechnik: Grundlagen, Werkstoffbeanspruchungen, Hochtemperaturlegierungen und -beschichtungen ; mit 66 Tabellen*. 4., überarb. Auflage. Praxis. Wiesbaden: Vieweg + Teubner, 2011. 597 pp.

[173] Sato, J.; Omori, T.; Oikawa, K.; Ohnuma, I.; Kainuma, R.; Ishida, K.: Cobalt-Base High-Temperature Alloys. In: *Science* 312.5770 (2006), 90–91.

[174] Pyczak, F.; Bauer, A.; Göken, M.; Lorenz, U.; Neumeier, S.; Oehring, M.; Paul, J.; Schell, N.; Schreyer, A.; Stark, A.; Symanzik, F.: The Effect of Tungsten Content on the Properties of L12-hardened Co–Al–W Alloys. In: *Journal of Alloys and Compounds* 632 (2015), 110–115.

[175] Suzuki, A.: High-Temperature Strength and Deformation of γ/γ' Two-Phase Co–Al–W-base Alloys. In: *Acta Materialia* 56.6 (2008), 1288–1297.

[176] Ooshima, M.; Tanaka, K.; Okamoto, N. L.; Kishida, K.; Inui, H.: Effects of Quaternary Alloying Elements on the γ' Solvus Temperature of Co–Al–W Based Alloys with Fcc/L12 Two-Phase Microstructures. In: *Journal of Alloys and Compounds* 508.1 (2010), 71–78.

[177] Povstugar, I.; Choi, P.-P.; Neumeier, S.; Bauer, A.; Zenk, C. H.; Göken, M.; Raabe, D.: Elemental Partitioning and Mechanical Properties of Ti- and Ta-containing Co–Al–W-base Superalloys Studied by Atom Probe Tomography and Nanoindentation. In: *Acta Materialia* 78 (2014), 78–85.

[178] Xue, F.; Zhou, H.; Ding, X.; Wang, M.; Feng, Q.: Improved High Temperature γ' Stability of Co–Al–W-base Alloys Containing Ti and Ta. In: *Materials Letters* 112 (2013), 215–218.

[179] Alloys, C. A. F. C. H. R.: AMS5917 Metal Injection Molded Nickel Based Alloy 718 Parts Hot Isostatically Pressed, Solutioned and Aged. 2017.

[180] An, X. L.; Zhou, L.; Zhang, B.: Inconel 718 Treated with Two-Stage Solution and Aging Processes: Microstructure Evolution and Enhanced Properties. In: *Materials Research Express* 6.7 (2019), 075803.

[181] Chang, L.; Sun, W.; Cui, Y.; Yang, R.: Influences of Hot-Isostatic-Pressing Temperature on Microstructure, Tensile Properties and Tensile Fracture Mode of Inconel 718 Powder Compact. In: *Materials Science and Engineering: A* 599 (2014), 186–195.

[182] Miura, H.; Ikeda, H.; Iwahashi, T.; Osada, T.: *High Temperature and Fatigue Properties of Injection Moulded Superalloy Compacts*. In: *Proceedings of the World Powder Metallurgy Congress and Exhibition, World PM 2010*. Vol. 4. Florence, Italy, 2010, 86–90.

[183] Özgün, Ö.; Gülsoy, H. Ö.; Yılmaz, R.; Fındık, F.: Microstructural and Mechanical Characterization of Injection Molded 718 Superalloy Powders. In: *Journal of Alloys and Compounds* 576 (2013), 140–153.

[184] Sidambe, A. T.; Derguti, F.; Russell, A. D.; Todd, I.: Influence of Processing on the Properties of IN718 Parts Produced via Metal Injection Moulding. In: *PIM Int.* 7 (2013), 81–85.

[185] Youhua, H.; Yimin, L.; Hao, H.; Jia, L.; Xiao, T.: Preparation and Mechanical Properties of Inconel718 Alloy by Metal Injection Molding. In: *Rare Metal Materials and Engineering* 39.5 (2010), 775–780.

[186] Klöden, B.; Weissgaerber, T.; Kieback, B.; Langer, I.: The Processing and Properties of Metal Injection Moulded Superalloys. In: *Powder injection moulding international* 7.1 (2013), 53–66.

[187] Klöden, B.; Jehring, U.; Weißgärber, T.; Kieback, B.; Langer, I.: High Temperature Properties of MIM Processed Superalloys. In: *Powder Injection Moulding International* 4.4 (2010), 63–67.

[188] Tsukamoto, Y.; Kobayashi, S.; Takasugi, T.: The Stability of γ'-Co_3(Al,W) Phase in Co-Al-W Ternary System. In: *Materials Science Forum* 654 (Trans Tech Publications Ltd 2010), 448–451.

[189] Freund, L.: *Mikrostrukturelle und mechanische Charakterisierung von polykristallinen ausscheidungsgehärteten Co-Basis Superlegierungen unter besonderer Berücksichtigung der Verformungsmechanismen*. In collab. with Erlangen-Nürnberg, F.-A.-U. FAU Forschungen Reihe B, Medizin, Naturwissenschaft, Technik Band 31. Erlangen: FAU University Press, 2019. 216 pp.

[190] Forsik, S. A. J.; Polar Rosas, A. O.; Wang, T.; Colombo, G. A.; Zhou, N.; Kernion, S. J.; Epler, M. E.: High-Temperature Oxidation Behavior of a Novel Co-Base Superalloy. In: *Metallurgical and Materials Transactions A* 49.9 (2018), 4058–4069.

[191] Freund, L. P.; Stark, A.; Kirchmayer, A.; Schell, N.; Pyczak, F.; Göken, M.; Neumeier, S.: The Effect of a Grain Boundary Pinning B2 Phase on Polycrystalline Co-Based Superalloys with Reduced Density. In: *Metallurgical and Materials Transactions A* 49.9 (2018), 4070–4078.

[192] Freund, L. P.; Stark, A.; Pyczak, F.; Schell, N.; Göken, M.; Neumeier, S.: The Grain Boundary Pinning Effect of the μ Phase in an Advanced Polycrystalline γ/γ' Co-base Superalloy. In: *Journal of Alloys and Compounds* 753 (2018), 333–342.

[193] Tsunekane, M.; Suzuki, A.; Pollock, T. M.: Single-Crystal Solidification of New Co–Al–W-base Alloys. In: *Intermetallics* 19.5 (2011), 636–643.

[194] Murray, S. P.; Pusch, K. M.; Polonsky, A. T.; Torbet, C. J.; Seward, G. G. E.; Zhou, N.; Forsik, S. A. J.; Nandwana, P.; Kirka, M. M.; Dehoff, R. R.; Slye, W. E.; Pollock, T. M.: A Defect-Resistant Co–Ni Superalloy for 3D Printing. In: *Nature Communications* 11.1 (2020), 1–11.

[195] Polonsky, A.; Francis, T.; Pusch, K.; Echlin, M.; Botman, A.; Randolph, S.; Geurts, R.; Filevich, J.; Pollock, T.: 3D Characterization of a Novel CoNi-superalloy for Additive Manufacturing. In: *Microscopy and Microanalysis* 26.S2 (2020), 1688–1690.

[196] Cartón-Cordero, M.; Srinivasarao, B.; Campos, M.; García-Junceda, A.; Torralba, J.: On the Role of Processing Parameters in Sintered New Co-based (W,Al) Alloys. In: *Journal of Alloys and Compounds* 674 (2016), 406–412.

[197] Casas, R.; Gálvez, F.; Campos, M.; Dunand, D.; Seidman, D.: *Effect of Heat Treatments on γ/γ' Microstructures and Strengthening in Cobalt-Base Superalloys Created by Powder Metallurgy.* In: Euro PM 2107. Milan, Italy, 2017.

[198] Casas, R.: Design of High Temperature Cobalt-Based Alloys Processed by Powder Metallurgy Route. PhD thesis. Universidad Carlos III de Madrid, 2018.

[199] Tiberto; Klotz, U. E.; Held, F.: Einfluss Der Thermophysikalischen Eigenschaften Auf Die Verarbeitbarkeit von CuSn- Legierungen Durch Das Selektive Laserschmelzen. In: *Metall-Forschung* 71 (2017), 452–458.

[200] Trevisan, F.; Calignano, F.; Lorusso, M.; Lombardi, M.; Manfredi, D.; Fino, P.: *Selective Laser Melting of Chemical Pure Copper Powders*. In: Euro PM 2017. Milan, Italy, 2017.

[201] Constantin, L.; Wu, Z.; Li, N.; Fan, L.; Silvain, J.-F.; Lu, Y. F.: Laser 3D Printing of Complex Copper Structures. In: *Additive Manufacturing* 35 (2020), 101268.

[202] Grünes Licht für neues 3D-Verfahren - Fraunhofer ILT. Fraunhofer-Institut für Lasertechnik ILT. URL: https://www.ilt.fraunhofer.de/de/presse/pressemitteilungen/pm2017/pressemitteilung-30-08-2017.html (visited on 03/18/2021).

[203] Jiang, Q.; Zhang, P.; Yu, Z.; Shi, H.; Wu, D.; Yan, H.; Ye, X.; Lu, Q.; Tian, Y.: A Review on Additive Manufacturing of Pure Copper. In: *Coatings* 11.6 (2021), 740.

[204] Yan, X.; Chang, C.; Dong, D.; Gao, S.; Ma, W.; Liu, M.; Liao, H.; Yin, S.: Microstructure and Mechanical Properties of Pure Copper Manufactured by Selective Laser Melting. In: *Materials Science and Engineering: A* 789 (2020), 139615.

[205] Frigola, P.; Harrysson, O. A.; Horn, T. J.; West, H. A.; Aman, R. L.; Rigsbee, J. M.; Ramirez, D. A.; Murr, L. E.; Medina, F.; Wicker, R. B.; Rodriguez, E.: Fabricating Copper Components. In: *Advanced Materials & Processes* 172 (2014), 20–24.

[206] Bai, Y.; Williams, C. B.: An Exploration of Binder Jetting of Copper. In: *Rapid Prototyping Journal* 21.2 (2015), 177–185.

[207] Kumar, A.; Bai, Y.; Eklund, A.; Williams, C. B.: Effects of Hot Isostatic Pressing on Copper Parts Fabricated via Binder Jetting. In: *Procedia Manufacturing* 10 (2017), 935–944.

[208] Davis, J. R., ed.: *Copper and Copper Alloys*. ASM International, 2001. 659 pp.

[209] Heath, P. J.; Evans, P. E.: Sintering, Fracture and Oxide Films. In: *Journal of Materials Science* 9.12 (1974), 1955–1960.

[210] Vaezi, M.; Chianrabutra, S.; Mellor, B.; Yang, S.: Multiple Material Additive Manufacturing – Part 1: A Review: This Review Paper Covers a Decade of Research on Multiple Material Additive Manufacturing Technologies Which Can Produce Complex Geometry Parts with Different Materials. In: *Virtual and Physical Prototyping* 8.1 (2013), 19–50.

[211] Islam, A.; Hansen, H. N.; Bondo, M.: Experimental Investigation of the Factors Influencing the Polymer–Polymer Bond Strength during Two-Component Injection Moulding. In: *The International Journal of Advanced Manufacturing Technology* 50.1 (2010), 101–111.

[212] Scheithauer, U.; Bergner, A.; Schwarzer, E.; Richter, H.-J.; Moritz, T.: Studies on Thermoplastic 3D Printing of Steel–Zirconia Composites. In: *Journal of Materials Research* 29.17 (2014), 1931–1940.

[213] Scheithauer, U.: Additive Manufacturing of Metal-Ceramic-Composites by Thermoplastic 3D-Printing (3DTP). In: *Journal of Ceramic Science and Technology* 6.2 (2015), 125–132.

[214] Brooks, H.; Clarkson, P.; Davies, P.; Fairclough, D.: *Sintering of 3D Printed Metal, Ceramic and Glass Multi-Material Parts*. In: 15th Rapid Design, Prototyping & Manufacturing (RDPM) Conference. Northumbria University, Newcastle, 2017.

[215] Schmitt, P. A.; Myerberg, J. S.; Fulop, R.; Gibson, M. A.; Verminski, M. D.; Fontana, R. R.; Schuh, C. A.; Chiang, Y.-M.; Hart, A. J.: Fabricating Mulit-Part Assemblies. U.S. pat. 9,815,118 B1. 2017.

[216] Gibson, M. A.; Myerberg, J. S.; Fulop, R.; Verminski, M. D.; Fontana, R. R.; Schuh, C. A.; Chiang, Y.-M.; Hart, A. J.: Fabricating an Interface Layer for Removable Support. U.S. pat. 9,833,839 B2. 2017.

[217] Simchi, A.; Petzoldt, F.; Hartwig, T.: *An Approach for Assessment of Sintering Behavior of Co-injection Moulded PIM Feedstocks by Dilatometric Analysis*. In: *European Congress and Exhibition on Powder Metallurgy. European PM Conference Proceedings*. Vol. 2. Prague, Czech Republic: The European Powder Metallurgy Association, 2005, 365–370.

[218] Dutra, G. B.; Mulser, M.; Calixto, R.; Petzoldt, F.: Investigation of Material Combinations Processed via Two-Component Metal Injection Moulding (2C-MIM). In: *Materials Science Forum* 727 (Trans Tech Publications Ltd 2012), 248–253.

[219] Baumann, A.: *Pulverspritzgießen von Metall-Keramik-Verbunden*. Schriftenreihe Kompetenzen in Keramik 9. Stuttgart: Fraunhofer Verlag, 2011. 153 pp.

[220] Cai, P. Z.; Green, D. J.; Messing, G. L.: Constrained Densification of Alumina/Zirconia Hybrid Laminates, I: Experimental Observations of Processing Defects. In: *Journal of the American Ceramic Society* 80.8 (2005), 1929–1939.

[221] Heaney, D. F.; Suri, P.; German, R. M.: Defect-Free Sintering of Two Material Powder Injection Molded Components Part I *Experimental Investigations*. In: *Journal of Materials Science* 38.24 (2003), 4869–4874.

[222] Dutra, B.: *Influence of a Mismatch in Shrinkage for Two-Component Metal Injection Moulding (2C-MIM)*. In: International Powder Metallurgy Congress and Exhibition. Vol. 4. Florence, 2010.

[223] Jiang, J.; Xu, X.; Stringer, J.: Support Structures for Additive Manufacturing: A Review. In: *Journal of Manufacturing and Materials Processing* 2.4 (2018), 64.

[224] Vanek, J.; Galicia, J. A. G.; Benes, B.: Clever Support: Efficient Support Structure Generation for Digital Fabrication. In: *Computer Graphics Forum* 33.5 (2014), 117–125.

[225] Zhang, Y.; Wang, Z.; Zhang, Y.; Gomes, S.; Bernard, A.: Bio-Inspired Generative Design for Support Structure Generation and Optimization in Additive Manufacturing (AM). In: *CIRP Annals* 69.1 (2020), 117–120.

[226] Desktop Metal: Separable Supports™ for Easy Post-Processing. URL: https://www.desktopmetal.com/resources/separable-supports-post-processing (visited on 10/29/2021).

[227] Marlin 3D Printer Firmware. Marlin, 2018.

[228] Carl Roth GmbH + Co KG; Cyclohexan. Sicherheitsdatenblatt. 2018.

[229] Nolze, G.; Hielscher, R.: Orientations – Perfectly Colored. In: *Journal of Applied Crystallography* 49.5 (2016), 1786–1802.

[230] Felfer, P.: Atom Probe Toolbox. 2021. URL: https://github.com/peterfelfer/Atom-Probe-Toolbox (visited on 09/13/2021).

[231] Hochleistungskeramik - Mechanische Eigenschaften Monolithischer Keramik Bei Raumtemperatur - Teil 1: Bestimmung Der Biegefestigkeit; Deutsche Fassung EN 843-1:2006. 2008.

[232] Thompson, Y.; Gonzalez-Gutierrez, J.; Kukla, C.; Felfer, P.: Fused Filament Fabrication, Debinding and Sintering as a Low Cost Additive Manufacturing Method of 316L Stainless Steel. In: *Additive Manufacturing* 30 (2019), 100861.

[233] Prüfung Metallischer Werkstoffe - Druckversuch Bei Raumtemperatur; DIN 50106:2016-11. 2016.

[234] Lopez Ruiz, B.: Fused Filament Fabrication of Tool Steel: Influence of Filament Fillgrade and Heat Treatment. Mini-Project, MAP. FAU Erlangen-Nürnberg, 2022.

[235] Hwang, S.; Reyes, E. I.; Moon, K.-s.; Rumpf, R. C.; Kim, N. S.: Thermo-Mechanical Characterization of Metal/Polymer Composite Filaments and Printing Parameter Study for Fused Deposition Modeling in the 3D Printing Process. In: *Journal of Electronic Materials* 44.3 (2015), 771–777.

[236] Serdeczny, M.; Comminal, R.; Pedersen, D. B.; Spangenberg, J.: Influence of Fibers on the Flow through the Hot-End in Material Extrusion Additive Manufacturing. In: *Industrializing Additive Manufacturing*. Ed. by Meboldt, M.; Klahn, C. AMPA 2020. Cham: Springer International Publishing, 2020, 251–267.

[237] Spoerk, M.; Gonzalez-Gutierrez, J.; Sapkota, J.; Schuschnigg, S.; Holzer, C.: Effect of the Printing Bed Temperature on the Adhesion of Parts Produced by Fused Filament Fabrication. In: *Plastics, Rubber and Composites* 47.1 (2018), 17–24.

[238] Spoerk, M.; Gonzalez-Gutierrez, J.; Lichal, C.; Cajner, H.; Berger, G.; Schuschnigg, S.; Cardon, L.; Holzer, C.: Optimisation of the Adhesion of Polypropylene-Based Materials during Extrusion-Based Additive Manufacturing. In: *Polymers* 10.5 (2018), 490.

[239] Dunstan, M. K.; Paramore, J. D.; Fang, Z. Z.: Gaseous Isostatic Forging: Design and Application to Powder Metallurgy Ti-6Al-4V. In: *Journal of Materials Processing Technology* 259 (2018), 292–304.

[240] Turner, C.; Ashby, M.: The Cold Isostatic Pressing of Composite Powders-I. Experimental Investigations Using Model Powders. In: *Acta Materialia* 44.11 (1996), 4521–4530.

[241] Paramore, J. D.; Fang, Z. Z.; Dunstan, M.; Sun, P.; Butler, B. G.: Hydrogen-Enabled Microstructure and Fatigue Strength Engineering of Titanium Alloys. In: *Scientific Reports* 7.1 (2017), 1–12.

[242] Li, Y.; Liu, S.; Qu, X.; Huang, B.: Thermal Debinding Processing of 316L Stainless Steel Powder Injection Molding Compacts. In: *Journal of Materials Processing Technology* 137.1-3 (2003), 65–69.

[243] Derfuß, B.: Entbinderungsverhalten Beim Pulverspritzguss Mit Mesophasenkohlenstoff Und Wasserlöslichen Bindersystemen. PhD thesis. Friedrich-Alexander-Universität Erlangen, 2009.

[244] Pinwill, I. E.; Edirisinghe, M. J.; Bevis, M. J.: Development of Temperature-Heating Rate Diagrams for the Pyrolytic Removal of Binder Used for Powder Injection Moulding. In: *Journal of materials science* 27.16 (1992), 4381–4388.

[245] Lam, Y. C.; Shengjie, Y.; Yu, S. C. M.; Tam, K. C.: Simulation of Polymer Removal from a Powder Injection Molding Compact by Thermal Debinding. In: *Metallurgical and Materials Transactions A* 31.10 (2000), 2597–2606.

[246] Raza, M. R.; Ahmad, F.; Omar, M.; German, R.; Muhsan, A. S.: Role of Debinding to Control Mechanical Properties of Powder Injection Molded 316L Stainless Steel. In: *Advanced Materials Research* 699 (Trans Tech Publications Ltd 2013), 875–882.

[247] Voigt, J.: Additive Fertigung von Polymerbasierten Und Pulverbasierten Metallen Und Keramiken. Masterarbeit. FAU Erlangen-Nürnberg, 2019.

[248] Salmang, H.; Scholze, H.: *Keramik*. Ed. by Telle, R. 7th ed. Berlin, Heidelberg: Springer, 2007. 1148 pp.

[249] Pfeiffer, S.; Florio, K.; Puccio, D.; Grasso, M.; Colosimo, B. M.; Aneziris, C. G.; Wegener, K.; Graule, T.: Direct Laser Additive Manufacturing of High Performance Oxide Ceramics: A State-of-the-Art Review. In: *Journal of the European Ceramic Society* 41.13 (2021), 6087–6114.

[250] Travitzky, N.; Bonet, A.; Dermeik, B.; Fey, T.; Filbert-Demut, I.; Schlier, L.; Schlordt, T.; Greil, P.: Additive Manufacturing of Ceramic-Based Materials: Additive Manufacturing of Ceramic-Based Materials. In: *Advanced Engineering Materials* 16.6 (2014), 729–754.

[251] Wang, J.-C.; Dommati, H.; Hsieh, S.-J.: Review of Additive Manufacturing Methods for High-Performance Ceramic Materials. In: *The International Journal of Advanced Manufacturing Technology* 103.5 (2019), 2627–2647.

[252] Thompson, Y.: Low Cost Additive Manufacturing via Metal Extrusion Modeling. Masterarbeit. FAU Erlangen-Nürnberg, 2017.

[253] Marshall, P.: *Austenitic Stainless Steels: Microstructure and Mechanical Properties*. Springer Science & Business Media, 1984. 458 pp.

[254] Atanda, P.; Fatudimu, A.; Oluwole, O.: Sensitisation Study of Normalized 316L Stainless Steel. In: *Journal of Minerals and Materials Characterization and Engineering* 9.1 (2010), 13–23.

[255] Werkzeugstähle (ISO 4957:2018); Deutsche Fassung EN ISO 4957:2018. 2018.

[256] Soukup, M.: Einfluss Der Sinteratmosphäre Auf Die Härtbarkeit von Fused-Filament Additiv Gefertigtem Warmarbeitsstahl. Bacheloarbeit. FAU Erlangen-Nürnberg, 2021.

[257] Böhler Edelstahl GmbH: W303 Warmarbeitsstahl. 2020. URL: https://www.bohler-edelstahl.com/app/uploads/sites/92/2018/08/W303DE.pdf (visited on 09/14/2020).

[258] Mazur, M.; Brincat, P.; Leary, M.; Brandt, M.: Numerical and Experimental Evaluation of a Conformally Cooled H13 Steel Injection Mould Manufactured with Selective Laser Melting. In: *The International Journal of Advanced Manufacturing Technology* 93.1 (2017), 881–900.

[259] Cormier, D.; Harrysson, O.; West, H.: Characterization of H13 Steel Produced via Electron Beam Melting. In: *Rapid Prototyping Journal* 10.1 (2004), 35–41.

[260] Bajaj, P.; Hariharan, A.; Kini, A.; Kürnsteiner, P.; Raabe, D.; Jägle, E.: Steels in Additive Manufacturing: A Review of Their Microstructure and Properties. In: *Materials Science and Engineering: A* 772 (2020), 138633.

[261] Murray, J. L.: The Fe–Ti (Iron-Titanium) System. In: *Bulletin of Alloy Phase Diagrams* 2.3 (1981), 320–334.

[262] Attar, H.; Calin, M.; Zhang, L.; Scudino, S.; Eckert, J.: Manufacture by Selective Laser Melting and Mechanical Behavior of Commercially Pure Titanium. In: *Materials Science and Engineering: A* 593 (2014), 170–177.

[263] Thompson, Y.; Zissel, K.; Förner, A.; Gonzalez-Gutierrez, J.; Kukla, C.; Neumeier, S.; Felfer, P.: Metal Fused Filament Fabrication of the Nickel-Base Superalloy IN 718. In: *Journal of Materials Science* 57.21 (2022), 9541–9555.

[264] Sindhura, D.; Sravya, M. V.; Murthy, G. V. S.: Comprehensive Microstructural Evaluation of Precipitation in Inconel 718. In: *Metallography, Microstructure, and Analysis* 8.2 (2019), 233–240.

[265] Miller, M.; Babu, S.; Burke, M.: Comparison of the Phase Compositions in Alloy 718 Measured by Atom Probe Tomography and Predicted by Thermodynamic Calculations. In: *Materials Science and Engineering: A* 327.1 (2002), 84–88.

[266] Hajmrle, K.; Angers, R.; Dufour, G.: Phase Analysis of Sintered and Heat Treated Alloy 718. In: *Metallurgical Transactions A* 13.1 (1982), 5–12.

[267] EOS GmbH, Electro Optical Systems: EOS NickelAlloy IN718. 2020. URL: https://www.eos.info/03_system-related-assets/material-related-contents/metal-materials-and-examples/metal-material-datasheet/nickelalloy-inconel/material_datasheet_eos_nickelalloy_in718_m290_premium_en_web.pdf (visited on 11/17/2021).

[268] Han, Y.; Chaturvedi, M.: Steady State Creep Deformation of Superalloy Inconel 718. In: *Materials Science and Engineering* 89 (1987), 25–33.

[269] Caliari, F. R.; Candioto, K. C. G.; Couto, A. A.; Nunes, C. Â.; Reis, D. A. P.: Effect of Double Aging Heat Treatment on the Short-Term Creep Behavior of the Inconel 718. In: *Journal of Materials Engineering and Performance* 25.6 (2016), 2307–2317.

[270] Hayes, R.: *Creep Deformation of Inconel Alloy 718 in the 650°C to 760°C Temperature Regime*. In: *Superalloys 718, 625 and Various Derivatives (1991)*. Superalloys. Pittsburgh, Pennsylvania, USA: TMS, 1991, 549–562.

[271] Pröbstle, M.; Neumeier, S.; Hopfenmüller, J.; Freund, L.; Niendorf, T.; Schwarze, D.; Göken, M.: Superior Creep Strength of a Nickel-Based Superalloy Produced by Selective Laser Melting. In: *Materials Science and Engineering: A* 674 (2016), 299–307.

[272] Chaturvedi, M.; Han, Y.: *Creep Deformation of Alloy 718*. In: *Superalloys 718 Metallurgy and Applications (1989)*. Superalloys. Pittsburgh, Pennsylvania, USA: TMS, 1989, 489–498.

[273] Li, S.; Zhuang, J.; Yang, J.; Deng, Q.; Du, J.; Xie, X.; Li, B.; Xu, Z.; Cao, Z.; Su, Z.; Jiang, C.: *The Effect of Delta-Phase on Crack Propagation Under Creep and Fatigue Conditions in Alloy 718*. In: *Superalloys 718, 625 and Various Derivatives (1994)*. Pittsburgh, Pennsylvania, USA: TMS, 1994, 545–555.

[274] Meermeier, A.: Additive Fertigung einer Kobaltbasissuperlegierung mittels polymergebundener Filamentextrusion. Masterarbeit. FAU Erlangen-Nürnberg, 2022.

[275] Cahn, J. W.: The Impurity-Drag Effect in Grain Boundary Motion. In: *Acta Metallurgica* 10.9 (1962), 789–798.

[276] Neumeier, S.; Rehman, H.; Neuner, J.; Zenk, C.; Michel, S.; Schuwalow, S.; Rogal, J.; Drautz, R.; Göken, M.: Diffusion of Solutes in Fcc Cobalt Investigated by Diffusion Couples and First Principles Kinetic Monte Carlo. In: *Acta Materialia* 106 (2016), 304–312.

[277] Zhou, X.; Fu, H.; Xue, F.; Zhang, Y.; Xie, J.: Abnormal Precipitation of the μ Phase During Solution Treatment of γ'-Strengthened Co-Ni-Al-W-Based Superalloys. In: *Scripta Materialia* 181 (2020), 30–34.

[278] Qin, X. Z.; Guo, J. T.; Yuan, C.; Yang, G. X.; Zhou, L. Z.; Ye, H. Q.: M-Phase Behavior in a Cast Ni-base Superalloy. In: *Journal of Materials Science* 44.18 (2009), 4840–4847.

[279] Sugui, T.; Minggang, W.; Tang, L.; Benjiang, Q.; Jun, X.: Influence of TCP Phase and Its Morphology on Creep Properties of Single Crystal Nickel-Based Superalloys. In: *Materials Science and Engineering: A* 527.21-22 (2010), 5444–5451.

[280] Schupp, Z.: Herstellung von Kupfer/316L-Verbunden Mittels "Fused Filament Fabrication". Masterarbeit. FAU Erlangen-Nürnberg, 2018.

[281] Marschall, M.: Additive Fertigung von Kupfer Mittels Filament 3D-Druck. Bachelorarbeit. FAU Erlangen-Nürnberg, 2018.

[282] Pineau, A.; Benzerga, A.; Pardoen, T.: Failure of Metals I: Brittle and Ductile Fracture. In: *Acta Materialia* 107 (2016), 424–483.

[283] Dash, K.; Panda, S.; Ray, B. C.: Process and Progress of Sintering Behavior of Cu-Al_2 O_3 Composites. In: *Emerging Materials Research* 2.1 (2013), 32–38.

[284] Utz, Y.: Additive Fertigung Komplexer Geometrien Mittels Filamentextrusion. Bachelorarbeit. FAU Erlangen-Nürnberg, 2020.

Acknowledgements

Vielen Dank all denjenigen, die durch ihre fachliche und moralische Unterstützung zur Entstehung dieser Arbeit beigetragen haben!

An erster Stelle möchte ich meinem Doktorvater Prof. Dr. Peter Felfer meinen Dank aussprechen, der mir die Bearbeitung dieses Projekts auf mehrfachen Wunsch übertragen hat, obgleich es den Themenbereich der Atomsonden-Gruppe stark erweitert hat. Auch in Phasen, in denen Fortschritte nur schleppend oder scheinbar gar nicht zustande kamen, hat mich Dein unerschütterlicher Optimismus weiterhin an den Erfolg dieses Projektes glauben lassen.

Meinen Projektpartnern der Montanuniversität Leoben gebührt mein Dank, nicht nur für die Fertigung der 3D Druck Filamente aus jeglichem bereitgestellten Pulver. Dr. Christian Kukla and Dr. Joamin Gonzalez-Gutierrez: Thank you for sharing you FFF-knowledge, the helpful troubleshooting during the first project times and proofreading of all publications at any state.

Besonders bedanken möchte ich mich auch beim gesamten Leitungskreis des Lehrstuhls Herrn Prof. Dr. Mathias Göken, Herrn PD Dr. Heinz Werner Höppel und Herrn Dr. Steffen Neumeier fürs Bereiten der unvergleichlichen und so wertvollen WWI-Atmosphäre. Gemeinsam mit allen Kollegen und Technikern hat mir insbesondere die 10 Uhr Kaffeepause so manchen Tag gerettet, wenn die Wissenschaft mal wieder größere Herausforderungen bereithielt.

Ein großer Dank geht auch an meine vielen Bachelor- und Masterarbeiter, die mir das Vertrauen geschenkt haben eines meiner Themen zu bearbeiten und wertvolle Ergebnisse zu dieser Arbeit beigetragen haben: Zeno Schupp, Jorrit Voigt, Maximilian Marschall, Manuel Burghold, Markus Polzer, Kai Zissel, Maximilian Soukup, Beatrix Lopez Ruiz und insbesondere Annalena Meermeier fürs zusätzliche Korrekturlesen. Ein großes Dankeschön auch meinem langjährigen HiWi Stefan Leimbach für die Unterstützung bei den experimentellen Arbeiten, besonders die überragende Probenpräparation.

Zusätzlich wurde ich von vielen Kollegen auch bei der Durchführung von Messungen unterstützt. Daher möchte ich Jennifer Reiser für die

TGA-Messungen, Dr. Julian Koopmann für die Messungen der Partikelgrößenverteilung, Jonas Harrer und Christina Hasenest für die Messungen der Dichte, Philip Keilholz für die chemischen Analysen, Andreas Bezold für die TEM - Aufnahmen und Dr. Valentin Dahlbauer und Andreas Förner für die Atomsondentomographien danken. Besonderer Dank gilt außerdem Werner Langner, ohne den der 3D Drucker vermutlich nie ein funktionierendes Heizbett bekommen hätte und der meinen Vakuumofen trotz der Misshandlungen für Forschungszwecke immer wieder aufs Neue funktionsfähig gehalten hat. Danke auch an Dr. Benjamin Ruttert, der mir zum Ende meiner Arbeit noch die Möglichkeit gegeben hat, die Vorzüge des HIP zu testen.

Allen Kollegen der Arbeitsgruppe Felfer ein großes Dankeschön für den gemeinsamen Weg, die gegenseitige Motivation und Durchhalteparolen. Gleiches gilt in besonderem Maße für die wechselnden Bürokollegen in 3.26 fürs gemeinsame Frieren, das begrünte Fensterbrett und die Kinderschokolade-Schrankbar, die die Arbeitszeit erheblich versüßt haben.

Neben den bereits genannten haben noch viele weitere Kollegen und Freunde fachlich aber auch persönlich zum Gelingen meiner Arbeit beigetragen. Ihnen allen gilt natürlich mein Dank, insbesondere: Jan Josten für die unerschütterliche positive Energie; Valentin Dahlbauer fürs montägliche Bier-vor-4; dem Wintersportbeauftragen Nicklas Volz fürs organisieren und allen die dabei waren für die legendären Skifreizeiten; der WW-Laufgruppe: besonders Benedikt Diepold fürs Antreiben und meinen Trainingspartnern Daniel Elitzer und Daniel Hausmann für die bewegten Pausen; Martin Endt, Werner Langner, Martin Weiser, Markus Bierling, Nora Vorlaufer und Moritz Kuglstatter für die Schafkopf-Runden, Benedict Ott für fliegende Enten, Julia Groppweis für deine Nähmaschine und die Sushi-Sessions, Dorothèe Kaup für die Kaffee aka Shopping-Pausen und meinen Korrekturlesern Andreas Förner, Annalena Meermeier und Philip Keilholz fürs freiwillig Melden und die hilfreichen Verbesserungsvorschläge.

Ganz herzlich danken möchte ich meiner Familie und meinen Eltern für die Förderung und den vorbehaltlosen Rückhalt in all den Jahren und meiner Schwester, die schon ganze Gespräche über Metallpulver führen kann. Danke Andreas für die Aufmunterung, deine Geduld und Essensversorgung während der Wochenendschichten und dass du für angemessenen Ausgleich abseits des Diss-Programms gesorgt hast.

Metal fused filament fabrication (MF^3) with metal-filled filaments is an indirect process that uses polymeric binders for additive shaping of green bodies. These are processed into solid metal parts after debinding and sintering. Due to the filament-based shaping, this process can be used for the additive manufacturing of all sinterable powder materials requiring low investment costs. The MF^3 process could thus provide a cost-effective and material-flexible alternative to powder bed fusion (PBF) manufacturing of small metallic components with complex shapes. To enable a successful process application, parameter optimization as well as the selection of the furnace atmosphere for each individual process step is crucial to achieve a high final density. In this context, the applied parameters have a significant influence on the microstructure and the functional and mechanical properties of the manufactured components.

It is the aim of this work to identify suitable parameter sets for the individual process steps and to evaluate the applicability of MF^3 for AM of various high-value metal alloys. This includes a general parameter optimization for each step of the entire process chain of shaping, debinding and sintering, independently of the processed metal powder. Based on the general process implementation, systematic parameter studies were performed for 316L, Ampersint 1557.02, cp-Ti, IN 718, CoWAlloy3mod, and 99 % pure Cu to derive the best processing strategies for each of these metals.

ISBN 978-3-96147-687-9

FAU UNIVERSITY PRESS 2023